Title

Dynamic and Non-equilibrium Polymeric Materials

Author

Muradyan, Hurik

Publication Date

2020

UNIVERSITY OF CALIFORNIA,
IRVINE

Dynamic and Non-equilibrium Polymeric Materials

DISSERTATION

submitted in partial satisfaction of the requirements
for the degree of

DOCTOR OF PHILOSOPHY

in Chemistry

by

Hurik Muradyan

Dissertation Committee:
Professor Zhibin Guan, Chair
Distinguished Professor Kenneth J. Shea
Professor Shane Ardo

2020

Dedication

To

My family new and old

I would not be here without you all

Table of Contents

Dedication ii

Table of Contents iii

List of Figures v

List of Tables vii

List of Schemes viii

Acknowledgments ix

Vita xii

Abstract of Dissertation xiv

Chapter 1: Introduction to Nonequilibrium Systems 1

1.1 Background 1

1.2 History of studying nonequilibrium systems 5

1.3 Distinction between nonequilibrium systems and other closely related systems 6

1.4 Sources of energy used in synthetic nonequilibrium systems 9

1.5 Modes of operation in synthetic nonequilibrium systems 11

1.6 Molecular motor based nonequilibrium systems 13

1.7. Dissipative Supramolecular Assembly 20

1.8 Dissipative colloidal assembly 24

1.8.1 Chemically driven dissipative colloidal assembly 25

1.8.2 Light driven dissipative colloidal assembly 27

1.8.3 Light & chemically driven active colloidal motion 29

1.8.4 Chemically driven active colloidal motion 30

1.8.5 Magnetically driven active colloidal motion 31

1.9 Dissipative Macroscopic Behavior 32

1.9.1 Chemically fueled macroscopic dissipative behavior 32

1.10 Emergent behavior of synthetic nonequilibrium systems 35

1.11 Challenges of synthetic nonequilibrium systems 38

1.12 Goals of thesis 39

Chapter 2: Chemothermally Driven Out-of-equilibrium Materials 40

2.1 Introduction chemically fueled nonequilibrium materials 40

2.2 Our design of self-regulating materials 41

2.3 Results and discussion 43

2.3.1 Exothermicity 43

2.3.2 Coupling to colloidal pNIPAAm solution 44

2.3.3 Coupling to macroscopic pNIPAAm hydrogels 46

2.4 Conclusion 47

2.5 Experimental 48

2.5.1 Synthesis of small molecules 49

2.5.2 Small molecule studies 52

2.5.3 Synthesis and characterization of polymers 54
2.5.4 Turbidity experiments for temperature-responsive NPs 60
2.5.5 Macroscopic hydrogel experiments 62
2.5.6 Calculations for power output 64
2.5.7 NMR spectra 66
Chapter 3: Progress Towards Self-regulating Materials 69
3.1 Introduction to self-regulating materials 69
3.2 Our design of self-regulating materials 70
3.3 Results and discussion 72
3.3.2 Hydrogel nanoparticle approach 78
3.3.3 Acrylamide core-shell nanoparticle approach 81
3.3.4 Mesoporous silica/polyethylene glycol core-shell nanoparticle approach 82
3.5.1 Synthesis of small molecules and polymers 87
3.5.2 Characterization of temperature responsive polymers 96
3.5.3 NMR spectra 98
Chapter 4: Self-healing Magnetic Nanocomposites 103
4.1 Introduction to self-healing materials 103
4.2 Introduction to self-healing magnetic composites 105
4.3 Our design for self-healing magnetic nanocomposites 107
4.4 Results and discussion 108
4.4.1. Synthesis and characterization of magnetic particles 108
4.4.2 Mechanical properties of magnetic nanocomposites 111
4.4.3 Magnetic actuation of nanocomposites 113
4.5 Conclusion 114
4.6 Experimental 115
4.6.1 Synthesis of BAAm MNP composites 116
4.6.2 Characterization of small molecules and composites 119
References 129

List of Figures

Figure 1.1 Thermodynamic and out-of-equilibrium systems....2
Figure 1.2 Molecular motor scaffolds of rotary motors, biped walkers and rotaxanes. 15
Figure 1.3 Molecular motor scaffolds of catenanes, and rotatory motors based on alkene and imines.. 18
Figure 1.4 Chemically fueled dissipative assemblies 22
Figure 1.5 Chemically fueled dissipative colloidal assemblies....26
Figure 1.6 Light fueled dissipative colloidal assemblies....28
Figure 1.7 Schematics of chemical and light driven colloidal motion using nanoparticle catalysis. 30
Figure 1.8 Schematic of osmosis driven expansion/contraction of a macroscopic chemically fueled hydrogel....34
Figure 1.9 Nonequilibrium behavior in the form of dissipative assembly and self-regulation....37
Figure 2.1 Design concept of chemothermally driven out-of-equilibrium materials and small molecule heat generation studies....42
Figure 2.2 Chemothermally driven out-of-equilibrium system demonstrated for a colloidal solution of pNIPAAm NPs and of macroscopic pNIPAAm hydrogels....45
Figure 2.3 Macroscopic chemically driven out-of-equilibirum behavior. 48
Figure 2.4 Temperature profiles of small molecule CuAAc reactions at different concentration of fuels (32 mM Cu-THPTA)....53
Figure 2.5 Temperature increase with time for small molecule CuAAc reactions at different fuel concentrations (32 mM Cu-THPTA)....53
Figure 2.7 Temperature increase with time for small molecule CuAAc reactions at different concentration of Cu-THPTA catalyst (1 M for both fuels) 54
Figure 2.8 Size distribution of pNIPPAm NPs at 21 ºC measured by DLS. 57
Figure 2.9 Temperature dependence of pNIPPAm NP size measured by DLS....58
Figure 2.14 Temperature change with time recorded for visual turbidity experiment....62
Figure 2.15 Macroscopic work by lifting an object**.**. 64
Figure 2.16 ^{1}H NMR spectrum of 2-azidoethanol in $CDCl_3$. 66
Figure 2.17 ^{1}H NMR spectrum of 3-azidopropanol in $CDCl_3$....67
Figure 2.18 ^{1}H NMR spectra of tris(3-hydroxypropyltriazolylmethyl)amine (THPTA) in d_6-DMSO....68
Figure 3.1 Characterization of bulk macroscopic hydrogels....74
Figure 3.2 Reaction kinetics of catalytic THPTA-co-NIPAAm macroscopic hydrogels. 76
Figure 3.3 Heat generation of catalytic THPTA-co-NIPAAm hydrogels. a 78
Figure 3.4 Catalytic CuNTA nanoparticle system 80
Figure 3.5 Core-shell PEG nanoparticle system. 84
Figure 3.5 DLS characterization of core-shell NP size at pH 7....97
Figure 3.6 **^{1}**H NMR spectrum of 2-azidoethanol in $CDCl_3$. 98
Figure 3.7 ^{1}H NMR spectrum of 3-azidopropanol in $CDCl_3$....99
Figure 3.8 ^{1}H NMR spectrum of THPTA in d_6-DMSO. 100
Figure 3.9 ^{1}H NMR spectrum of THPTAmon in d_6-DMSO....101

Figure 3.10 ^{1}H NMR spectrum of p-THPTA-co-NIPAAm polymer in d_6-DMSO. 102
Figure 4.1 MNP Characterization. 109
Figure 4.2 Mechanical characterization of BAAm-MNP composites....112
Figure 4.5 Differential scanning calorimetry of iron-oleate precursor. 120
Figure 4.6 High resolution transmission electron micrograph. 120
Figure 4.7 Thermogravimetric Analysis (TGA) 121
Figure 4.8 Full FTIR spectra of nanoparticles....121
Figure 4.9 Mechanical properties of BAAm-MNP and BAAm-control. 123
Figure 4.10 Stress-strain curves for BAAM-MNP-85.. 124
Figure 4.11 Stress-strain curves BAAm-MNP-33 at 80 ºC for 5 h. 125
Figure 4.12 Gel permeation chromatogram of cleaved BAAm polymer.. 127
Figure 4.13 ^{1}H NMR spectra of BAAm-MNP-86 after cleaving from particles 128

List of Tables

Table 2.1: Analysis of temperature graphs for small molecule CuAAc reactions at different fuel concentrations (32 mM Cu-THPTA)........53

Table 2.2 Analysis of temperature graphs for small molecule CuAAc reactions at different concentration of Cu-THPTA catalyst (1 M for both fuels) 54

Table 2.3 Summary of DLS data for pNIPPAm NPs at 21 ºC........58

Table 2.4 Temperature dependence of pNIPPAm NP size measured by DLS........59

Table 3.1 DLS characterization of catalytic 5 mol% NTA-co-NIPPAm NP size at pH 7.........96

Table 3.2 DLS characterization of core-shell NP before Cu(II) complexation size at pH 2.........97

Table 4.1 Mechanical and Thermal Properties of BAAm-MNP 122

Table 4.2 Mechanical Properties of Healed and Pristine BAAm-MNP-75 & 85 (ambient conditions)124

Table 4.3 Self-healing Efficiency BAAm-MNP-33 & 85 (ambient conditions)........125

Table 4.4 Mechanical Properties of Healed and Pristine BAAm-MNP-33 (80 ºC, 5h) 126

Table 4.5 Self-healing Efficiency BAAm-MNP-33 (80 ºC, 5h, reduced pressure) 126

List of Schemes

Scheme 2.1: Synthesis of 2-azidoethanol 49
Scheme 2.2 Synthesis of 3-azidopropanol 50
Scheme 2.3: Synthesis of tris(3-hydroxypropyltriazolylmethyl)amine (THPTA) 51
Scheme 3.1 Synthesis of 2-azidoethanol 87
Scheme 3.2 Synthesis of 3-azidopropanol 88
Scheme 3.3 Synthesis Tris(3-hydroxypropyltriazolylmethyl)amine (THPTA) 89
Scheme 3.4 Synthesis of THPTAmon 90
Scheme 3.5 Synthesis of 2,2'-((5-amino-1-carboxypentyl)azanediyl)diacetic acid (N6-NTA) 90
Scheme 3.6 Synthesis of 2,2'-((5-acrylamido-1-carboxypentyl)azanediyl)diacetic acid (NTAmon) 91
Scheme 3.7 Synthesis of 2,2'-((1-carboxy-5-(pent-4-ynamido)pentyl)azanediyl)diacetic acid (NTAalkyne) 92
Scheme 4.1 Design and synthesis of self-healing magnetic nanocomposites 108

Acknowledgments

I would like to thank **Prof. Zhibin Guan** for allowing me to work in his lab for 5 years. I have learned more than I ever thought I could—or would. **Prof. Ken Shea**, I am so grateful for your guidance throughout my academic pursuits—before, during and after my candidacy exams. I am forever grateful for your role in my mentorship and growth as a scientist. **Prof. Shane Ardo**, your passion and excitement for science has been inspirational—I am very thankful to have had such positive conversations with you about my projects, especially after a series of experiments that failed to prove a hypothesis.

I would like to thank the members of the Guan lab. Dr. James Neal and Dr. Jaeyoon Chung , Dr. Nathan Oldenhuis, William Ogden, and Dr. Alex Eldridge for their mentorship—especially during my preparation for candidacy exams. **James**, thanks for sticking up for me, I really needed it sometimes. It took me a surprisingly longtime to realize that "I'm living the dream," was not all true, thank you for your perspective. **Jae**, thanks for trying to give me the much-needed reality check on my expectations of science—I wish I were wise enough to understand it at the time. **Nate**, I still remember the note you put on my desk after a failed experiment: Drink and try again—thank you. **Billy**, thank you for being you. **Alex**, thanks for reminding me that social interaction is important for keeping sane and normal. All the younger students I have overlapped with, I hope I have been able to impact your life in a net positive way, I did my best. **Chase**, thanks for being the most direct person you are—it has taught me a lot. **Eric**, thanks for reminding me that some naivety is not bad. **Collin**, thanks for teaching me about CRISPR and sharing beer—Cheers. Thank you to Tomas Mitchell and Rong Tang for being absolute joys to mentor.

I also want to thank my past mentors. Thank you **Dr. Marty Mulvihill** for mentoring me despite my GPA. I have learned a lot from you and I really need to have research as an outlet during my time at Berkeley. **Dr. Jacob Berlin**, thanks for mentoring me and believing in me—I needed it. **Dr. Greg Copeland**, thank you for making me realize I still love organic chemistry. **Dr. Kathleen Elison**, thank you for teaching me how to balance passion for research and being a normal person.

Thank you to all the friends I have made in undergraduate and graduate school. **Michelle Reyes**, thank you for being so understanding and empathetic, you are truly a kind soul. **Gina Zaghi** and **Priyanka Dadlani**, I love you both, whether it has been 2 hours or 2 year. Thank you for your support in good and bad times.

Thank you to my family old and new including the canine family. **Daisy and Frankie**, thank you for being an excuse to take walks outside and for making quarantine sweeter and more eventful. Thank you to the **Thrifts**, for welcoming me into your home and family—I have experienced nothing but love, great food and even better company. My extended family: **Edo, Aida, Karine, Rob, Emmily, and Stacey**, thank you for all your support, love, and humor. Thank you to my grandparents, **Emma and Roland Hovhannisyan**—I love you both, thank you for always supporting my education.

I also want to thank my parents and sister, **Asmik Oganesyan, Ararat Muradyan**, and **Ani Muradyan**. You were all always my biggest cheerleaders and I love you all so much for that. I am sorry I could not have given you more of my time in the last 5 years. I hope I have made it worth coming to America—I love you all.

William John Thrift you are the love of my life and I am so blessed to have met you. Grad school would be a completely different ride and I do not think I would have made it out without you. You are an inspiring person and scientist. Thank you for bringing so much happiness into my life—I love you.

Vita

Education

PhD University of California, Irvine, Chemistry *June 2015 – June 2020*

BS University of California, Berkeley, Chemistry *September 2012 – May 2014*

Research Experience

*Graduate Student Researcher***,** *UC Irvine* *June 2015 – Present*

- Managed, developed, documented and executed four research projects that aims to design novel polymeric materials that aim mimic advanced functions found in biotic systems
- Collaborated with chemical biologists to investigate and characterize novel polymeric biomaterials to delivery vehicles for RNA
- Planned team brainstorming retreat to create an environment of scientific curiosity and the promote the exchange and growth of new ideas
- Maintained laboratory instruments including size exclusion chromatography, automated column chromatography, vacuum pumps, dry solvent system, thermogravimetric analyzer

Post-Baccalaurete Researcher, City of Hope *June 2014 – August 2015*

- Synthesized and purified chromatography fluorescently labeled oligonucleotides and proteins that reduced projected costs
- Optimized orthogonal chemistries for the development of a spatially encoded library of chemicals that can be rapidly screened to identify potent therapeutics
- Improved the stability of the assembled library of therapeutics which resulted in inventorship on patent that has been out licensed to Terray Therapeutics led by my mentor and advisor

Undergraduate Student Researcher, UC Berkeley *June 2013 – May 2014*

- Identified and demonstrated the addition of calcium stearate into cellulose-based materials endows the composite with water-resistance which decreases the cost of production
- Collaborated with interdisciplinary team of engineers, chemists, architects as well as with an industrial partner, ModRoofs, to improve the durability and lower the cost of emergency shelters
- Demonstrated improved water-resistance of cellulose based materials which resulted in NSF funding of a post-doctoral student to continue the project and author a publication

Skills

- *Synthetic*: small molecule (monomers, chain-transfer agents), small molecule separation, living radical polymerization (ATRP and RAFT) inorganic and organic nanomaterials
- *Small molecule characterization:* NMR, HPLC, LC/GC-MS, elemental analysis
- *Thermal/Mechanical*: TGA, DSC, DMA, rheology, Instron
- *Spectroscopy*: FTIR, UV/Vis, Raman
- *Microscopy*: optical, fluorescent confocal, SEM, TEM of inorganic and organic materials

Teaching Experience

University of California, Irvine

- Teaching assistant for the following courses: General chemistry lab and lecture, organic chemistry lab and lecture, chemical biology lab, and graduate level polymer chemistry

Select Publications and Patents

- **Muradyan, H.,** Guan, Z. "Chemothermally Driven Out-of-equilibrium Materials for Macroscopic Motion" *ChemSystemsChem*, **2020**, DOI: 10.1002/syst.202000024.
- **Muradyan, H.** Mozhdehi, D.; Guan, Z. "Self-healing magnetic nanocomposites with robust mechanical properties and high magnetic actuation potential prepared from commodity monomers via graft-from approach" *Polym. Chem.*, **2020,** 11 (7), 1292-1297.
- Yang, D.; Eldridge, A.; Hickey, J. C.; **Muradyan, H.;** Guan, Z. "Multivalent Peptide-Functionalized Bioreducible Polymers for Cellular Delivery of Various RNAs" Biomacromolecules, **2020,** 21 (4), 1613-1624.
- Nishimua, Y.; Chung, J.; **Muradyan, H.;** Guan, Z. "Silyl Ether as a Robust and Thermally Stable Dynamic Covalent Motif for Malleable Polymer Design," *J. Am. Chem. Soc.* **2018** 1, 503-509.
- Berlin, J.; Copeland, G.; Elison, K. Muradyan, H., "Spatial Array Technology," United States
- Buckley, H. L.; Touchberry, C. H.; McKinley, J. P. Mathe, Z. S.; **Muradyan, H**.; Ling, H.; Fadadu, R. P.; Mulvihill, M. J.; Amrose, S. E., "Renewable Additives that Improve Water Resistance of Cellulose Composite Materials," *Journal of Renewable Materials*, **2017** *5*, 1-13.

Select Presentations and Invited Lectures

- "Bringing Life to Materials with Chemistry" Lecture Series at Glendale CC *May 2019*
- "Photo-triggered Change in Dynamic Properties," UC Chemical Symposium *March 2018*
- "Water-Resistant Cellulose-based Composites" ACS National meeting *August 2016*
- "Versatility Monodentate Metal-Ligand Interactions" Gordon Conference *June 2018*
- "Self-healing Magnetic Actuators," USD *September 2017*

Select Honors and Awards

- Michael E. Gebel Award for Chemistry Graduate Students (Department-wide) *May 2019*
- Loh Down on Science (LDOS) Fellowship (Campus-wide) *March 2018*
- Audience Choice TED-style Talk at the UCI AGS Symposium (Campus-wide) *April 2018*
- Eugene and Ruth Robert's Summer Academy Fellowship (State-wide) *June 2014*
- NSF REU Summer Undergraduate Research Fellowship (State-wide) *June 2012*

Professional Training and Affiliations

SciPhD. The Business of Science *October 2018*

  - Two-day workshop on effective communication and negotiation

Thermal Analysis Training *September 2016*

  - Three-day workshop on thermal analysis instrumentation

Iota Sigma Pi *June 2018 – May 2019*

  - Serve as secretary and manage the website for women in chemistry organization

Community Service

UC Irvine. Mentor Undergraduate Students *December 2018 - present*

  - Mentored undergraduate chemistry students conducting research in Guan lab

Glendale Community College. "Is a Ph.D. for *April 2016*

  - Served as a panelist and mentor to community college students

Teaching Assistant Mentor *September 2018- May 2019*

  - Serve as teaching mentor for 6 first year Ph.D. students

Abstract of Dissertation

Dynamic and Non-equilibrium Polymeric Materials
By

Hurik Muradyan

Doctor of Philosophy in Chemistry

University of California, Irvine, 2020

Professor Zhibin Guan, Chair

In nature, living systems operate far from equilibrium by consuming and dissipating energy to perform vital processes. Chapter 1 will introduce the background, history, and field of nonequilibrium systems. Biological systems use chemically derived energy to power out-of-equilibrium processes to generate complex macroscopic motion by dissipating energy at the molecular scale. In contrast, it remains a major challenge to create synthetic out-of-equilibrium systems that operate on the macroscopic scale.

In Chapter 2 we report a chemically fueled out-of-equilibrium system that can perform macroscopic actuation and do work by lifting objects. We achieve this by driving a lower critical solution temperature (LCST) transition of poly(N-isopropylacrylamide) (pNIPAAm) hydrogels with heat generated by a copper-catalyzed azide-alkyne cycloaddition (CuAAc) reaction. Upon completion of reaction, heat dissipates to the environment, and the system returns to equilibrium completing one cycle of out-of-equilibrium behavior, which can be repeated multiple cycles by adding new chemical fuels.

In Chapter 3 the groundwork from Chapter 2 is employed in efforts to achieve a self-regulating device. We set out to attach a copper catalyst in and LCST hydrogel in order to

modulate reaction rate using the change in diffusion of the chemical fuels to the active catalytic sites. Efforts to achieve self-regulation of an exothermic reaction in a 3-dimensional material *via* autonomously oscillating catalytic hydrogels is described.

In Chapter 4, we report the design, synthesis and characterization of self-healing magnetic nanocomposites prepared from readily available commodity monomers. These multi-functional materials demonstrate robust mechanical properties, with a Young's modulus of 70 MPa and over 500% extensibility. The magnetic nanocomposites also show self-healing ability, achieving 46% recovery of extensibility in 5 hours in ambient conditions while retaining high magnetic actuation with a commodity magnet.

Chapter 1: Introduction to Nonequilibrium Systems

1.1 Background

There have been tremendous advances in our ability to design and create functional materials. Prior to the emergence of modern functional materials, human society primarily used structural materials, which are employed for their load-bearing capacity. Functional materials, on the other hand, possess unique functional properties such as biological,[1] chemical,[2] electronic,[3] magnetic,[4] optical,[5] or thermal properties.[6] In the last century, major breakthroughs in the field of functional materials have brought forward revolutionary changes to our society. For example, the development of photoresists and semiconducting materials allowed for mass fabrication of field effect transistors (FETs) for integrated circuits, which are essential for all kinds of microelectronic devices such as computers, mobile phones, radios, and sensors.[7] Functional materials have also made enormous impacts in the biomedical field in the development of biomaterials for biodegradable surgical sutures,[8] drug delivery,[9] medical devices,[10] and tissue engineering.[11] Nevertheless, most manmade materials to date capitalize on thermodynamic equilibrium properties in order to ensure stability for static behavior. This is in dramatic contrast with biological systems, which mostly operate in far from equilibrium conditions.[12]

Out-of-equilibrium systems consume and dissipate energy, resulting in constant dynamics for the system over time.[13] Nonequilibrium systems consume energy in the form of chemical,[14–21] mechanical,[22] electrical,[23–25] or light energy from their surroundings.[26–29] This energy consumption can power many processes from molecular to cellular changes. Note that nonequilibrium systems dissipate energy by release energy to the surrounding environment.[13] This behavior will be discussed in detail by comparing a few different energy landscapes.

The energy landscapes of systems out-of-equilibrium are fundamentally distinct from traditional equilibrium systems (Figure 1). Systems at equilibrium exchange no energy or matter with their surroundings and accordingly, on the macroscopic level, the system does not change over time.[13] This behavior has been studied for decades and can be quantitatively described by classical thermodynamics.[30] Nonequilibrium systems, commonly referred to as out-of- or far-from-equilibrium, have a net exchange of energy and/or matter with the environment.[13] Typically we are interested in cases that result in a net loss of energy to the environment, which are referred to as dissipative systems.[31] Such nonequilibrium systems can only persist when there is a constant influx of energy from the environment.

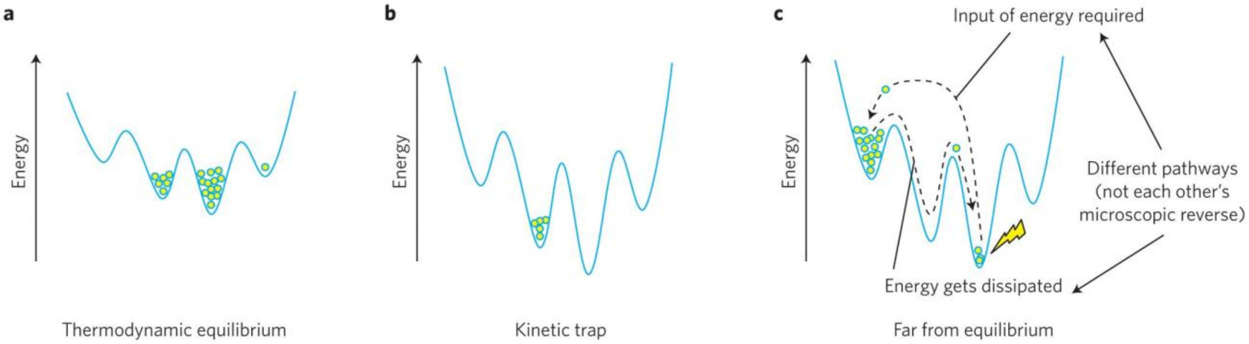

Figure 1.1 Thermodynamic and out-of-equilibrium systems. (a) Thermodynamic equilibrium where the system is in equilibrium and will remain static unless there is an input of energy. The pathway the system took to reach this state is irrelevant. (b) Kinetic trap where the state of the system is dependent on the path. (c) Far-from-equilibrium or nonequilibrium systems where the state depends on the continuous influx and dissipation of energy. Figure adapted from [32].

In designing nonequilibrium systems, the thermodynamics as well as kinetics must be controlled. Figure 1.1 graphically depicts the differences in energy landscapes between equilibrium, kinetically trapped, and nonequilibrium systems in a, b, and c, respectively.[32] First, consider an equilibrium system which resides predominantly in global energy minimum and remains there over time (Figure 1.1a).[32] Next, consider kinetically trapped systems, which differ in that they are transiently stable because these systems reside in local minima and cannot transition to the global minima (Figure 1.1b). A metastable system is closely related to a kinetically trapped system except that this system has a finite lifetime—it can transition from a local energy minimum to a global energy minimum over time. Metastable states are able to persist for some amount of time without any energy input, which marks a key difference from other nonequilibrium systems which cannot persist without energy input.[13] Lastly, nonequilibrium states are short lived and have a net flow of energy and/or matter between the system and the environment.[13] Nonequilibrium states are short lived because there must be a constant source of energy to sustain the flow of energy. The input of energy causes the system to move to a higher energy state, which is only attainable with continual fuel supply, thus over time the system dissipates this energy and moves to a lower energy state (Figure 1.1c).

Nonequilibrium processes are ubiquitous in biological systems, with the most discussed examples being actin and microtubule supramolecular assemblies. Actin is a structural protein which forms the building blocks of the actin cytoskeleton that determines the shape, mechanical properties, and motility of the cell.[12] Actin units dynamically assemble into actin filaments and disassemble by the interconversion of adenosine triphosphate (ATP) and adenosine diphosphate (ADP) *via* hydrolysis and phosphorylation.[33] Actin can exist as G-actin or F-actin, which differ in the propensity to assemble.[12] F-actin represents actin in the assembled filament form, while G-actin is the monomeric, unassembled unit. F-actin can be converted into G-actin *via* a chemically fueled nonequilibrium process.[34] The exact mechanism of disassembly remains controversial but the current understanding involves two steps: ATP hydrolysis and phosphate dissociation.[34,35] In this process, the existing actin unit becomes unstable in the filament form, which in turn with cooperative effects of neighboring units, leads to the dynamic disassembly of the filament.[34] The nonequilibrium behavior arises from the competing phosphorylation reaction of ADP to ATP, which stabilizes and results in growth of the actin filaments.

Similarly, microtubules are composed of α- and β- tubulin heterodimers that dynamically assemble and disassemble.[12] The dissipative assembly is chemically fueled with guanosine triphosphate (GTP). Much like ATP fuels actin disassembly *via* hydrolysis, GTP can be hydrolyzed to guanine diphosphate (GDP) to fuel microtubulin dissassembly.[12] When the tubulin heterodimers are assembled they bind to two GTP units. The GTP stabilizes the microtubule assembly. Upon hydrolysis of GTP to GDP, and dissociation of the phosphate the microtubule begins to curve indicating instability, which leads to disassembly.[33] The disassembly and reassembly of microtubulin to form spindle-shaped units for partitioning chromosomes is crucial for mitosis.[12] Upon completion of mitosis the monomeric units will reassemble to form the interphase microtubule network.[12] These examples demonstrate the key function and utility of chemically fueled dissipative processes in biological systems. Nonequilibrium systems constantly require energy input even when operating in homeostatic conditions. This poses the natural question: why use nonequilibrium processes to maintain stability? Nonequilibrium processes allow biological systems to more rapidly adapt and reconfigure in response to changes in their surroundings, which is advantageous for survival.[36] Let us take a static actin assembly as an example. If the environment abruptly changes such that assembly in a new location is necessary, the disassembly and reassembly would be much more energy demanding as compared to a nonequilibrium assembly. Given living systems work in concert with one another, biological systems must be able to quickly response and adapt—nonequilibrium processes allow for such rapid adaptation.

1.2 History of studying nonequilibrium systems

While biological systems have been operating far from equilibrium for millions of years, scientific investigation of nonequilibrium systems did not begin until the early 1900's. In the 19th century scientists focused on studying thermodynamics in terms of the state functions of energy and entropy.[37] This is described by the first and second laws of thermodynamics, stating that energy must be conserved, and entropy for an isolated system must not decrease, respectively.[38] Together these laws allowed for the study of processes which are infinitely slow and reversible, limiting analysis to systems at equilibrium. Then, at the turn of the twentieth century Lar Onsager and Ilya Prigogine made significant contributions on thermodynamics of irreversible processes which have profound implications on nonequilibrium systems.[37] The initial work by Onsager in 1930's laid the groundwork for the thermodynamics of irreversible processes for which he received the Nobel Prize in chemistry in 1968.[39] Building upon this work, Prigogine introduced the notion of treating an inhomogeneous system as if it were composed of many parts that were in equilibrium locally, which was supported by existing theories in statistical physics.[40] Prigogine was awarded the Noble Prize in chemistry in 1977 for his contributions to nonequilibrium thermodynamics, particularly for his theories on dissipative structures—a term he coined.[37]

It was not until the early 1960's when scientists realized that experimental nonequilibrium systems have interesting new properties. A prominent example being oscillating chemical reactions, in which the concentration of chemical species changes in an oscillatory fashion over time.[37] Concurrently, the field of dissipative systems began to emerge as scientists discovered that nonequilibrium processes can be used for self-organization.[31] In the 1990's, pivotal work by Chris Jarzynski and Gavin Crooks extended the second law of thermodynamics to better understand thermodynamic constraints on nonequilibrium behavior.[41] While physicists and physical chemists continue to study nonequilibrium systems and develop guiding principles for understanding biological processes, synthetic chemists and materials scientists have begun to mimic these biological nonequilibrium processes using synthetic systems.[37]

There is a long history in science of bioinspiration. Inspiration from biology has given rise to advances in a variety of fields including drug delivery,[9] structure coloration,[42] sustainable building design,[43] and materials design.[44] Until recently bioinspired research largely focused on systems at equilibrium. The pursuit of synthetic nonequilibrium systems gained steam in the 1980s with the inception of the field of molecular motors (discussed in more detail in section 1.6).[32,45,46] The ability to mimic nonequilibrium behavior could enable materials to adapt, learn, achieve homeostasis, and interact with their surrounds and even living systems. Despite these advances, nonequilibrium systems have proven to be challenging to mimic in synthetic systems. This is because many of the governing principles and the theoretical framework of nonequilibrium systems is still poorly understood.

1.3 Distinction between nonequilibrium systems and other closely related systems

To facilitate further in-depth discussions, it is helpful to compare nonequilibrium materials with other closely related systems such as stimuli-responsive, dynamic, and adaptive materials. However, keep in mind that some of these concepts are intertwined with partial overlaps and the delineations for a complex, relatively new, and broad field are still open to discussion and interpretation.

One extensively studied system is stimuli-responsive materials consisting of small molecule or polymer-based materials that respond to various external stimuli such as temperature,[47] pH,[48] solvent polarity,[49] light,[50] mechanical force,[51] or magnetic field,[4] etc. For such systems, an external stimulus triggers the switch from one equilibrium state to a new equilibrium state.[52] This switch is usually accompanied with an associated change in properties including color,[53] physical phase,[54] surface adhesion,[55] or hydrophobicity[56] among other properties. It should be noted that the new state is also at equilibrium, thus it will remain static until a counter trigger is introduced.[36] For nonequilibrium systems, however, the trigger (energy input) is transient because the energy it provides is constantly consumed to sustain the process. As soon as the energy supply stops, the unstable system quickly goes back to the thermodynamic minimum energy state or ends up in a kinetic trap (Figure 1.1). Thus, in nonequilibrium cases there is no need to introduce a counter trigger to move the system back to the starting point.

As pointed out by Walther,[36] sometimes the distinctions between stimuli-responsive and nonequilibrium materials are subtle. This can be illustrated in light and temperature responsive azobenzene derivatives *via* the *cis*/*trans* isomerization. Upon irradiation with light of one wavelength (l_1), the thermodynamically more stable *trans* form isomerizes to its metastable *cis* form, which can thermally relax back to its thermodynamic minimum state if there is sufficient thermal energy. In this sense, it behaves more like an out-of-equilibrium system because it requires constant light energy input to sustain at the *cis* form. At relatively low temperature the *cis* to *trans* transition can also be achieved using a counter trigger by irradiating with light of another wavelength (l_2). In this scenario, the system acts as a stimuli-responsive system because it requires a trigger and a counter trigger to switch back and forth between two stable equilibrium states. We see that depending on context, this system may either be classified as a stimuli-responsive or nonequilibrium system. This nuance has made it difficult to implement nomenclature that draws a strict line between these fields. Many define nonequilibrium as any system that dissipates energy; while this definition is sufficient for constructing the theoretical framework for the thermodynamics at play, it does not provide a clear outline for practical demonstrations of nonequilibrium processes.[13,36] It can be argued that better distinctions will arise as the field progresses to more closely mimic biological complexity.

Another commonly used and more general term is dynamic materials. Dynamic materials refer to materials having dynamic properties that change over time.[57] By this definition, nonequilibrium systems are all inherently dynamic. Stimuli-responsive materials are also dynamic because they change over time in response to a triggered stimulus.[58] The term dynamic is also applied to the field of self-healing materials which usually consists of polymeric materials crosslinked with dynamic supramolecular or covalent bonds.[57] Dynamic bonds can break and reform enabling self-healing behavior and the ability to be reprocessed. Many dynamic materials can also be classified as stimuli responsive materials because the dynamic exchange can be triggered by an external stimulus such as increased temperature, or addition of solvents. Noteworthy subfields include shape-memory polymers capable of generating motion in response to a change in temperature,[54] and covalent adaptable networks (CANs)[59] which can be reprocessed at elevated temperatures.

Finally, adaptive materials are similar in broadness with dynamic materials but come with an added layer of nuance. Many in the field refer to all stimuli-responsive materials as adaptive because the systems adapt to a change in the environment; however, the field has progressed to incorporate higher levels of complexity. The increased complexity often is in the form of responses that are proportional to the stimuli-intensity, rather than a simple on/off switch. Complexity can also come in the form of combining multiple stimuli-responsive features to construct logic-gates to program more complex response modes.[36] Certain systems with more complex levels of adaptability can exhibit a change in function such as autonomous self-regulation.[60] These new levels of hierarchy, organization and complexity have not been accompanied by new concrete vocabulary that is accepted throughout the field. This has unfortunately given rise to ambiguity. The term adaptive is commonly used instead of stimuli-responsive when the system has some higher level of complexity than a simple trigger from one state to another.

1.4 Sources of energy used in synthetic nonequilibrium systems

In bioinspired design of synthetic nonequilibrium systems, a diverse sources of energy such as chemicals,[14–21] light, [26–29] current, [23–25] heat,[61] and mechanical energy[22] have been used to power these systems. In this section the major energy sources will be briefly introduced.

Chemically driven nonequilibrium systems use small molecules, biomacromolecules, or combinations of the two. Compared to other energy sources, chemical fuels (such as ATP hydrolysis and phosphorylation) have relatively high energy density and are used ubiquitously in biology, making them desirable targets for biomimicry. Small molecule-based fuels capitalize on irreversible competing reactions such as alkyation/hydrolysis,[14] thioester exchange,[15] and reduction/oxidation to achieve transient self-assembly.[16] This sort of competing opposing reactions parallels a common approach in biology of hydrolysis and phosphorylation as described in section 1.1. Alternatively, small molecule fuels can act on molecular motors to induce rotation or linear motion.[17] The molecular motor approach, while conceptually quite elegant, struggles to extend this behavior past the molecular scale. On the other hand, clock reactions such as the Belousov-Zhabotinsky (BZ) reaction can be used to achieve self-oscillating hydrogels, even on the macroscopic scale.[18] Another approach uses phoretic effects that yield gradients of small molecules on the nanoscale that drive active collective motion of particles.[62] The phoretic approach can be compared to nature's use of ion channels to regulate ionic strength.[12] However synthetic mimics have not yet been able to replicate that level of control over motion. Taking further inspiration from biology, biomacromolecules have also been leveraged to fuel nonequilibrium behavior through processes such as DNA strand displacement.[19] More commonly, biomacromolecules are often used in combination with small molecules *via* enzymatic conversion of small molecule substrates.[21] Combination systems also use oligonucleotides, enzymes and small molecules to drive nonequilibrium behavior.[20]

Light and heat can also serve as fuel for nonequilibrium processes. The use of light as a fuel can be advantageous because it enables spatiotemporal control. Additionally, light fuel can be administered remotely in a non-contact fashion, which can be advantageous for some applications. Light responsiveness is often achieved *via* photo-active small molecule which upon irradiation can cause a change in pH or assembly propensity.[26–28] For example, azobenzene is a common motif to incorporate into light driven systems due to the photo-triggered *cis/trans* isomerization that induces self-assembly. [26,27] Spiropyran is another common photo-active molecule used to impart light driven dissipative behavior, popular due to its reactivity at optical wavelengths.[63] Photoactive molecules can be used to achieve nonequilibrium behavior in a variety of forms such as: transient change in optical properties,[64] molecular motion, [65] or active colloidal motion.[62] In one example a pH responsive colloidal crystal is disassembled through the use of a photoacid causing transient changes in pH.[28] Photo-active molecules can also be used to achieve molecular motion *via* a ratchet mechanism that uses Brownian fluctuations on an anisotropic molecule in isothermal media to enable directional molecular motion.[66,67] There are very few examples of purely thermally driven systems; however one approach uses shape memory polymers to achieve autonomous actuation, this example is discussed in detail in 1.9.2.[61]

Electricity can also be used as a source of energy to power nonequilibrium behavior. Electrochemistry can be leveraged in achieve nonequilibrium behavior in molecular motor.[24] In one example, electrochemical oxidation of benzidine results a change in net charge, facilitating molecular shutting (described in detail in section 1.5).[24] Electricity fueled molecular motion can also be achieved using prochiral molecules on a copper surface.[25] Electric fields can also be used to fuel active motion of asymmetric colloidal material driven be electrostatic forces.[23]

Mechanical energy can also be used to fuel nonequilibrium behavior. Early examples, include material processing such as milling, achieved nonequilibrium alloy phases.[68,69] More recently, mechanical energy was used to bias the assembly of peptides into fiber structures.[22] Mechanically driven surface dynamics in hydrogel materials have also given rise to nonequilibrium behavior such as elastic creasing instabilities.[70]

1.5 Modes of operation in synthetic nonequilibrium systems

The input of external energy or fuel can achieve nonequilibrium behavior through several modes of operation, here we outline the main modes of fuel operation. Fuel can induce a change in chemical characteristics of the substrates which results in molecular motion or a change in self-assembly propensity. Additionally, fuel can act upon the media to change the local and global chemical composition, resulting in changes in assembly or colloidal motion.

First off, fuel can directly change the chemical characteristics of small molecules to yield nonequilibrium behavior in the form of molecular motion. The addition of fuel can change the chemical characteristics *via* a change in conformation or configuration,[71] charge,[72] or sterics.[73] A common approach uses an input of energy to facilitate *cis/tran* isomerization of an alkenes,[74] or imines to generate rotational molecular motion.[75] Fuel can also generate directional molecular motion by changing the charge,[24] or protonation state.[76] The addition of fuel can also induce a change in sterics which can give rise to directional molecular motion.[73]

The fuel induced direct change in chemical characteristics can also lead to dissipative supramolecular assembly by altering the chemical characteristics of monomeric building blocks, controlling the self-assembly behavior. Here, the addition of the fuel causes a change to the assembly behavior of a small molecule by changing its charge state through the use of redox chemistry,[77] or alkylating agents.[78] Changes in molecular polarity can also induce dissipative assembly *via* transient anhydride formation using carbodiimide activating agents as the fuel.[79] Alternatively, changes in dipole moment induced by photo-triggered isomerization can alter long range order as seen in liquid crystalline systems.[80] The fuel input can also change properties such as binding affinity as seen in micellular systems.[81]

In contrast, fuel can also act upon the surrounding media to change the chemical composition to achieve nonequilibrium behavior. Changes in chemical composition can be achieved by the addition of acids or bases to cause a transient change of pH which can result in directional molecular motion,[76] or transient colloidal assembly,[82] and disassembly.[28] The chemical composition can also be changed *via* reaction-diffusion processes that generate chemical oscillators, known as clock reactions.[16,83] The change in the chemical composition can also give rise to nonequilibrium behavior such as oscillatory changes in the swelling of a hydrogel.[84] There has also been recent work that uses imbalances in diffusion rates during interfacial polymerization to generate synthetic Turing patterns without the use of existing clock reactions.[85]

Furthermore, fuel can act on surrounding media to change the chemical composition locally to achieve nonequilibrium behavior in the form of active colloidal motion. Local changes in chemical composition can be achieved *via* a colloidal catalysis.[86] In the case of catalytically active colloids, the chemical reaction only occurs at the surface of the particle and thus the change in chemical composition is transiently localized the surface of the colloid. For example, hydrogen peroxide decomposition can be used to achieve directional colloidal motion.[62] Asymmetric catalytic colloids can be used to generate rotational colloidal motion.[87] Colloids that leach metal ions can also be used to achieve colloidal motion.[88]

In the following sections (section 1.6 – 1.10), we will concisely summarize some major synthetic nonequilibrium material systems by highlighting some representative examples.

1.6 Molecular motor based nonequilibrium systems

In the legendary talk "There's plenty of room at the bottom," Richard Feynman outlined the vast opportunities available to scientists at the molecular and nanoscale.[89] The field of molecular machines has been an active area of research since the 1980's. The most seminal contributions to this field are attributed to Jean-Pierre Sauvage, Sir J. Fraser Stoddart, and Bernard L. Feringa, who shared the Nobel Prize in Chemistry in 2016 for their work on the design, synthesis, and studies of molecular machines.

First let us consider the methods of achieving motion of molecular machines. Inherent differences from macroscopic machines arise due to the large change in scale.[45] For this reason, a ratchet mechanism is often used. In short, a ratchet mechanism relies on anisotropic molecules whose Brownian fluctuations will themselves be anisotropic, enabling directional molecular motion.[66,67] The ratchet mechanism can be used because Brownian motion operates at these short length scales, making it is much easier to absorb energy using non-equilibrium fluctuations in the environment.[90] The motion of molecular motors is considered a nonequilibrium process because the motion is driven by an input of energy such as thermal or chemical energy, which is then dissipated into the surrounding *via* bond rotation. This is different from equilibrium bond rotation because in equilibrium conditions the rotation is normalized due to the random nature. In this section key classes of molecular motors will be discussed.

First, let us discuss unidirectional rotary molecular motors, whose motion is derived from rotation about a C-C single bond. A prominent example includes triptycenes, which are organic molecules with a three-blade architecture and a C-C single bond that serves as the rotational axis for movement (Figure 1.2a). Upon attachment of a bulky substituent, [4] helicene, the rotational energy associated for the C-C single bond increases to ~25 kcal/mol which is significantly higher than typical C-C bonds (~3-5 kcal/mol).[71] The higher rotational energy serves as an opportunity to bias directional motion, achieving a molecular motor. It should be noted that without the bulky [4] helicene the triptycene can rotate; however, this rotation occurs equally in both directions, thus this motion is not an nonequilibrium process, and directional motion is not achieved.[71] Through the attachment of an aniline motif to one of the three-blades on the triptycene, phosgene can be used as the chemical fuel to bias molecular rotation.[71] The addition of phosgene results in isothiocyanate formation. The rotational movement is equivalent in both directions; however, by tethering an alcohol to the [4] helicene, the rotation in one direction becomes biased due to the trapping of the isothiocyante *via* intramolecular urethane formation.[71] This work was the first example of a unidirectional rotary molecular machine. Biaryl sulfoxides have also been used for achieving unidirectional rotary motion about a C-C single bonds and have extended the rotation from 120º to 360º.[91] Sterically bulkly substituents in the ortho positions restrict rotation.[91] The system can be fueled using organometallic chemistry that triggers shuttling between Pd(0) and Pd(II) oxidations states that selectively bind to the biaryl sulfoxides.[91] This binding directs C-H activation and subsequently oxidative addition to achieve rotary motion.

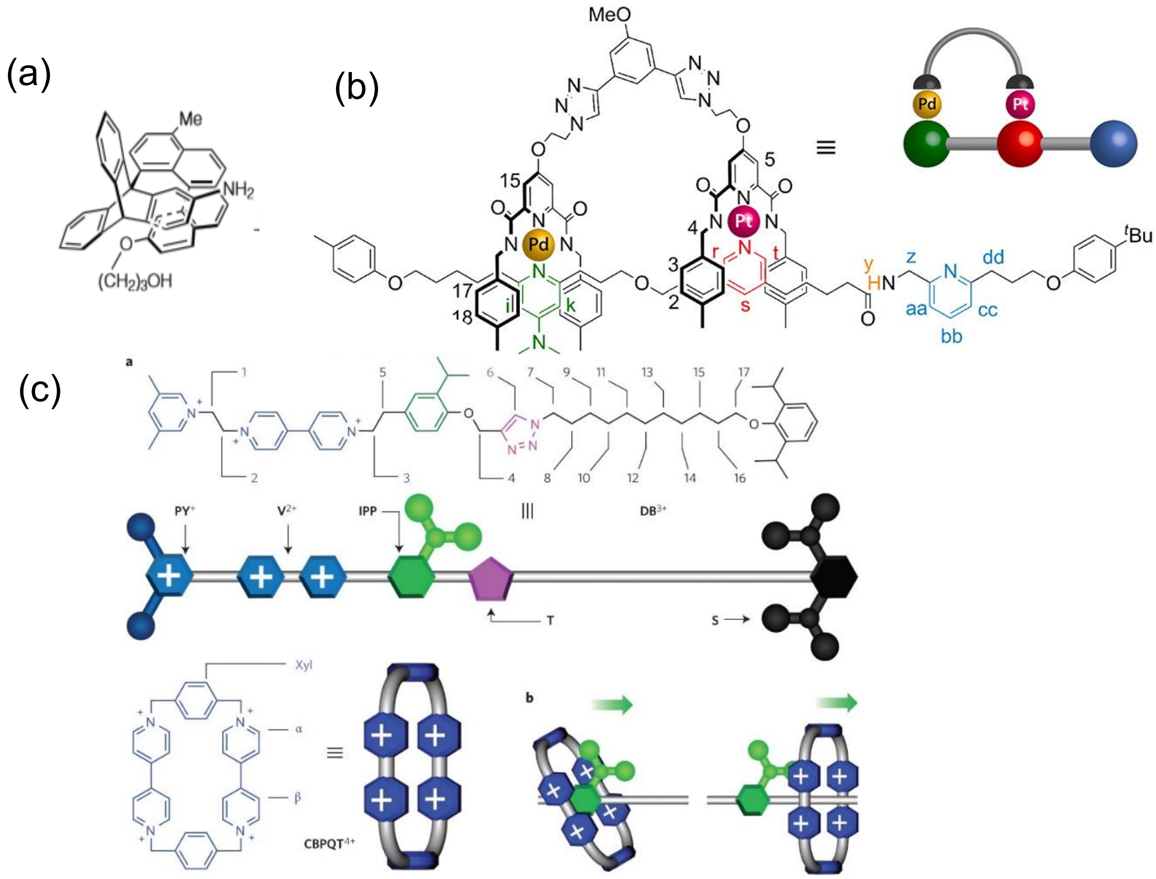

Figure 1.2 Molecular motor scaffolds of rotary motors, biped walkers and rotaxanes. (a) Structure for achieving unidirectional rotary molecular motors derived from rotation about a C-C single bond. Figure adapted from [71]. (b) Structure and schematic for the development of molecular bipeds. The Pt(II) and Pd(II) complexes are highlight in pink and gold circles, respectively. The N-heterocyclic ligands are shown in black. The 4-dimethylaminopyridine (DMAP) unit is shown in green and binds to the Pd complex. Molecular motion is achieved via protonation of the DMAP unit. Figure adapted from [76]. (c) Rotaxane based molecular motor capable of demonstrating 2 cycles of operation to drive a bead shown in blue that is composed of tetracationic viologen macrocycle. The bead is threaded onto an axle composed of a dicationic viologen, shown in blue, which in reducing conditions binds to the bead to allow for threading. Under oxidative conditions the viologens repel and result in locking of the bead on the left of the isopropylphenyl “speed bump” shown in green, which can be overcome over time. This process can be repeated an additional cycle. Figure adapted from [72].

Organometallic chemistry has also found utility in the field of molecular motors for the development of molecular bipeds or “walkers.” In one example, the “feet” of the bipeds are composed of Pt(II) and Pd(II) complexes that serve as binding sites for ligands (Figure 1.2b). N-heterocycles are used to ensure an open coordination site in the square planar geometry. An important design feature of this system is that Pd(II) binding is reversible while Pt(II) binding remains locked. Through the reversible protonation/deprotonation of 4-dimethylyaminopyridine, the attachment of the Pd(II) foot can be modulated, thus demonstrating proton fueled molecular walkers. This design allowed for demonstration of a pH fueled molecular biped.[76] The motion generated by the molecular bipeds is quite similar to the walking mechanism of motor proteins, such as the kinesin protein which moves along microtubule filaments *via* ATP hydrolysis.[12]

Rotaxanes are another important and large class of molecule motors that are based on mechanically interlocked molecules (MIMs).[92,93] Rotaxanes are composed of three components, the thread (or axle), the bead (or macrocycle), and two chain stoppers.[92] The thread is a linear molecule onto which a macrocycle can be threaded. The bead is held in place due to the chain stoppers which consists of sterically bulky substituents that prevent the bead from dethreading.[92] In many molecular motor designs, the axle is also designed to have binding sites to induce docking points for the bead on the thread. In one example by Stoddart, the bead contains a tetracation of bipyridinium units—referred to as viologens—tethered by p-xylyl spacers.[24] The axle is composed of biphenol and benzidine, which serve as the electron donors into the positively charged bead.[24] These binding units are spaced *via* an ethylene glycol chain and capped at each end with sterically bulky stoppers.[24] The motor can be fueled electrically *via* the oxidation of benzidine which generates a dication, locking the bead onto the biphenol docking point. Trifluoracetic acid can also be used as a chemical fuel *via* protonation of the benzidine in a similar fashion as described above.[24] Others have shown rotaxane based molecular motors with 2 cycles of operation that drive a threaded bead away from equilibrium towards a higher local concentration, which is a more energetically demanding state (Figure 1.2c).[72] Similarly, the bead is composed of tetracationic viologen units. The axle has cationic viologen units which, under reducing conditions, result in stabilizing radical-radical pimerization allowing for threading of the bead onto the axle.[72] After threading, oxidization drives the systems to a very high potential energy locking in the viologen rings onto the axle due to the repulsive forces between the oxidized viologen on one side and a sterically bulky isopropylphenyl “speed bump.”[72] It should be noted that in this state, dethreading of the bead and axle is thermodynamically favored but kinetically disfavored.[72] The isopropylphenyl speed bump can be overcome given enough time due to co-conformational rearrangements.[72] Upon exposure to reducing conditions this cycle can be repeated to thread another bead onto the axle creating an increase in the local concentration of the beads which is energetically quite demanding.[72] This demonstration of a molecular pump, more closely mimics biological nonequilibrium systems that are able to use chemical fuels to achieve energetically demanding changes in local concentration.

Rotaxanes can also be powered using a light driven asymmetric rotaxane. In one example, one side of the axle contains an azobenezene motif that allows for photo-triggered E/Z isomerization.[65] The axle has an ammonium-based docking site in the middle, and a methylcyclopentyl stopper on the other end.[65] The naphthene crown ether-based macrocycle is used as the bead and can be threaded onto the axle when the azobenzene in is the E form.[65] In the Z form the beads is unable to dethread from the axle allowing for controlled threading and dethreading using light.[65] By using light as a source of fuel the nonequilibrium behavior has the potential to be controlled in a spatiotemporal fashion, bringing molecular machines closer to mimicking the complexity found in biological systems.

Catenanes are another class of MIMs that have received significant attention in the field of molecular motors. Catenanes are molecular systems composed of at least two topologically linked macrocycles.[92] Jean-Pierre Sauvage was an early pioneer of the design and synthesis of catenane based molecular motors.[94] In general, similar design strategies can be used as seen in rotaxanes such as the use of bulk substituents as blocking agents and noncovalent interactions as binding sites. To describe motion of interlocked molecules it becomes important to establish nomenclature of each macrocycle. Typically, the larger macrocycle in the system is referred to as the track (akin to the thread component of rotaxanes) and the smaller macrocycle will move long this track. In one example, autonomous molecular motion is achieved *via* a catenane based system using chemical fuels.[73] Here, fumaramide residues on the track (larger macrocycle) allow for binding to benzylic amides on the smaller macrocycle (Figure 1.3a).[73] The molecular motion of the smaller macrocycle on the track is powered by two competing reactions: the carbonate-forming reaction using 9-fluorenylmethyoxycarbonyl chloride, and the hydrolysis of the carbonate. The carbonation reaction introduces a blocking agent in the form of a sterically bulky 9-fluorenylmethyoxycarbonate, which can then be removed *via* hydrolysis.[73] The hydrolysis reaction

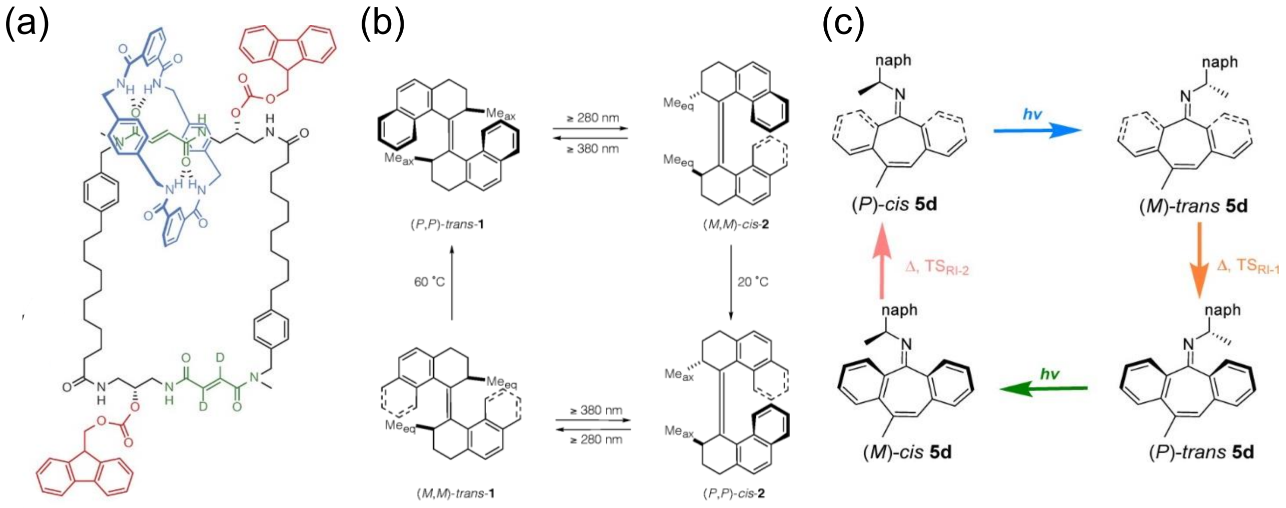

Figure 1.3 Molecular motor scaffolds of catenanes, and rotatory motors based on alkene and imines. (a) Catenane based molecular motor composed of a track with fumaramide residues, shown in green, and sterically hindered blocking agents shown in red. The bead shown in blue can be driven via pyridine catalyzed carbonate-forming reaction using 9-fluorenylmethyoxycarbonyl as the chemical fuel. Figure adapted from [73]. (b) Overcrowded alkene molecular machine capable of achieving 360º rotation in 4 consecutive steps. Photoinduced isomerization results in from the (P,P)-trans-1 to the (MM)-cis-2 form helical inversion to yield (P,P)-cis-2. Further light irradiation yields (M,M)-trans-1 which upon heating regenerates (P,P)-trans-1. Figure adapted from [74]. (c) Chiral N-alkyl imine based molecular motors that use light triggered isomerization coupled with ring inversion to achieve rotary motion. Figure adapted from [75].

kinetics remain constant despite the position of the macrocycle relative to the track; however, for the carbonation reaction, the kinetics depend on the relative location of the macrocycle.[73] When the fumaramide groups on the macrocycle are close in proximity to the hydroxyl, nucleophilic attack is suppressed—this effect results in dissimilar carbonation reactions rates giving rise to net directional motion of the ring on the track.[73] This work demonstrates the use of competing carbonation and hydrolysis reaction using 9-fluorenylmethyoxycarbonyl chloride as a chemical fuel to achieve continuous autonomous motion, marking an advancement in the field from the stepwise motion previously described.[73]

Another class of molecular machines employs overcrowded alkenes and uses *cis* to *trans* isomerization to achieve motion. In the pioneering work in 1999, Feringa demonstrated light driven isomerization to achieve 360º rotation in 4 consecutive steps by using a sterically hindered alkene as the axis for rotation.[74] The achieved monodirectional rotation hinges on two chiral centers which allows for temperature-controlled helicity inversions.[74] Specifically, by irradiation with one light (λ_{max} ~280 nm), the isomerization from the *trans* to the *cis* form is achieved and the axial methyls go to the equatorial positions (Figure 1.3b).[74] At 20 ºC, the helicity spontaneously inverts, resulting in axial methyls.[74] Upon irradiation with another light (λ_{max} ~380 nm), *cis* to *trans* isomerization occurs and results in equatorial methyls; however, upon increasing temperature, inversion results axial methyls. The spontaneous inversion blocks the reverse rotation and thus ensures that the four individual steps add up to one full rotation in one direction only.[74] This design was later incorporated into a liquid crystalline matrix to induce light driven rotation that manifests on the microscale.[95] This was accomplished by irradiating a liquid crystal sample doped with an overcrowded alkene molecular motor, to achieve rotation of the chiral motor.[95] The rotation of the chiral motor results in reorganization of the liquid crystal which manifests in rotation on macroscopic scale, marking a significant advancement in the ability to translate molecular scale motion to microscale motion.[95]

Chiral N-alky imines have also attracted attention in the field of molecular motors due to facile synthetic routes, the ability to control E/Z isomerization to generate rotational motion, like the crowded alkene motors described previously. The isomerization rate can be tuned over 9 orders of magnitude by varying the N-substitution.[75] These molecular motors can be accessed in an orthogonal two-step mode of E/Z isomerization. Additionally, by coupling the isomerization to a ring inversion, a four-step rotation can also be accessed (Figure 1.3c).[75] This is a noteworthy step in the field as it expanded the scope of molecular motors from sterically congested alkenes to imines which are synthetically more easily accessed. Building on these studies chiral N-alkyl imine based molecular motors were later incorporated into hydrogel materials to yield macroscopic contraction in response to the phototriggered E/Z-isomerization.[96]

1.7. Dissipative Supramolecular Assembly

Dissipative supramolecular assembly has garnered significant attention in the field of nonequilibrium materials due to its close similarity to biological out-of-equilibrium systems such as actin and microtubules.[13] The reversible nature of the noncovalent interactions that hold supramolecular assemblies together allows for the introduction of dissipative behavior. Frequently the dissipative behavior manifests in transient self-assembly or transient changes in previously assembled systems. The canonical biological examples of actin and microtubules both elegantly use chemically fueled dissipative self-assembly to sustain vital cellular processes.[12] For this reason, dissipative self-assembly are important in the biomimetic community. In 2010 the use of supramolecular assembly took off when Boekhoven *et al.* demonstrated the transient self-assembly of small molecule gelators by using competing irreversible alkylating and hydrolysis reactions.[14] Since then, other chemically driven,[14–16,97] as well as light driven nonequilibrium supramolecular systems have emerged.[26,95,98] Alternative approaches have been developed including the use of clock reactions,[99,100] as well as biomacromolecules such as oligonucleotides and enzymes.[20,21] Prominent examples of these approaches are discussed below.

The use of competing irreversible reactions is prevalent in chemically driven nonequilibrium supramolecular assemblies. Commonly, the competing reactions alter the assembly behavior of small molecules such that a non-assembling molecule is converted to a small molecule gelator, while the opposing reaction converts the small molecule gelator back to the non-assembling form. This approach results in transient supramolecular assembly which gives rise to transient hydrogel formation. The source of energy in these nonequilibrium supramolecular assemblies derives from the competing reactions used to fuel the process. When the source of fuel is depleted the system goes back to equilibrium—depending on the specific conditions, equilibrium may be the assembled or disassembled form.

The pioneering work by Boekhoven *et al.* in 2010 used competing alkylation *via* methyl iodine and hydrolysis in basic conditions to drive nonequilibrium behavior (Figure 1.4a).[14] Anhydride formation and hydrolysis has also yielded chemically-driven dissipative supramolecular assembly (Figure 1.4b).[97] Carbodiimide coupling agents can be used as the chemical fuel for transformation of carboxylates into anhydrides.[79,97] The anhydrides can only be formed transiently before degradation *via* hydrolysis.[97] Others have reported intermolecular thioester exchange, fueled by the addition of highly reactive thioesters, followed by spontaneous release of lactams as waste.[15] Redox chemistry has also been explored by using competing reduction with sodium dithionite and air oxidations reaction on perylene diimide (PDI) derivatives to yield nonequilibrium transient assembly.[16] More recently, milder redox chemistries have been employed by Ogden *et al.* to achieve transient self-assembly.[101] These examples demonstrate the expanding scope of chemical reactions used to achieve dissipative assembly.

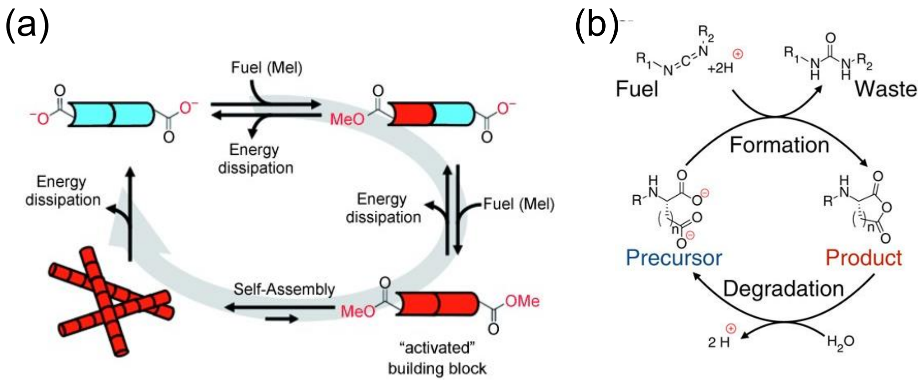

Figure 1.4 Chemically fueled dissipative assemblies (a) Dissipative cycle of chemically fueled supramolecular assembly using strong alkylating agents in basic conditions to yield transient assemblies of small molecule gelators. Figure adapted from [14]. (b) Dissipative cycle of chemically driven supramolecular assembly using carbodiimide chemistry to yield transient anhydride formation follow by degradation via hydrolysis. Figure adapted from [97].

Chemically driven supramolecular systems have also used biomolecules and biomacromolecules to achieve nonequilibrium behavior. Fundamentally, these examples are quite similar in the use of competing irreversible reactions; however, in these cases the assembly behavior of biomolecules, such as peptides and oligonucleotides are altered.[20,21] In one example, the competing reactions of catalytic transacylation and hydrolysis result in nonequilibrium dissipative assembly and subsequently transient gelation of peptide amphiphiles.[21] The transacylation and hydrolysis reactions were accomplished enzymatically with chymotrypsin and thermolysin, respectively, to yield transient gelation.[21] In another example, DNA is used as the chemical fuel in conjugation with RNA and RNA polymerase to achieve autonomous dynamic self-assembly of DNA nanotubes.[20] By incorporating biomacromolecules scientists have been able to more closely mimic biological systems, as evident in comparing the autonomous dissipative assembly of DNA nanotubes to actin assembly.

Chemically driven nonequilibrium systems can also be fueled by reaction-diffusion processes. Reaction-diffusion processes give rise to chemical oscillators (often referred to as clock reactions) in which the chemical composition changes in a oscillatory fashion over time.[16] Chemical oscillators can also give rise to emergent behavior such as the formation of Turing patterns.[102] Coupling the change in chemical composition to self-assembly behavior has resulted in nonequilibrium behavior. Clock reactions such as the Belousov-Zhabotinsky,[18] iodine clock,[99] and methylene glycol/sulfite/gluconolactone reactions have been employed to generate dissipative assemblies.[103] In one example, an iodine clock reaction is coupled to an iodine-responsive polymer to generate transient self-assembly of the polymers.[99] The polymer is composed of a block copolymer with one hydrophilic block and an iodine responsive block composed of polyethenylene glycol (PEG).[99] The addition of iodine to PEG polymers results in noncovalent interactions that increase the hydrophobicity of the polymer.[99] The change in hydrophilicity results in a change in the self-assembly behavior of the polymers. Thus, upon changes in concentration of iodine as the clock reaction proceeds, the self-assembly behavior of the polymer also changes.[99] While the use of clock reactions has yielded a number of nonequilibrium system with unseen properties such as macroscopic autonomous motion,[100] the reliance on clock reactions limits the scope of this approach.

Light driven nonequilibrium supramolecular assemblies have also been demonstrated. Light fueled systems have the advantage of operating without the addition of chemical reagents and can potentially provide spatiotemporal control of the self-assembly. Azobenzenes exbibit a light triggered *trans* to *cis* isomerization that has been employed to achieve dissipative self-assembly.[26] The dissipative self-assembly is accomplished by using dicarboxylic acid containing azobenezene derivatives that in the *cis* form undergo self-assembly into cyclic tetramer, which further aggregate into rod-like structures, while the *trans* form assembles into linear head-to-tail structures.[26] Thus by irradiating a solution of the *trans*-azobenenze derivatives, the *trans* to *cis* isomerization drives the aggregation of these assemblies.[26] Here, the source of energy is the light, thus, when light irradiation is stopped these assemblies then undergo dissipative disassembly due to the thermally induced relaxation back to the *trans* form.[26] Alternative approaches use dithienylcyclopentene as a photochromic switch that has an associated sol-gel transition due to the transient assembly.[98] Similar to the aforementioned azobenzene motif, liquid crystals can be prepared using supramolecular assembly of the azobenezene and through UV irradiation the phase of the liquid crystal can be transiently altered.[80] Liquid crystalline materials have also had a notable presence in light fueled nonequilibrium systems due to the ability to translate molecular motion to the colloidal and microscale—a task that remains a challenge in disordered systems. Liquid crystals have been used in conjugation with C-C single bond rotary molecular motors to achieve motion of a cholesteric liquid crystal on the order of 50 um.[95]

1.8 Dissipative colloidal assembly

Dissipative colloidal self-assembly is another area of pursuit in the field of nonequilibrium materials. Compared to dissipative assembly of molecular building blocks, operating on the colloidal scale using molecular fuels has an added layer of hierarchy due to the increase in scale from small molecule to nano- and microscale. Most of the approaches capitalize on similar driving forces such as the use of competing irreversible reactions,[81] clock reactions,[104] and photo triggered changes in chemical composition.[105] There are also new methodologies unique to the colloidal scale that capitalize on chemical,[87] magnetic, [106] and phoretic properties of colloids.[88] In this section key approaches for achieving nonequilibrium colloidal systems such as transient aggregation,[104] assembly, [81] and active motion will be discussed.[107]

1.8.1 Chemically driven dissipative colloidal assembly

To begin we will look at an example that lies at the interface of supramolecular assembly and colloidal assembly. In the work by Maiti *et al.*, supramolecular interactions between ATP and surfactant molecules result in the transient assembly of micelles, which are amphiphilic colloids. The building blocks of the micelles are amphiphilic molecules composed of a hydrophobic alkyl chain with a 1,4,7-triazacyclononane●Zn^{2+} head group. ATP stabilizes the micelle assemblies *via* favorable multivalent ionic interactions between the anionic phosphate motif of ATP and the cationic charge of the amphiphile headgroup, yielding a stable micellar solution (Figure 1.5a). To achieve transient nonequilibrium behavior, hydrolysis of ATP is introduced as a competing and opposing pathway. This is accomplished via addition of an enzyme, potato apyrase, which hydrolyzes ATP into adenosine 5'-monophosphate (AMP) and orthophosphate. AMP and orthophosphate cannot stabilize the amphiphilic aggregates, resulting in disassembly of micelles.[81] This work demonstrates the use of transient supramolecular interactions via small molecule and enzymatic processes to achieve dissipative assembly of micelles.

Nonequilibrium colloidal assembly can also be fueled *via* other sources of chemical fuels. For example, the previously described method that uses opposing chemical reactions to achieve transient supramolecular assembly (Section 1.7) can be used in a colloidal system to achieve transient colloidal assembly.[109] Starting with a colloidal suspension of microparticles with ~750 nm diameter and stabilized by the electrostatic repulsion due to negatively charged carboxylates on the particle surface, the carboxylates can be methylated using strong alkylating agent such as methylsulfate.[109] The methylation increases the hydrophobicity and leads to aggregation. The aggregation is transient due to the competing hydrolysis reaction that reforms the negatively charged carboxylate, which disperse the aggregates.[109] Transient aggregation can also be

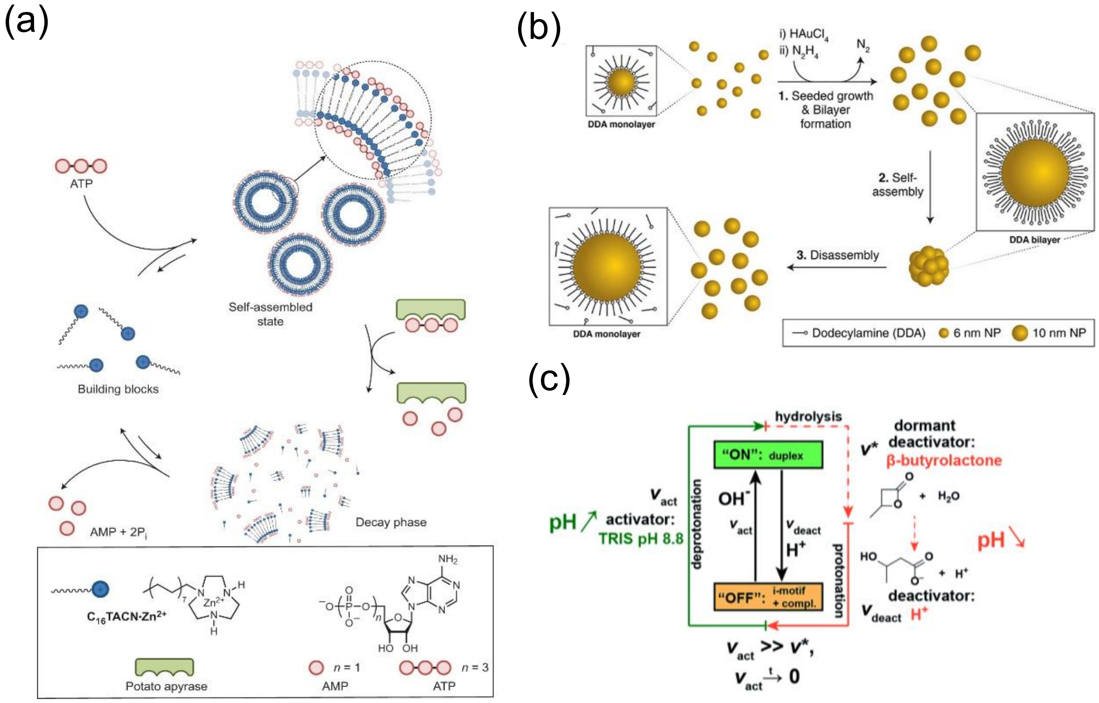

Figure 1.5 Chemically fueled dissipative colloidal assemblies (a) Scheme showing dissipative assembly of micelles composed the building block 1,4,7-triazacyclononane●Zn^{2+} shown as a blue sphere with a black curved tail. Upon addition of adenosine triphosphase (ATP) depicted as the 3 red circles, the micelles will be formed; however, potato apyrase (denoted as the green object) will hydrolyze ATP to adensine diphosphate (ADP) depicted as the 2 red circles. ADP cannot stabilize the micelles and thus the assembly begins to decay. Figure adapted from [81]. (b) Schematic of proposed mechanism of chemically fueled dissipative assembly of Au nanoparticles. Addition of hydrazine reduces Au(III) sals and induces self-assembly due to changes in local concentration of dodecylamine (DDA) ligand which upon equilibration result in disassembly of higher order aggregates. Figure adapted from [108]. (c) Schematic of transient DNA duplex formation using pH triggered DNA switch (i-motif). The system starts in the "off" state with single stranded DNA, Au nanoparticles and butyrolactone. Addition of TRIS buffer increases pH, triggers duplex formation and nanoparticle assembly referred to as the "on" state. Over time hydrolysis of butyrolactone, causes pH to increase and nanoparticles to disassemble, returning to the system to the "off" state. Figure adapted from [82].

accomplished *via* addition of hydrazine, as a reducing agent to an Au(III) salt and Au(0) colloidal solution.[108] The reduction of the free Au(III) results in attachment of Au(0) clusters to existing nanoparticle which increases the local surfactant concentration on the surface of the nanoparticle (Figure 1.5b).[108] The increased local concentration leads to transient aggregation of nanoparticles, which over time is dispersed upon equilibration of the surfactant concentration.[108] Clock reactions can also be used to achieve nonequilibrium colloidal behavior by coupling the oscillatory changes in chemical concentration over time with a stimuli-responsive colloidal system. In one example the methylene glycol/sulfite/gluconolactone (MGSG) oscillator is coupled with pH responsive nanoparticles.[103] The MGSG oscillating reaction results in pH fluctuations from pH 7 to 9, leading to changes in the protonation state of 2-fluoro *para*-mercaptophenol.[103] In the protonated form the phenolate stabilizes the individual nanoparticles in solution and in the protonated phenol form the nanoparticles assemble into aggregates.[103] This approach yields oscillatory assembly and disassembly in response to the oscillatory pH change of the clock reaction.[103]

Biomacromolecules, such as oligonucleotides have also been used as chemical fuels for achieving transient colloidal assembly. To achieve this, a pH-triggered DNA switch was used to enable transient DNA duplex formation (Figure 1.5c). Upon addition of TRIS buffer into the solution of butyrolactone and DNA-functionalized gold nanoparticles, the pH of the solution increases rapidly.[82] The increase in pH is short lived due to the hydrolysis of the butyrolactone, which causes pH reduction.[82] The transient change in pH induce transient aggregation of the DNA functionalized nanoparticles.[82]

1.8.2 Light driven dissipative colloidal assembly

Light can also be a source of fuel for nonequilibrium colloidal behavior. As compared to chemical fuels the use of light has the advantage of offering the potential to control nonequilibrium behavior in a spatiotemporal fashion. As discussed in section 1.6, azobenzene can be incorporated to yield interesting nonequilibrium behavior. The UV triggered *trans* to *cis* isomerization can also be used to induce transient nanoparticle aggregation using nanoparticles functionalized with azobenzene derivatives (Figure 1.6a&b).[105] Others have shown the use of spiropyran derivatives as photoacids to trigger the transient aggregation of carboxylate functionalized particles (Figure 1.6d).[64] Upon UV irradiation the carboxylate is protonated to the neutral carboxylic acid form causing aggregation of particles (Figure 1.6c). This process is transient due the spontaneous reversible reaction of spiropyran which increases the pH of the solution and reforms the negatively charged carboxylate, resulting in disassembly.[64] The examples discussed in this section and section 1.8.1 are mostly extension of approaches employed in molecular dissipative assembly systems discussed in section 1.7 to the dissipative assembly of colloidal systems. In the next section (1.8.3), nonequilibrium colloidal systems that capitalize on properties unique to the colloidal scale will be discussed.

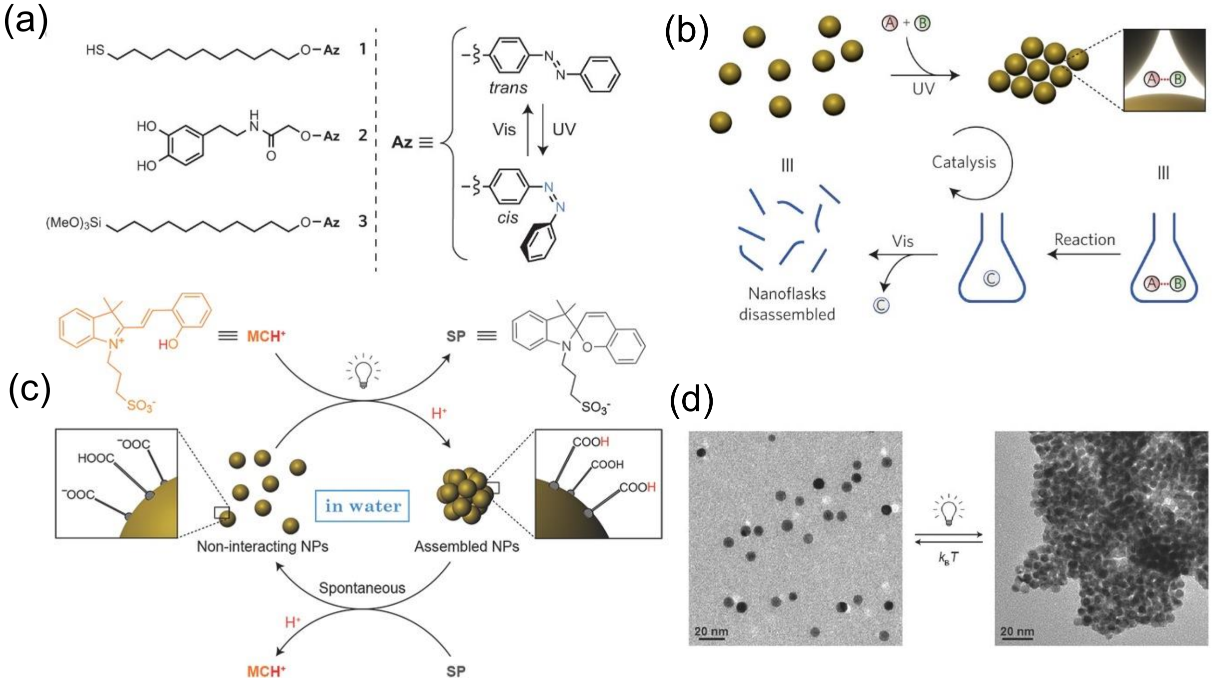

Figure 1.6 Light fueled dissipative colloidal assemblies (a) Scheme showing the azobenezene derivatives that are used to functionalize nanoparticles to allow for the light driven assembly of nanoflasks *via* the UV triggered *trans* to *cis* isomerization shown on the right. Figure adapted from [105]. (b) Schematic showing the light driven aggregation of the nanoparticles that yield nanoflasks that can trap polar molecules, denoted as A+B. The nanoflasks serve as nanocontainers which accelerate chemical reactions denoted as the conversion of A+B to C. The nanoflasks can be disassembled *via* visible light irradiation. Figure adapted from [105]. (c) Scheme showing dissipative assembly of carboxylate functionalized nanoparticles using an UV triggered photoacid *via* the closing of merocyanine (MCH^+) to spiropyran (SP). UV irradiation results in a proton release that facilitates the protonation of carboxylates to carboxylic acids, which leads to the assembly of nanoparticle aggregates. Spontaneous opening of SP back to the MCH^+ form results in the dispersion of the aggregates due to the repulsive forces of the negatively charged carboxylates. (d) The transient nanoparticle aggregation driven by the photoacid is shown in transmission electron micrographs of the particles before UV irradiation (shown in the leftmost image) and after UV irradiation (shown in the rightmost image). Figure adapted from [64].

1.8.3 Light & chemically driven active colloidal motion

Active matter—the collective mobility of self-propelled objects—has emerged as a subfield of nonequilibrium materials.[110] Active matter is characteristic of self-propelled objects that convert various forms of energy into mechanical work, which is commonly seen in colloidal motion through a fluid.[110] To start this section a few fundamental definitions and processes will first be described. Active motion of colloids is often fueled via phoretic forces between particles and the local field gradient such as chemical, hydrodynamic, electrostatic or magnetic properties.[86] In the case where motion is generated by a local gradient of a chemical species, this is referred to as diffusiophoresis.[111] Electrophoresis refers to electric field gradients which uses the interaction between an electric field and the electrical double layer of a particle. The local field gradient can be generated by the active colloid itself, in which case it is termed self-phoresies.

Active colloids can be achieved using a combination of light and chemical fuels with hydrogen peroxide as the most commonly used chemical fuel. Particles such as Pt, Pd, TiO_2, Fe_2O_3, and AgCl can catalyze the decomposition of hydrogen peroxide into water and oxygen.[110] For TiO_2, Fe_2O_3, and AgCl particles, the reaction can be further controlled by light.[110] Let us take one simple example to demonstrate how nanoparticle catalysis can generate motion. A cube of Fe_2O_3 is immobilized in a solution of hydrogen peroxide containing tracer (unreactive) microparticles.[62] Upon irradiation with light, hydrogen peroxide decomposition occurs at the surface of the cube and the tracer microparticles propel towards the region of depleted hydrogen peroxide *via* diffusiophoresis, generating active colloidal motion.[62] In another example, AgCl microparticles were used to achieve active motion by using the local release of ions around the microparticles in response to UV irradiation (Figure 1.7a).[112] When mixed with tracer microparticles, the tracer particles get caught in the local ion gradient around the AgCl microparticles, and clusters or "schools" of particles emerge.[112] The catalytic properties of AgCl microparticles enables the decomposition of hydrogen peroxide in the presence of UV light and achieves oscillations of colloidal assembly from clustered to dispersed microparticles.[88] This type of approach can be leveraged to construct more complex systems such as logic gates.[113]

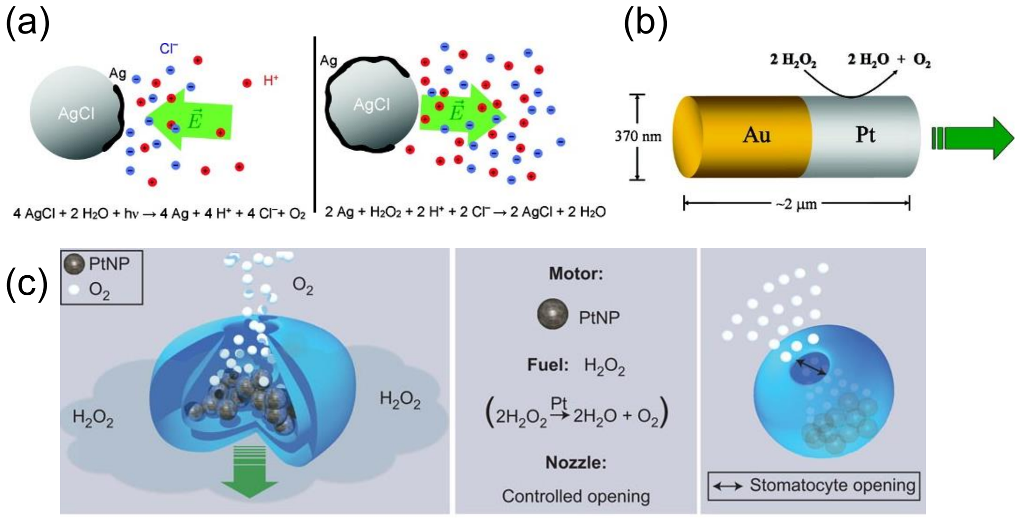

Figure 1.7 Schematics of chemical and light driven colloidal motion using nanoparticle catalysis. (a) Schematic of colloidal motion of AgCl particles driven by the catalysis of hydrogen peroxide in the presence of UV light and AgCl nanoparticles (NP). Chlorine ions are depicted as blue (-) circles, and the protons are depicted as red (+) circles. Leftmost schematic shows the change in the local ionic strength around the surface of the NPs due to the AgCl releasing ions result in a net electric field towards the surface of the NPs as shown by the green arrow. The balanced chemical reaction is shown underneath. The right most schematic shows decomposition of hydrogen peroxide via the released ions which results in a net electric field away from the NPs as shown by the green arrow. The full balanced chemical reaction is shown below. Figure adapted from [88]. (b) Schematic of asymmetric nanorods composed of inert Au and catalytic Pt surfaces. Figure adapted from [87]. (c) Schematic of autonomous colloidal motion using artificial stomatocytes (depicted in blue bowl-shaped particle. The particles are loaded with catalytic Pt NP shown as grey circles, which catalyze the decomposition of hydrogen peroxide into O_2 shown as white circles. The chemical reaction that occurs is shown in the middle panel. As the chemical reaction proceeds the O_2 exists the stomatocytes via the opening resulting in active colloidal motion. Figure adapted from [107].

1.8.4 Chemically driven active colloidal motion

Asymmetric colloids have also been used to generate active nonequilibrium motion fueled by chemical reactions such as hydrogen peroxide decomposition.[114] In one example, asymmetric nanorods composed of Pt and Au were shown to generate autonomous colloidal motion.[87] The Pt portion of the nanorod catalyzes the decomposition of hydrogen peroxide leading to a change in the interfacial energy between the solvent and the nanorod, giving rise to rotation due to the asymmetric nature of the nanorod (Figure 1.7b).[87] Janus particles—particles composed of two nonidentical faces—can be used in lieu of nanorods to impart anisotropy and yield active colloidal motion. Like the nanorod system, one face of the Janus particle is composed Pt which catalyzes hydrogen peroxide decomposition, while the other face is composed of inert Au. In response to an input of chemical energy in the form of hydrogen peroxide the colloidal solution exhibits active motion, as observed via the aggregation of particles.[115] Active motion is also demonstrated in another type of asymmetric colloid system known as stomatocytes, which are bowl-shaped polymer vesicles with a narrow opening (Figure 1.7c).[107] To achieve active motion, the stomatocytes are loaded with Pt nanoparticles such that upon addition of hydrogen peroxide, chemically-fueled active motion is achieved due to the generation of oxygen bubbles that escape *via* the narrow opening of the bowl.[107] Through decorating the surface of the of stomatocyte with a temperature responsive polymer, the accessibility of hydrogen peroxide to the Pt nanoparticles can be self-regulated.[116] This work advanced the field by demonstrating the use of a thermally responsive valve to reversibly control the active motion.[116]

1.8.5 Magnetically driven active colloidal motion

Magnetic fields have also been employed as the fuel for driving active colloidal motion. The use of magnetic fields allows for a non-contact method of supplying energy. In an early example, magnetic microparticles were fueled by an oscillating magnetic field to achieve active motion.[106] The magnetic microparticles were linked together in a linear chain and attached to a red blood cell.[106] In the presence of an oscillating magnetic field, the microscale object demonstrates a beating pattern that results in propulsion due to the linear chain of magnetic microparticles.[106] This work demonstrates the first example of the controlled swimming of artificial micrometer structures, mimicking the motion of bacterial flagella.[106] Ferrofluids composed of magnetic nanoparticles have also be shown to exhibit nonequilibrium colloidal motion that result in dynamic assembly.[117] A droplet of a ferrofluid is placed on a superhydrophobic surface and an external magnetic field is applied, which results in the assembly of the single droplet into multiple droplets.[117] The system (at equilibrium) is then pushed away from equilibrium by using changes in the magnetic field that results in kinetically trapped states and dissipative assemblies.[117]

1.9 Dissipative Macroscopic Behavior

Next, nonequilibrium behavior that manifests on the macroscopic scale will be discussed. Biological systems demonstrate nonequilibrium behavior at all length scales from regulating the concentration of chemical species to regulating cycles such as the circadian sleep cycle.[12] Mimicking nonequilibrium behavior across all length scales is highly sought after but remains a challenge in the field. Many of the driving forces that power existing nonequilibrium systems operate on the molecular scale and are easily overpowered by Brownian motion, making it challenging to achieve macroscopic nonequilibrium behavior. In this section processes driven by chemicals,[18] light, [118] and heat[61] to yield macroscopic nonequilibrium behavior will be discussed.

1.9.1 Chemically fueled macroscopic dissipative behavior

Chemical fuels can be used to achieve macroscopic dissipative behavior by coupling a change in concentration of a chemical species to a stimuli-responsive polymer. The Belousov-Zhabotinsky (BZ) reaction in particular has received significant attention in the nonequilibrium field due to the pioneering work by Yoshida *et al.* that demonstrated oscillatory changes in swelling of a hydrogel.[18] In specific, a pH responsive gel was coupled to oscillatory changes in pH associated with the BZ reaction to yield a self-oscillating system.[18] The polymer used in the initial demonstration of this system was composed of N-isopropylacrylamide (NIPAAm) and acrylic acid, which exhibits a pH dependent lower critical solution temperature (LCST) phase transition in which the gel deswells at temperatures about the LCST.[18] This polymer was coupled to the oscillatory changes on pH in a continuous-flow stirred tank reaction in order to yield autonomous oscillations.[18] In another example, Horváth *et al.* demonstrated chemo-mechanical oscillations of a pH responsive gel swelling and shrinkage in the presence of the proton-autoactivated bromate-sulphite (BS) reaction.[119] Depending on the experimental parameters, the BS reaction can exhibit clock reaction type behavior and yield oscillatory changes in pH.[119] In this work, the oscillations do not occur as a result oscillatory changes in the pH due to the BS reaction, but rather because of mechanical feedback from deswelling of the hydrogel that results in two distinct pH regimes in the conically-shaped hydrogel. Horváth *et al*. has further extended this work by using a different reaction network: methylene glycol–sulphite OH-producing clock reaction.[119] Furthermore, Korevaar *et al.* used a polyacrylic acid hydrogel crosslinked with Cu(II) salts to achieve nonequilibrium behavior. The nonequilibrium behavior is chemically driven upon addition of acid to fuel the deswelling.[120] The addition of acid results in protonation of the carboxylates and decomplexation of Cu(II).[120] The nonequilibrium behavior arises from the competition of the flux of water into the gel (due to the Cu(II) release) and mechanical relaxation of the gel (Figure 1.8). This manifests in a wave of osmosis driven expansion/contraction of a macroscopic hydrogel.[120] In another exciting demonstration, a pH responsive hydrogel photonic crystal that exhibits a transient change in the optical properties due to pH dependent activity of the enzyme urease was developed.[121] Urease catalyzes the conversion of urea to carbon dioxide, ammonia, and hydroxide.

The generation of hydroxide species results in an increase of the pH of the solution, providing a negative feedback and stopping the urease activity. To achieve nonequilibrium behavior the photonic gel system starts in basic conditions (pH > 7) so that the enzyme is dormant. Upon addition of an acid, the pH of the solution abruptly drops and the enzyme is activated.[121] As urea is converted into ammonia and hydroxide, the pH of the solution begins to increase which eventually shuts off the enzymatic activity. This demonstrates the use of urea as the chemical fuel to sustain nonequilibrium behavior on the macroscopic scale.[121] The abovementioned examples

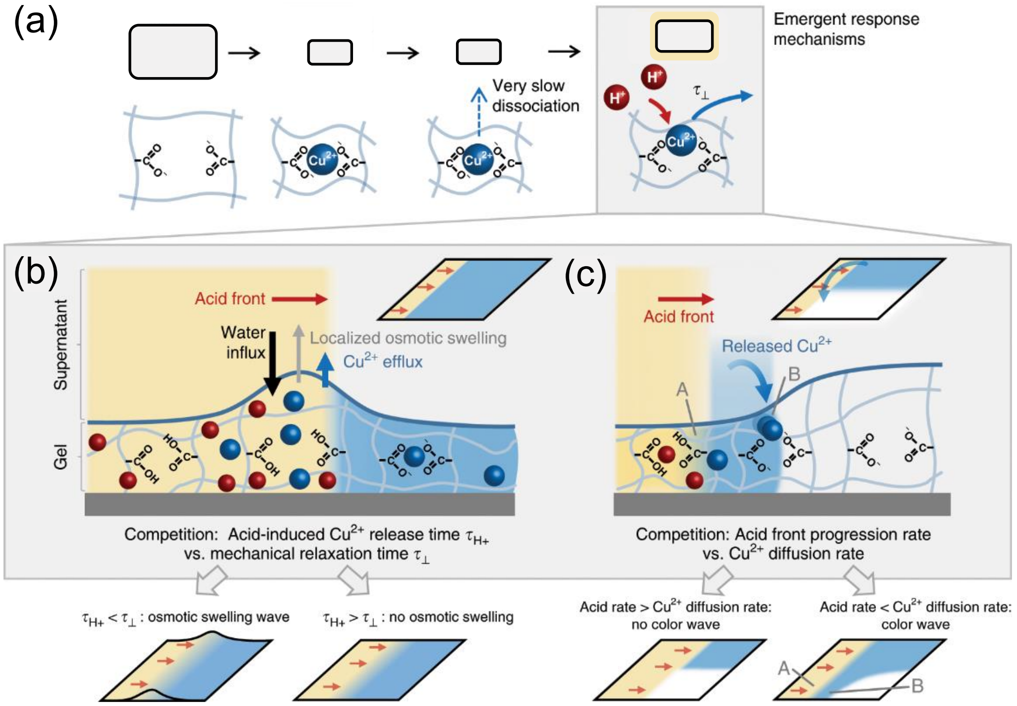

Figure 1.8 Schematic of osmosis driven expansion/contraction of a macroscopic chemically fueled hydrogel. Schematic of polyacrylic acid (PAA) hydrogel that deswells in response to acidic conditions or in the presence of Cu(II) depicted in yellow and blue, respectively to achieve nonequilibrium behavior. (a) Upon addition of Cu(II) the gel deswells to achieve a kinetically stable (after removal of excess salts) complex with two carboxylates. Addition of an acid triggers uncomplexation a rate related to the delivery rate of the acid ($\tau H+$). The release of the Cu(II) salts induce water influx and mechanical relation of the gel ($\tau\perp$). The relative rates impacted the observed swelling behavior as depicted in b & c (b) Schematic showing result when $\tau H+ < \tau\perp$ waves of swelling proportion of to $\tau H+$ are observed. (c) Schematic of the competition of diffusion of Cu(II) and transient recomplexation to carboxylates. Figure adapted from [120].

demonstrate chemically driven nonequilibrium behavior on the macroscopic scale using the deswelling and reswelling of hydrogel materials.

1.9.2 Heat and light fueled macroscopic dissipative behavior

Macroscopic nonequilibrium behavior has also been demonstrated using heat and light to achieve autonomous oscillatory actuation of solid polymers. In one notable example, a shape-memory polymer was used to impart temperature responsive properties which was coupled to a feedback loop to achieve oscillatory motion.[61] This was achieved by placing the polymer on a hot surface—upon contact a temperature gradient through the thickness of the material forms, resulting in bending of the material so that the center was lifted up and away from the heated surface. The actuation resulted in cooling, which allowed for the initial shape to be recovered, putting the material into proximity of the hot surface once again to complete one cycle of nonequilibrium behavior. This could be repeated multiple cycles with a constant source of heat as the fuel.[61] An alternative approach relies on the dual temperature and light responsive nature of liquid crystalline materials composed of azobenzene derivatives.[118] Similar autonomous oscillations in motion are observed for the liquid crystalline material with an increased level of control of various motions including rolling and oscillatory rocking back and forth motion.[118] This example demonstrated an additional layer of control by using two different fuel source to achieve more complex macroscopic motion.

1.10 Emergent behavior of synthetic nonequilibrium systems

Nonequilibrium systems exhibit unique dissipative behavior, which has the potential to be harnessed for a variety of applications. While current studies of nonequilibrium systems are primarily focused on fundamental interest, the applications become more apparent as the methods for designing and constructing various nonequilibrium systems evolve to mimic more closely those seen in biological systems. In this section, we will discuss the emergent dissipative behavior such as self-healing, self-assembly, self-organizing, and self-regulating behavior that can be employed for the development of functional systems.

Dissipative supramolecular assemblies that exhibit transient gelation have given rise to interesting properties such as self-healing. Compared to analogous equilibrium supramolecular assemblies which often have a sol to gel transition, nonequilibrium supramolecular assemblies exhibit a sol to gel to sol transition.[122] This transient gelation gives rise to emergent properties not seen in analogous equilibrium supramolecular assemblies, such as the ability to self-heal. The ability to self-heal arises from the dynamic nature of the assembly. The self-healing behavior is demonstrated in one example that uses chemically driven dynamic assembly using competing alkylation and hydrolysis reactions to recover the original mechanical properties of a gel after destructive shearing of a gel though application of a high strain force.[78] It should be noted that this approach to self-healing requires a constant influx of the chemical fuels to sustain the self-healing capability.[13] The transient self-assembly can also be used for applications as a self-erasing ink.[27]

Additionally, nonequilibrium assemblies can exhibit self-organization on larger length scales than the monomer units themselves. Self-organization exists in biological system such as in the spontaneous self-organization of cell due to a phenomenon known as Bérnard convection, or the self-organization of larvae into clusters.[123] While self-organization has not been demonstrated in dissipative supramolecular assembly,[122] there has been progress towards self-organization within the field of active materials. More primitive examples of self-organization can be seen in the transient aggregation,[108] and schooling behavior of nonequilibrium colloidal systems.[112]

Self-regulation has also emerged as a useful feature of nonequilibrium systems. A notable example relies on chemo-mechanical feedback loop to achieve self-regulation of temperature.[125] This system uses an array of microscale pillars embedded in a temperature responsive hydrogel (Figure 1.9). The tops of the pillars are functionalized with a catalyst for an exothermic reaction.[125]

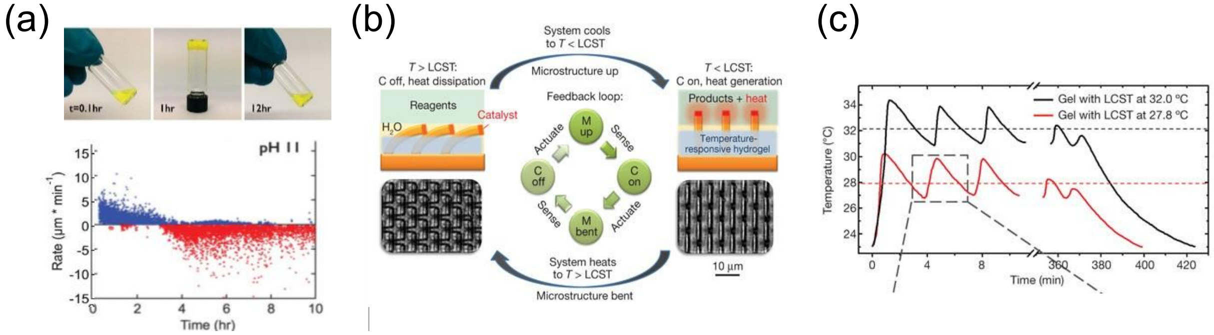

Figure 1.9 Nonequilibrium behavior in the form of dissipative assembly and self-regulation. (a) Top 3 images show the sol-gel-sol behavior over time that is characteristic of transient supramolecular assemblies. Figure adapted from [78]. (b) Schematic of temperature-regulating device. The pillar (vertical orange bars) are embedded in a lower critical solution temperature (LCST) hydrogel (blue). The system starts at temperatures (T) below LCST with the pillars in the upright position such that the catalytic tips are immersed in the fuel rich organic layer (green). As the reaction proceeds, heat is generation due to the exothermicity, which is sensed by the hydrogel and results in deswelling and bending of pillar out of the fuel rich organic layer. As the system cools the pillars sense and actuate in response. This chemo-mechanical cycle allows for temperature regulation. Figure adapted from [124]. (c) Temperature of self-regulating device over time showing the oscillating change in temperature that allows for regulation of the exothermic reaction. Depending on the LCST the range of temperatures achieved can be controlled. Figure adapted from [124].

Upon addition of organic starting materials, which serve as the chemical fuels, the exothermic reaction proceeds due to the presence of the catalytic pillars in the organic, fuel-rich phase.[125] Once the temperature reaches a certain threshold, the temperature responsive hydrogel shrinks in response and causes the pillars to bend down so that the catalytic pillars are solely in the aqueous phase. This temporarily turns off the catalytic reaction due to inaccessibility to chemical fuels, allows for heat dissipation, which in turn actuates the pillar back into the organic, fuel-rich phase, completing one cycle of nonequilibrium behavior. By coupling the exothermic reaction with a temperature responsive polymer, a device able to autonomously self-regulate temperature was demonstrated. Others have reported a nonequilibrium system capable of adaptive reconfiguration *via* a photothermal feedback loop that demonstrated the ability to detect and track light.[126]

1.11 Challenges of synthetic nonequilibrium systems

The field of nonequilibrium materials systems has several critical challenges that limit the development of applications and true biomimicry. Biological systems use chemical signals to fuel nonequilibrium behavior on multiple length scales.[12] For example, on the molecular scale biological systems have the ability to regulate the concentration of chemical species from ionic strength to concentration of key metabolites.[12] On the microscale, biological systems use ATP hydrolysis to power cell motility via dissipative assembly. Macroscopically, muscles use chemical fuel to create work in the form of macroscopic motion.[127] Additionally, macroscopic examples in nature include Turing patters as seen in zebrafish stripes which originate from complex, autonomous nonequilibrium processes that have been attributed to molecular and cellular scale mechanisms.[128,129] This level of hierarchical demonstration of nonequilibrium behavior in synthetic systems remains a challenge. Another challenge to the field is the development of biocompatible systems. Most the reported synthetic systems use reagents that are incompatible with biologically systems. Efforts have been made to develop milder reagents and conditions.[101,130] Even with these milder systems, there is still a gap between the synthetic and physiological conditions for interfacing synthetic nonequilibrium systems in the complex biochemical environments. Another intrinsic challenge for nonequilibrium materials to overcome is the requirement of a fuel source. Thus, for applications in the real world an infrastructure of fuel supply would be necessary to sustain the nonequilibrium behavior.[13] Lastly, the complexity of synthetic nonequilibrium systems pales in comparison to biological counterparts. While DNA-based systems have demonstrated improved levels of complexity, they are limited in terms of scalability due to cost.[131] There is room for growth in nonequilibrium systems that exhibit behavior such as self-replicating and even learning systems. Primitive examples of learning have been demonstrated using logic gates and memory devices.[132] Nevertheless, Nonequilibrium materials remains a nascent field with far reaching potential to create synthetic materials with unprecedented abilities. The ability to create nonequilibrium will allow scientists to make truly like-like materials.

1.12 Goals of thesis

In the sections above we have briefly reviewed bioinspired work that developed and expanded our collective understanding of nonequilibrium system. The bioinspired research of nonequilibrium systems has led to the demonstration of emergent behavior, as outlined in Section 1.10, that has the potential to have far-reaching applications. In this thesis we address several challenges in the field. The first challenge we aim to address is the translation of chemically fueled nonequilibrium behavior into macroscopic 3-dimensional motion. This has remained a challenge in the field because molecular scale driving forces are easily overpowered by Brownian motion. In Chapter 2 we show that, by coupling a highly exothermic reaction with a temperature responsive polymer, 3-dimensional macroscopic motion can be achieved. The second challenge we aim to address is the development of synthesis self-regulating devices in 3-dimensions. In Chapter 3 we describe our efforts toward a 3-dimensional self-regulating system using a temperature responsive polymer to modulate the catalytic activity of an exothermic reaction. Finally, in Chapter 4, we address a challenge in the field of self-healing magnetic nanocomposites. we report on efforts to address the challenge of nanoparticle aggregation and ease of translation of materials in the field of magnetic self-healing materials. We report the synthesis and characterization of a magnetic self-healing material synthesized *via* a graft-from approach using commodity monomers.

Chapter 2: Chemothermally Driven Out-of-equilibrium Materials

2.1 Introduction chemically fueled nonequilibrium materials

Biological systems have evolved efficient mechanisms for manipulating self-assembly, transport and macroscopic properties by operating far from equilibrium.[12] Natural out-of-equilibrium systems consume and dissipate energy to the environment to power important life processes.[133] A preeminent example in biology is microtubules, which are composed of monomeric tubulin units that can transiently assemble and disassemble to perform many vital functions including cell division.[134] Chemists have been interested in studying out-of-equilibrium systems since the 1950's;[135] however, experimental demonstrations of synthetic out-of-equilibrium systems, especially at macroscopic scale, remain challenging.[13]

Recently, there is a growing interest in developing synthetic out-of-equilibrium systems to mimic biology.[32,46] Synthetic out-of-equilibrium materials have been reported that employ light,[136,137,126,138] current,[139] or heat to fuel characteristic dissipative behavior.[61] Biological out-of-equilibrium systems ubiquitously use chemical fuels, such as ATP and GTP, to sustain the dissipative processes.[12] To closely mimic biology, it is desirable to use chemical fuels in synthetic out-of-equilibrium systems. Additionally, chemical fuels are commonly used in general applications such as combustion engines,[140] and fuel cells due to the low-cost, convenience and high-power density.[141] Several elegant approaches have been reported for chemically driven out-of-equilibrium systems using various chemical fuels such as alkylating agents,[78] carbodiimides,[79,97] thioesters,[15] ATP,[81,130,142] urea,[143] redox agents,[16,101] and nucleic acids.[19,20]. To date, chemically fueled out-of-equilibrium systems have manifested the characteristic dissipative behavior in the form of transient self-assembly,[78,81,97,101] self-propelling nanomotors,[107] molecular machines,[73] and self-regulation.[143] Nevertheless, these behaviors only manifest on the molecular to the colloidal scale. A significant advancement was the use of an exothermic reaction to achieve a device capable of self-regulating temperature *via* oscillatory motion of a microarray of pillars.[124] It remains a major challenge to create chemically driven manmade out-of-equilibrium systems that operate in 3-dimensions on the *macroscopic* scale.

Harnessing the characteristic dissipative behavior of out-of-equilibrium materials on a macroscopic scale to produce 3-dimensional motion will advance the field by more closely mimicking biological systems, which operate at macroscopic organism level by dissipating energy at the molecular scale.[144] Light powered processes have made advances in achieving autonomous macroscopic motion by utilizing liquid crystalline materials.[145,146] Chemically fueled motion is desirable because it more closely mimics biological systems. However, pushing chemically driven out-of-equilibrium systems into the macroscopic scale is a challenge because driving forces on the molecular scale are easily overpowered by Brownian motion.[147,148] While a few examples showed enzyme switches to achieve chemically driven out-of-equilibrium behavior on visible scale, these systems did not yield any macroscopic motion.[121,149] The only chemically driven out-of-equilibrium systems that generated macroscopic motion rely on the Belousov-Zhabotinsky (BZ) oscillating reaction, limiting the scope for general applications.[100,150] Notably, He *et al.* reported a self-regulating 2-D surface that elegantly combines a bi-phasic microfluidic device with an exothermic reaction;[124] nevertheless, 3-dimensional macroscopic actuation was not possible for this system.

2.2 Our design of self-regulating materials

Herein we describe chemothermally driven out-of-equilibrium materials that can perform macroscopic actuation and do work by lifting objects. Specifically, we achieve this by driving a lower critical solution temperature (LCST) phase transition of poly(N-isopropylacrylamide) (pNIPAAm) hydrogels with heat generated by a copper-catalyzed azide-alkyne cycloaddition (CuAAc) reaction (Figure 2.1a). pNIPAAm was chosen for this study due to its well-studied reversible LCST phase transition.[151] CuAAc reaction was used because of the large heat formation of the reaction, with a reaction enthalpy of nearly 50 kcal/mol.[152] In our proposed approach for realizing macroscopic motion using out-of-equilibrium processes, the fuels are the azide and alkyne, and the system is the pNIPAAm gel with the copper catalyst in presence. Upon addition of the fuels (azide and alkyne), the system moves out of equilibrium due to the energetically downhill CuAAc reaction, raising the temperature of the system and inducing an LCST transition

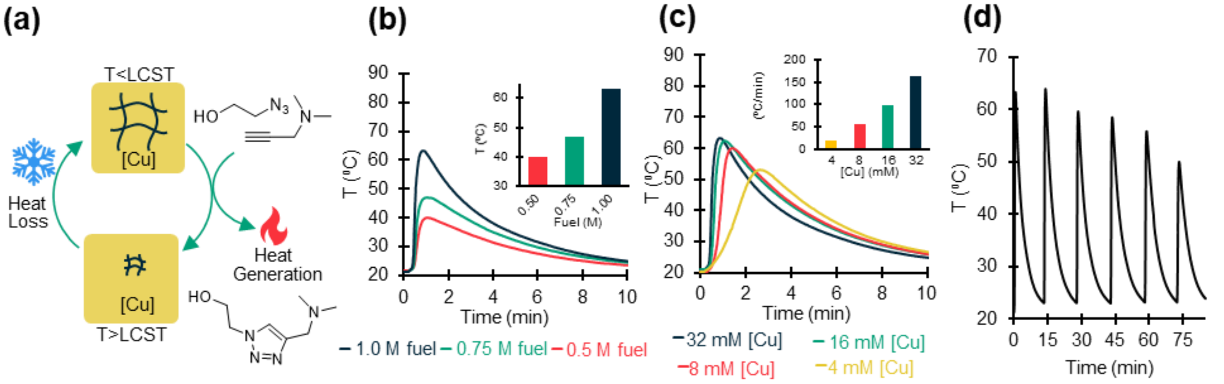

Figure 2.1 Design concept of chemothermally driven out-of-equilibrium materials and small molecule heat generation studies. (a) Scheme showing the out-of-equilibrium system composed of a temperature responsive hydrogel with a lower critical solution temperature (LCST) phase transition along with a catalyst, Cu(I)-tris(3-hydroxypropyltriazolylmethyl)amine (THPTA), to catalyze the azide-alkyne cycloaddition (CuAAc) of 2-azidoethanol and 3-dimethylaminopropyne, which are the fuels. The heat from the exothermic CuAAc drives the LCST phase transition. Heat dissipation then completes the cycle by lowering the temperature of the system. (b) Temperature increase at different concentration of fuels: 0.5 M (red), 0.75 M (green), and 1.0 M (blue). The inset shows the maximum temperature of each condition. All experiments were carried out at 1 mL scale with 32 mM Cu-THPTA. (c) Temperature increase at different concentration of Cu-THPTA: 4 mM (yellow), 8 mM (red), 16 mM (green), and 32 mM (blue). The inset shows the slope of the heat increase. All experiments were carried out at 1 mL scale with 1 M fuels. (d) Repetitive heat generation and dissipation for 6 cycles by adding new batches of fuels (1 mmole of each fuel added every 15 minutes). The experiment was carried out at 1 mL scale with 32 mM Cu-THPTA.

to the pNIPAAm gel. As the fuels run out, the heat generated by the CuAAc reaction dissipates to the environment, driving the re-swelling of the gel, completing an out-of-equilibrium cycle (Figure 2.1a). The same process can be repeated multiple cycles by repetitively adding new chemical fuels.

2.3 Results and discussion

2.3.1 Exothermicity

We started by evaluating the heat generation from the CuAAc reaction. To accelerate the CuAAc reaction for sufficient heat generation, tris(3-hydroxypropyltriazolylmethyl) amine (THPTA) ligand was added to complex with the Cu(I) catalyst. Previous reports have shown that Cu-THPTA catalyst is much more active for CuAAc reactions compared to uncomplexed copper catalyst.[153] To ensure water solubility, hydrophilic 2-azidoethanol and 3-dimethylaminopropyne were chosen as the fuels. 3-Dimethylaminopropyne was used also for its high reactivity in CuAAc reaction.[154] For model study, addition of the chosen fuels into an aqueous solution containing the Cu-THPTA catalyst indeed resulted in a significant temperature increase (Figure 2.1b-d). The amount of heat generated, and the rate of heat formation could be tuned by the concentrations of the fuels and Cu-THPTA catalyst, respectively. Keeping the Cu-THPTA catalyst concentration constant (32 mM), the maximum temperature of the reaction solution ranged from 40 to 60 ^{o}C by varying the concentration of fuel from 0.50 to 1.0 M (Figure 2.1b). The rate of heat generation could be tuned *via* the concentration of catalyst while keeping the concentration of fuel constant at 1.0 M (Figure 2.1c). The maximum temperature increased with increasing concentration of catalyst, which was expected due to the higher reaction turnover. Additionally, the rate of heat generation increased with higher catalyst concentrations, as evident in the initial slope of the curve (inset in Figure 2.1c). The conditions of 32 mM catalyst and 1 M fuel yield the highest maximum temperature at the fastest rate, so these conditions were used throughout the rest of the study. To demonstrate multiple cycles of heat generation and dissipation, fresh batches of fuels (1 mmol each for every cycle) were added at 15-minute intervals (Figure 2.1d). Importantly, the temperature increase at each cycle of fuel addition was well above the LCST transition temperature of pNIPAAm (i.e., 32 °C),[155] indicating that this chemothermal process could be used to trigger an LCST transition for the macroscopic pNIPAAm hydrogel. The decrease of maximum temperature for later additions of fresh fuels was due to dilution of the reactants and the catalyst in the system.

2.3.2 Coupling to colloidal pNIPAAm solution

Using the reaction conditions identified above, the initial demonstration of transient out-of-equilibrium behavior was conducted using a colloidal solution of pNIPAAm nanoparticles (NPs). pNIPAAm NPs with a hydrodynamic diameter of 236 nm and polydispersity index of 0.043, as determined by dynamic light scattering (DLS, Figure 2.8&9), were synthesized via free radical precipitation polymerization.[156,157] P-NIPAAm NP solutions exhibit a cloud point associated with the LCST transition which was monitored *via* turbidity measurements at a wavelength of 500 nm, a region with minimal overlap with the absorption of the Cu-THPTA catalyst, the fuels, and the triazole product (Figure 2.12 & 2.13). The system, which was composed of Cu-THTPA (32 mM) and the pNIPAAm NP (2 mg/mL), was pushed out-of-equilibrium by the addition of the chemical fuels (1 mmol each). We observed a temperature increase (Figure S14) and a change in light transmittance, which was attributed to increased light scattering from collapsed pNIPAAm NPs. Following reaction completion and heat dissipation to the environment, the pNIPAAm NPs reswelled and the turbidity decreased. As a control, this behavior was not observed when the system contained all components except the pNIPAAm NPs (Figure 2.13). The transient out-of-equilibrium behavior could be repeated, as shown in the six cycles presented in

Figure 2.2a, where 1 mmol of fuels was added every 15 minutes. The maximum transmittance of each cycle increased with repeated additions of fuels due to dilution of the pNIPAAm NPs with the increase of total solution volume. The transient behavior was also directly visualized by optical imaging (Figure 2.2b), where the solution became turbid shortly after the addition of fuels due to the LCST transition, followed by recovery of transparency as the heat dissipated to the environment.

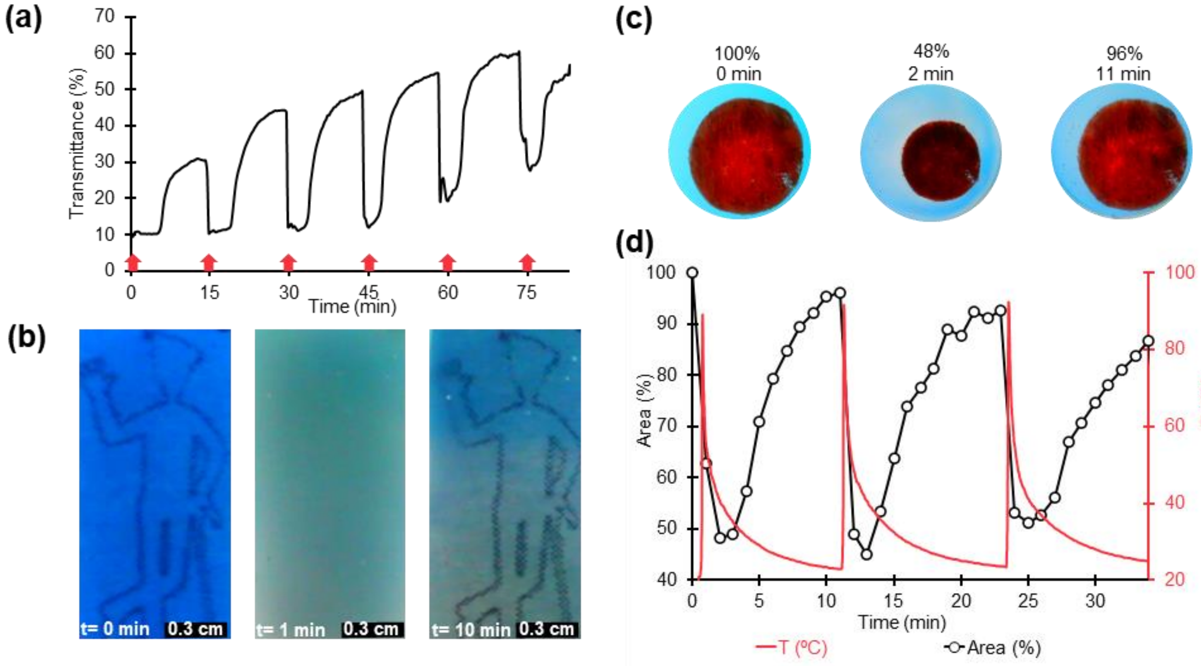

Figure 2.2 Chemothermally driven out-of-equilibrium system demonstrated for a colloidal solution of pNIPAAm NPs and of macroscopic pNIPAAm hydrogels. (a) Transmittance at 500 nm of 1 mL water solution containing 32 mM Cu-THPTA and 2 mg pNIPAAm NP with 1 mmole of fuels (2-azidoethanol and 3-dimethylaminopropyne) added ever 15 min, as indicated with the red arrows. (b) Optical images, with 0.3 cm scale bar, of a colloidal solution of pNIPAAm NPs and Cu-THPTA catalyst before the addition of fuels (T = 0 min), 1 min after the addition of fuels, and 10 minutes after the addition of fuels, showing the transient out-of-equilibrium behavior. (c) A pNIPAAm hydrogel (1.56 cm diameter, stained with Congo Red) was placed in 1 mL of 32 mM Cu-THPTA, and subject to the addition of 1 mmol fuels every 10 minutes. (d) The temperature and percent area of the pNIPAAm hydrogel (relative to 0 min) are plotted over time. Images of the first cycle, along with time point and area (%) are shown.

2.3.3 Coupling to macroscopic pNIPAAm hydrogels

After initial demonstration of chemothermally driven out-of-equilibrium behavior for the NP system, this approach was applied to macroscopic pNIPAAm hydrogels. PNIPAAm hydrogels with fast LCST phase transition response were synthesized and the temperature responsive behavior was carefully characterized (Figure 2.10&11).[158] Circular disks of the hydrogel were dyed with Congo red to aid in visualization and then immersed in an aqueous solution of 32 mM Cu-THPTA catalyst. The temperature and physical appearance were monitored while fuels were added at 10-minute intervals. In response to the addition of the fuels, the temperature increased to 90 ºC, causing a volume phase transition that could be seen in the change of area of the gel from 100% (normalized at 0 min) to 48% in less than 2 minutes (Figure 2.2c). The collapsed hydrogel sample gradually reswelled as the reaction heat dissipated into the environment. Similar to the NP system, the transient behavior could be repeated for multiple cycles. The gel size change synchronized with the solution temperature change caused by each cycle of fuel addition (Figure 2.2d). This demonstrates the ability of the chemothermal approach to drive and LCST transition in macroscopic hydrogels.

Next the chemothermal approach was applied for actuation of an asymmetric bilayer hydrogel. Bilayer hydrogels with one layer that is temperature responsive and the other that is not are known to curve above the LCST due to the asymmetry.[159,160] Here we chose to prepare an asymmetric bilayer hydrogel with one layer composed of pure pNIPAAm and the other a copolymer of with 25 mol% NIPAAm and 75 mol % of acrylamide. Based on a previous study,[161] the second layer hydrogel has much higher LCST temperature that is outside the range of temperatures in our experiment. The same conditions described above were used again and we observed rapid heat generation upon addition of the fuels, causing the asymmetric gel to curve

(Figure 2.3a). As the heat dissipated into the environment, the curved hydrogel sample recovered to the original form. Similarly, the gel curving synchronized with the solution temperature change caused by each cycle of fuel addition (Figure 2.3b). The rapid curving demonstrates the potential application of this approach in fields such as artificial muscles powered by chemical fuels.

Finally, we applied the chemothermal approach to construct a prototype engine that can convert chemical energy into work in the form of reversible lifting of an object. Cylindrical pNIPAAm hydrogels were prepared onto which a copper wire weight was affixed. The gel (5 mg dry polymer) was immersed in an aqueous solution of 32 mM Cu-THPTA, and upon addition of the fuels (1 mmole for each) the gel exhibited a volume phase transition, resulting in shrinkage, lifting the copper ring (83 mg) up by 3.3 mm (Figure 2.3c-d). By increasing the weight of the attached copper ring, we demonstrated that the pNIPAAm hydrogel could lift an object that was over two orders of magnitude heavier than its own dry weight (Figure 2.15). The power output of the engine was calculated to be 0.281 W/kg dry gel, which is comparable to other hydrogel based engines that capitalize on ion gradients,[162] or Belousov-Zhabotinsky (BZ) oscillating reaction.[100]

2.4 Conclusion

Here we demonstrated a chemothermally driven out-of-equilibrium system that could generate macroscopic motion. We achieved this by coupling a highly exothermic CuAAc reaction with a thermo-responsive polymer hydrogel. The transient out-of-equilibrium behavior was demonstrated in cyclic changes of turbidity, volume change, and actuation of asymmetric hydrogels. Furthermore, the macroscopic hydrogel was shown to be able to perform work by consuming chemical fuels, as demonstrated by the reversible lifting of an object two orders of magnitude heavier than itself. This demonstrated bioinspired out-of-equilibrium materials capable of generating macroscopic motion by dissipating chemical energy at the molecular scale. Further studies are currently ongoing in our laboratory toward the design of autonomous, self-regulating macroscopic materials fueled by chemical energy.

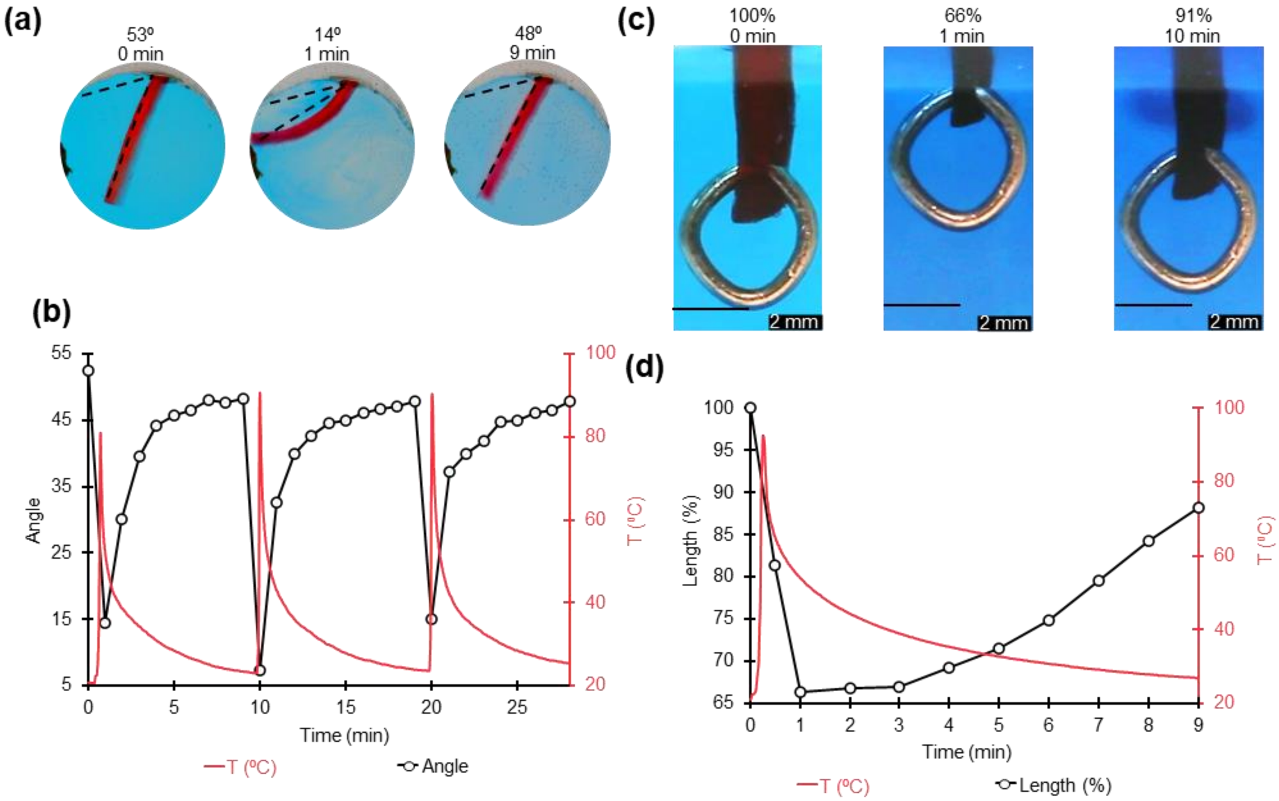

Figure 2.3 Macroscopic chemically driven out-of-equilibirum behavior. (a) A bilayer hydrogel composed of pNIPAAm on the left layer, and 75 mol % feed ratio of acrylamide (relative to NIPAAm) on the right layer was stained with Congo Red and placed in 1 mL of 32 mM Cu-THPTA, and subject to the addition of 1 mmol fuels every 10 minutes. (b) The temperature and angle measured (shown in black dashed lines in images above) are plotted over time. Images of the first cycle, along with time point and angle are shown. (c) pNIPAAm hydrogel with a copper wire weight (83 mg) attached submerged in 32 mM CuTHPTA, 1 mL scale, subject to the addition of 1 mmole fuel at 0 min. (c) Images along with the corresponding time and length (%) are shown, scale bar is 3 mm. Horizontal black line in each image represents the starting point of the copper ring at 0 min. (d) The percent length of the pNIPAAm hydrogel, relative to 0 min, is plotted over time. The temperature of the solution is plotted in red on the vertical axis on the right.

2.5 Experimental

All commercial reagents were used as received and stirred with a magnetic stir bar unless otherwise noted. 3-dimethylaminopropyne, 2-bromoethanol, *N,N'*-methylenebisacrylamide

(MBAAm), tripropargylamine were all purchased from Acros Organics. 3-bromopropanol was purchased from Oakwood Chemicals. $Cu(OAc)_2 \bullet H_2O$ was purchased from Alfa Aesar Chemicals. All other chemicals were purchased from Sigma Aldrich. *N*-isopropylacrylamide (NIPAAm) was recrystallized from hexanes prior to use. Dimethylsulfoxide (DMSO) was dried over activated molecular sieves (3 Å). All yields refer to isolated yields. Nuclear magnetic resonances (NMR) spectra were recorded at 500 MHz CRYO-500 spectrometers at 298 K. ^1H NMR chemical shifts are reported as δ values in ppm relative to residual solvent: $CDCl_3$ (δ=7.26 ppm) or DMSO-*d6* (δ=2.50 ppm). ^1H NMR data are reported as follows: chemical shift (in ppm), multiplicity (s = singlet, d = doublet, t = triplet, q = quartet, br = broad), relative integration in number of protons, and coupling constants in Hz. Multiplets (m) are reported over the range of chemical shift at which they appear. Differential Scanning Calorimetry (DSC) was done on a TA Instruments DSC Q2000 (endotherm down). Samples were loaded into a Tzero aluminum pan and hermetically sealed. Nitrogen was used to purge the furnace at 40 mL/min. The furnace is equilibrated at 30 ºC followed by a temperature ramp at 10 ºC/min to 0 ºC, followed by a 15 min isothermal period, then a temperature ramp of 10 ºC/min to 50 ºC. Transmittance measurements were carried out on a Cary-60 UV/Vis spectrophotometer. Dynamic light scattering (DLS) was done on a Malvern Zetasizer ZS Nano DLS.

2.5.1 Synthesis of small molecules

Scheme 2.1: Synthesis of 2-azidoethanol

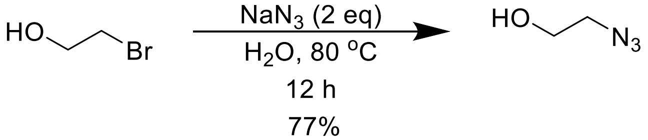

2-azidoethanol was synthesized following the literature reported protocol.[163] It should be noted that lower molecular weight organoazides are explosive and should be handled with caution! Reactions were performed on less than 13 g NaN_3 scale and protected with a blast shield. No explosion was encountered. Sodium azide (5.85 g, 90 mmoles, 2 equiv.) was carefully weighed using a glass pipet into a plastic weight boat and transferred using water (54 mL) into a round bottom flask equipped with a stir bar. 2-Bromoethanol (3.19 mL, 5.62 g, 45 mmole, 1 equiv.) was added and the reaction flask was placed in an oil bath at room temperature equipped with a reflux condenser and a blast shield. The oil bath was heated to 80 °C and held at that temperature overnight. The reaction mixture was cooled to room temperature and transferred to a separatory funnel for extraction with diethyl ether (50 mL, x3). The aqueous layer was handled with caution and quenched by adding 7 mL of 20 wt.% sodium nitrite solution per gram of sodium azide (assuming all sodium azide remains). Next, the aqueous layer was acidified *via* the slow addition of concentrated sulfuric acid until the evolution of brown gas stopped. The combined organic layers were dried over $MgSO_4$ and concentrated under reduced pressure to yield 2-azidoethanol (77% yield). ^1H NMR spectral data agrees with literature reports.[163] ^1H NMR (500 MHz, $CDCl_3$, 298 K) δ 3.85 (dd, 1H, *J* = 10.2, 5.7 Hz), 3.53 – 3.50 (m, 1H), 1.89 (t, 1H, *J* = 5.8 Hz).

Scheme 2.2 Synthesis of 3-azidopropanol

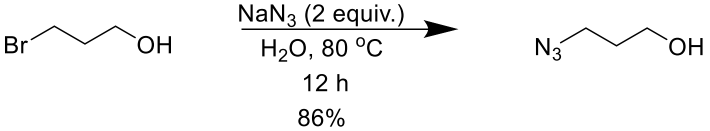

3-azidopropanol was synthesized following the literature reported protocol.[154] It should be noted that lower molecular weight organoazides are explosive and should be handled with caution! Reactions were performed on less than 20 g NaN_3 scale and protected with a blast shield. No explosion was encountered. Sodium azide (18.7 g, 0.228 moles, 2 equiv.) was carefully weighed using a glass pipet into a plastic weight boat and transferred using water (150 mL) into a round bottom flask equipped with a stir bar. 3-bromopropanol (20.0 g, 0.144 mmole, 1 equiv.) was added and the reaction flask was placed in a room temperature oil bath equipped with a reflux condenser and a blast shield. The oil bath was heated to 50 ºC and kept at that temperature overnight. The reaction mixture was cooled and transferred to a separatory funnel for extraction with diethyl ether (150 mL, x3). The aqueous layer was handled with caution and quenched using the same protocol described above. The combined organic layers were dried over $MgSO_4$ and concentrated under reduced pressure. Next, the product was distilled under vacuum to yield 3-azidopropanol (86% yield). ^1H NMR spectral data agrees with literature.[154] ^1H NMR (500 MHz, $CDCl_3$, 298 K) δ 3.76 (dd, 1H, *J* = 11.2, 5.9 Hz), 3.45 (t, 1H, *J* = 6.6 Hz), 1.88 – 1.80 (m, 2H), 1.55 (s, 1H).

Scheme 2.3: Synthesis of tris(3-hydroxypropyltriazolylmethyl)amine (THPTA)

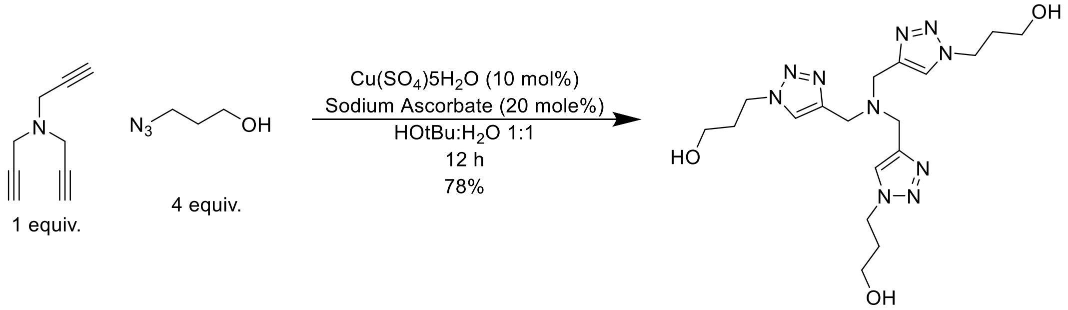

Tris(3-hydroxypropyltriazolylmethyl)amine (THPTA) was synthesized following the literature reported protocol.[154] Tripropargylamine (0.393 g, 3 mmoles, 1 equiv.), and 3-azidopropanol (1.211 g, 12 mmoles, 4 equiv.) were added to a round bottom flask equipped with a stir bar and dissolved with 1:1 tert-butanol:water (6 mL). To this was added $CuSO_4 \bullet 5H_2O$ (74.9 mg, 0.3 mmoles, 0.1 equiv.), and *L*-sodium ascorbate (119 mg, 0.6 mmoles, 0.2 equiv.). The reaction flask warmed slightly due to heat generation. The reaction was stirred at room temperature overnight. Saturated disodium ethylenediaminetetraacetate dihydrate (20.0 mL) was added to the reaction mixture then transferred to a separatory funnel and washed with dichloromethane (15 mL, x3). The aqueous layer was concentrated under reduced pressure to yield a bluish-green solid. The solid was dissolved with minimal amount 80:20 dichloromethane:methanol (~8 mL) and loaded on a plug of neutral alumina. The product was eluted with 80:20 dichloromethane:methanol (~200 mL). The product was concentrated under reduced pressure to yield a yellow oil. The oil was diluted with 80:20 dichloromethane:methanol (4 mL) and precipitated into diethyl ether (250 mL). The resulting cloudy solution was refrigerated overnight, filtered and dried under vacuum at 40 ºC overnight to yield THPTA as an off-white solid (78% yield). ^{1}H NMR spectral data agrees with literature.[154] ^{1}H NMR (500 MHz, DMSO, 298 K) δ 8.03 (s, 1H), 4.65 (t, 1H, *J* = 5.0 Hz), 4.41 (t, 2H, *J* = 7.1 Hz), 3.62 (s, 2H), 3.40 (dd, 2 H, *J* = 11.3, 5.9 Hz), 2.06 – 1.88 (m, 2H, *J* = 6.5 Hz).

2.5.2 Small molecule studies

As a representative example the conditions of 1 M fuel and 32 mM Cu-THPTA are described. $Cu(OAc)_2●H_2O$ (6.34 mg, 32 μmols) and THPTA (14.35 mg, 32 μmols) were dissolved in water (0.811 mL) in a 1 dram glass vial. 2-Azidoethanol (76.0 uL, 1 mmol) and 3-dimethylaminopropyne (0.113 mL, 1 mmol) were added to a 1 mL conical tube. Reaction was initiated by transferring 2-azidoethanol and 3-dimethylaminopropyne to the prepared Cu-THPTA solution. The reaction volume was kept at a constant 1 mL for all experiments. The temperature was logged every second with a Handheld Data Logger Thermometer with Graphic Display purchased from OMEGA TM with a resolution of 0.1 ºC and an accuracy of 0.2 ºC. For the small molecules studies a K-type thermocouple was used with a 3 mm thick probe.

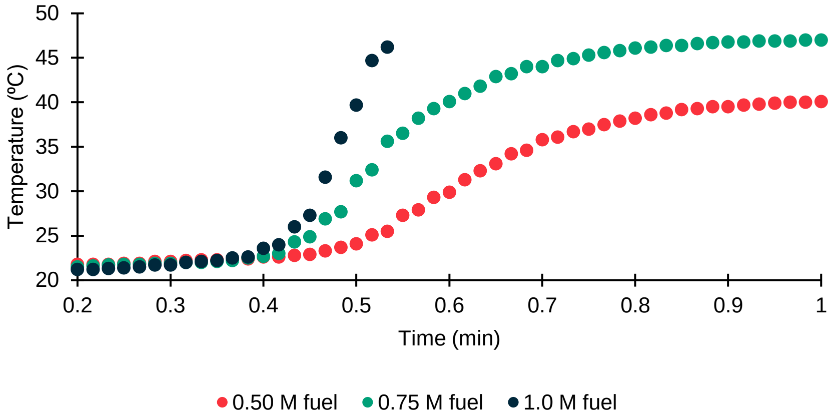

Figure 2.4 Temperature profiles of small molecule CuAAc reactions at different concentration of fuels (32 mM Cu-THPTA).

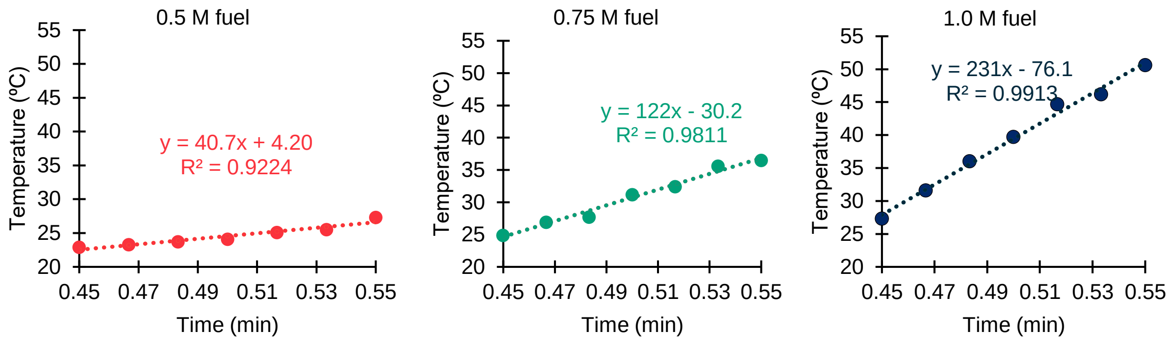

Figure 2.5 Temperature increase with time for small molecule CuAAc reactions at different fuel concentrations (32 mM Cu-THPTA)

Table 2.1: Analysis of temperature graphs for small molecule CuAAc reactions at different fuel concentrations (32 mM Cu-THPTA)

Fuel (M)	Max Temperature (ºC)	Slope (ºC/min)
0.50	40.2	40.7
0.75	47.0	122
1.0	63.2	231

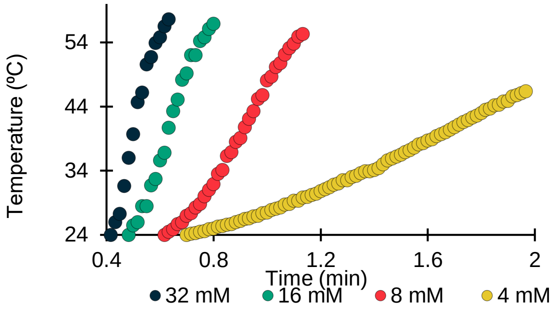

Figure 2.6 Temperature profiles of small molecule CuAAc reactions at different concentration of Cu-THPTA catalyst (1 M for both fuels).

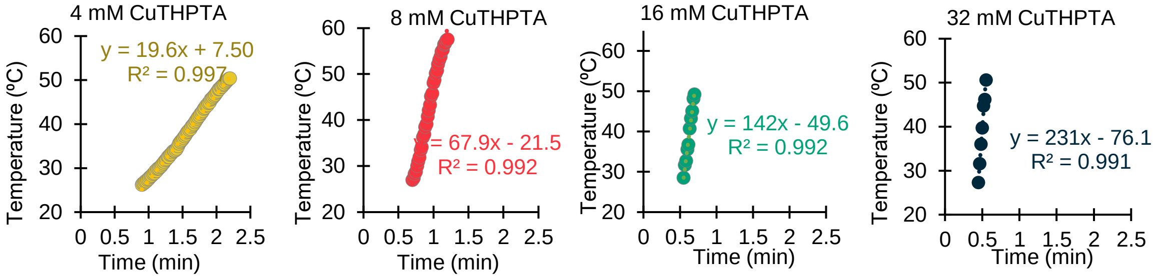

Figure 2.7 Temperature increase with time for small molecule CuAAc reactions at different concentration of Cu-THPTA catalyst (1 M for both fuels)

Table 2.2 Analysis of temperature graphs for small molecule CuAAc reactions at different concentration of Cu-THPTA catalyst (1 M for both fuels)

Cu-THPTA (mM)	Max Temperature (^{o}C)	Initial Slope (^{o}C/min)
4	53.3	19.6
8	60.0	67.9
16	62.4	142
32	63.2	231

2.5.3 Synthesis and characterization of polymers

Temperature-responsive polymers:

Synthesis of temperature-responsive pNIPAAm nanoparticles

pNIPAAm nanoparticles (NP) were synthesized following the literature reported protocol.[156,157] NIPAAm was recrystallized from hexanes and stored in refrigerator until ready to use. To a flask equipped with a stir bar, NIPAAm (64.4 mg, 0.569 mmols) was added and dissolved with MilliQ water (3.52 mL). Stock solutions of *N,N'*-methylenebis(acylamide) (10 mg/mL), sodium dodecyl sulfate (5 mg/mL), and potassium persulfate (10 mg/mL) were prepared fresh using MilliQ water. *N,N'*-methylenebis(acylamide) (0.63 mL stock solution, 6.3 mg, 0.0409 mmols) was added to the NIPAAm solution and the solution was sparged with nitrogen gas for 15 minutes before the addition of sodium dodecyl sulfate (0.36 mL stock solution, 1.8 mg, 0.00624 mmols). The monomer solution was sparged for an additional 5 minutes then immersed in 70 ºC oil bath for 10 minutes. A sparged solution of potassium persulfate (0.5 mL stock solution, 5 mg, 0.0185 mmol) was added and the vessel was kept at 70 ºC for 3 h. The solution became turbid within 30 minutes. After 3 h the solution was exposed to air, cooled and transferred to a dialysis bag (molecular weight cut-off 12,000 g/mol). The nanoparticles were dialyzed against water for 3 days changing the water twice a day. The concentration of the NPs was determined gravimetrically to be 16 mg/mL.

Synthesis of temperature-responsive macroscopic pNIPAAm hydrogel

pNIPAAm hydrogels were synthesized following the literature reported protocol.[158] NIPAAm (100 mg, 0.884 mmols), *N,N'*-methylenebis(acylamide) (5 mg, 0.032 mmols, 3.6 mol% crosslinking relative to NIPAAm) were dissolved with dry DMSO (0.9 mL) and sparged with nitrogen for 10 minutes. A freshly prepared stock solution of ammonium persulfate (20 mg/mL in DMSO) was sparged with nitrogen for 10 minutes. Ammonium persulfate (0.1 mL of the stock, 2 mg, 0.009 mmols) was added to the monomer and crosslinker solution, followed by *N, N, N', N'*-tetramethylethylenediamine (TEMED, 20 uL, 0.133 mmols). The reaction flask was immediately placed in a refrigerator at 0 ºC for 3 days. The gel was removed from the test tube using a spatula and addition of water to hydrate the gel. To remove residual monomer the gel placed in 1 L of water and the water was replaced twice a day for 3 days.

Investigation of swelling and deswelling of bulk hydrogels

The swelling and deswelling properties of the pNIPAAm cylindrical hydrogels (~0.5 g scale) were probed gravimetrically. The weight percent (wt%) of the gels were normalized to the initial weight of the gel at room temperature. The gel was then transferred to a 40 ºC water bath for 2 minutes before the mass was recorded. The gel was then transferred to a 20 ºC water bath for 2 minutes before the mass was recorded again. This cycle was repeated four times to demonstrate the reversible, rapid and large LCST transition which is attributed to the cryogenic polymerization conditions which have been reported to produce a macroporous structure.[158]

Synthesis of asymmetric bilayer hydrogels

pNIPAAm hydrogels with fast temperature response were synthesized following the literature reported protocol.[158] Working under inert atmosphere NIPAAm (100 mg, 0.884 mmols), *N,N'*-methylenebis(acylamide) (5 mg, 0.032 mmols, 3.6 mol% crosslinking relative to NIPAAm were added to a vial and dissolved in dry DMSO (0.9 mL). A stock solution of ammonium persulfate (20 mg/mL in DMSO) was prepared. Ammonium persulfate (0.1 mL of the stock, 2 mg, 0.009 mmols) and *N, N, N', N'*-tetramethylethylenediamine (TEMED, 20 uL, 0.133 mmols) wwere added to the monomer and crosslinker solution. The pregel solution was quickly transferred to a Teflon dish using a syringe and immediately placed in a refrigerator at 0 ºC for 30 min. After

30 minutes an equivalent volume of pregel solution prepared with 75 mol% acrylamide relative to NIPAAm was transferred to the existing frozen pregel solution. After 3 days of polymerization at 0 ºC the bilayer gel was removed from the Teflon mold. To remove residual monomer, the gel was placed in 1 L of water. The water was replaced twice a day for 3 days.

Dynamic light scattering (DLS) characterization of nanoparticles

DLS measurements were acquired on a Malvern Setasizer ZS Nano DLS. The refractive index of polyacrylamide of 1.490 was used. The solvent used was MilliQ water and the value for viscosity at 21.0 ºC was 0.9781 cP and a refractive index of 1.330. The Z-average diameter (236 nm) and polydispersity index (PDI) (0.043) is reported as an average of 3 measurements with 10 scans each taken at 21.0 ºC. The response to temperature was determined using 1 measurement consisting of 10 scans at each temperature from 16.0–48.0 ºC at 2 ºC increments with a 15 second equilibration time between different temperatures.

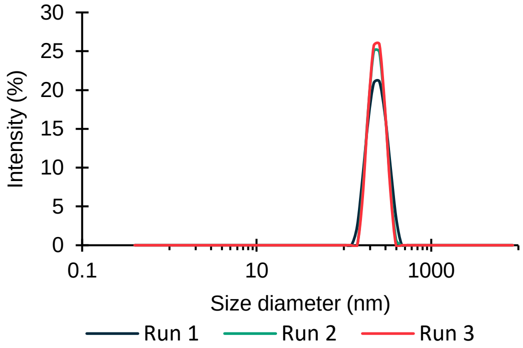

Figure 2.8 Size distribution of pNIPPAm NPs at 21 ºC measured by DLS.

Table 2.3 Summary of DLS data for pNIPPAm NPs at 21 ºC

Z-average diameter (nm)	PDI
233	0.056
236	0.009
238	0.063

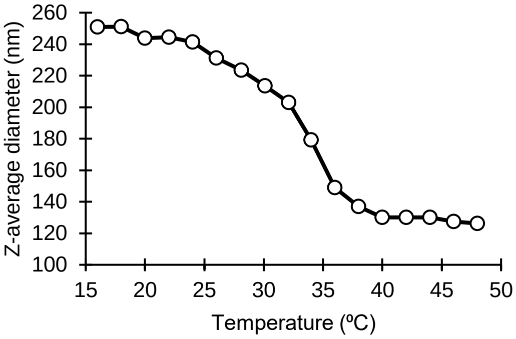

Figure 2.9 Temperature dependence of pNIPPAm NP size measured by DLS

Table 2.4 Temperature dependence of pNIPPAm NP size measured by DLS

Temperature (^{o}C)	**Z-average diameter (nm)**	**PDI**
16	251.0	0.002
18	251.1	0.042
20	243.8	0.047
22	244.4	0.002
24	241.4	0.026
26	231.3	0.055
28	223.5	0.011
30	213.6	0.067
32	203.0	0.016
34	179.3	0.019
36	148.9	0.019
38	137.0	0.030
40	130.1	0.010
42	130.1	0.008
44	130.1	0.013
46	127.5	0.043
48	126.2	0.052

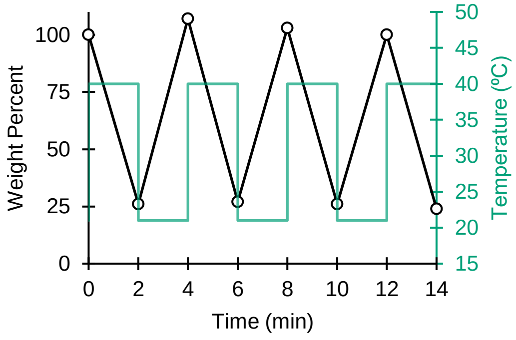

Figure 2.10 Swelling and deswelling properties of macroscopic hydrogel with response to changes in temperature. Weight percent was normalized to initial weight at room temperature.

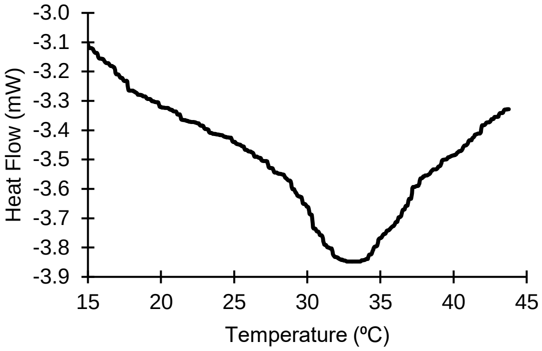

Figure 2.11 Differential scanning calorimetry of macroscopic hydrogel showing 32 ºC LCST transition.

2.5.4 Turbidity experiments for temperature-responsive NPs

Experimental protocol for turbidity measurements

Measurements were collected on a Cary-60 UV/Vis spectrophotometer. The Scanning Kinetics software was used to recorded transmittance from 500-850 nm every 0.3 min at 10 nm intervals (scan rate 72 nm/min). The same protocol was used as for small molecule exothermic experiments. A microcuvette made of optical glass was used as the vessel. For turbidity experiments the solution was pipetted up and down to ensure homogeneity. The pNIPAAm NP concentration at the start of the experiment was 2 mg/mL. Every 15 minutes an additional 1 mmol of each fuel was added as a neat solution of 3-dimethylaminopropyne (0.113 mL, 1 mmol), and 2-azidoethanol (76.0 uL, 1 mmol). The control was performed in the same fashion with the exception that there was no addition of pNIPAAm NP. Based on the small molecule studies both scenarios should generate heat, but with pNIPAAm NP present there was an associated change in turbidity.

Experimental protocol for visual turbidity experiments

For visual turbidity experiments, the same protocol described in the small molecule experiments was repeated using polystyrene semi-microcuvette as the vessel. *In situ* temperature was recorded every second with a Handheld Data Logger Thermometer with Graphic Display purchased from OMEGA TM using a 1 mm thick K-type thermocouple. The change in optical properties were visualized by taping a small figure to the outside of a cuvette and monitoring visual properties using a Canon EOS 5D Mark II camera with a Macro Lens EF 100 mm. An illuminator (Porta-trace, Model 1012, 16 Watt) was placed behind the cuvette to improve image quality. Video analysis and processing was performed using Shotcut, and quantitative analysis was performed using ImageJ. Scale bar was set using known diameter of the cuvette.

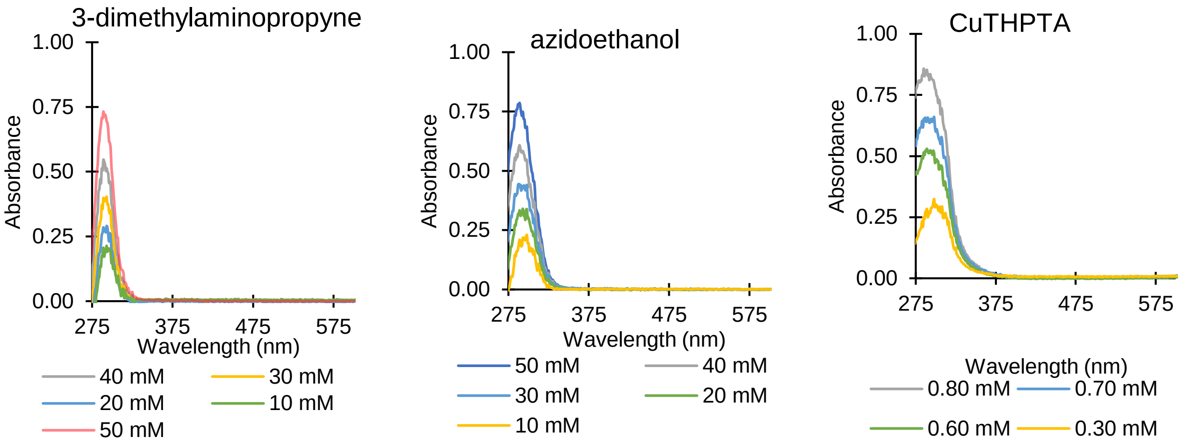

Figure 2.12 UV/Vis spectra of dimethylaminopropyne, azidoethanol and CuTHPTA.

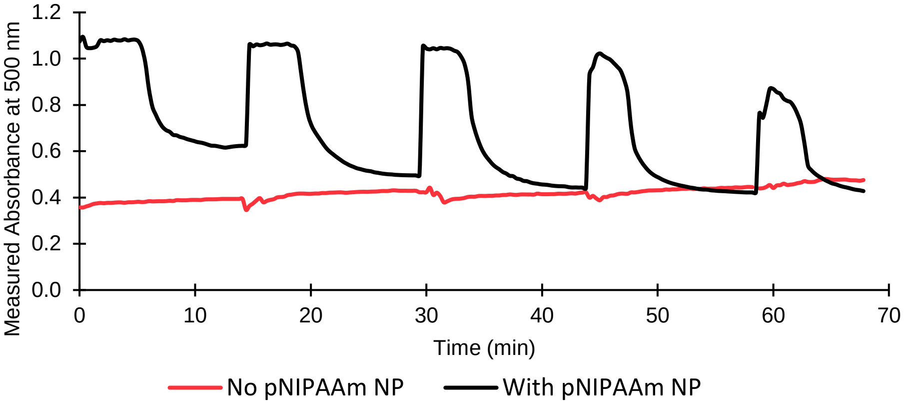

Figure 2.13 Absorbance at 500 nm for systems with and without pNIPAAm NPs

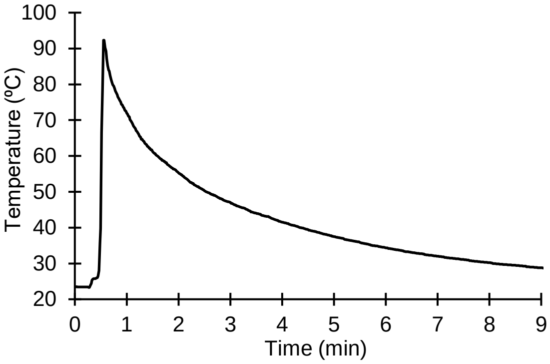

Figure 2.14 Temperature change with time recorded for visual turbidity experiment associated with Figure 2B (2 mg/mL pNIPAAm NP, 32 mM Cu-THPTA, 1 M fuels, 1 mL scale).

2.5.5 Macroscopic hydrogel experiments

Experimental protocol for visualizing deswelling of macroscopic hydrogels

To aid in visualization the gel was stained with Congo Red dye (1 mg/ml) solution in water for 10 minutes. The residual unbound stain was washed by incubating gel in water for 2 min (x3). The gel was then transferred to a plastic 6-well plate and placed over an illuminator (Porta-trace, Model 1012, 16 Watt). A freshly prepared stock solution of Cu-THPTA (0.811 mL 39.5 mM) in water was added, such that after the addition of 1 mmol of fuel (76 uL of 2-azidoethanol and 0.133 mL of 3-dimethylaminopropyne) the final concentration of catalyst was 32 mM and the fuel concentration 1 M. The visual appearance of the gel was monitored from above using a Canon EOS 5D Mark II camera with a Macro Lens EF 100 mm. Video analysis and processing was performed using Shotcut, and quantitative analysis was performed using ImageJ. Scale bar was set using known diameter of the 6-well plate. For *in situ* temperature monitoring while recording visual response, a 1 mm K-type thermocouple with a Handheld Data Logger Thermometer with Graphic Display purchased from OMEGA TM with a resolution of 0.1 ^{o}C and an accuracy of 0.2 ^{o}C was used. VideoS2 was played at x50.

Experimental protocol for visualizing actuation of macroscopic hydrogels

The same experimental conditions were used as described above in the protocol for visualizing deswelling of macroscopic gels except for the hydrogel. An asymmetric bilayer hydrogel was used instead. To position to the bilayer such that the actuation occurred in the field of view parallel to the camera, the gel was affixed with Super Glue to a piece of polydimethylsiloxane.

Experimental protocol for prototype engine demonstration

To aid in visualization the gel was stained with Congo Red dye (1 mg/ml) solution in water for 10 minutes. The residual unbound stain was washed by incubating gel in water for 2 min (x3). The gel was affixed to a toothpick using Super Glue, and the copper weight was attached by physically joining the two ends of the curled piece of copper wire. The gel was then transferred to a polystyrene semi-microcuvette and placed over an illuminator (Porta-trace, Model 1012, 16 Watt). To this a freshly prepared stock solution of Cu-THPTA (0.811 mL 39.5 mM) was added, such that after the addition of 1 mmol of fuel (76 uL of 2-azidoethanol and 0.133 mL of 3-dimethylaminopropyne) the final concentration of catalyst was 32 mM and the fuel concentration

1 M. The visual appearance of the gel was monitored from side using a Canon EOS 5D Mark II camera with a Macro Lens EF 100 mm. Video analysis and processing was performed using Shotcut, and quantitative analysis was performed using ImageJ. Scale bar was set using known width of the cuvette.

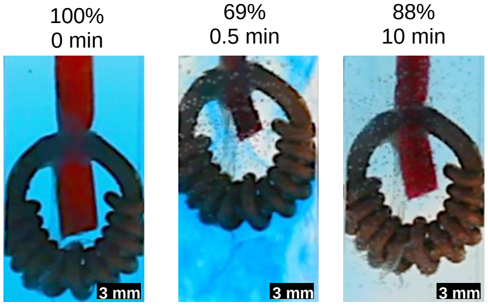

Figure 2.15 Macroscopic work by lifting an object**.** Mass lifted by a 5 mg dry polymer sample could be as high as 530 mg. The large mass was achieved by coiling copper wire around another piece of wire. The percent length of the pNIPAAm hydrogel, relative to 0 min, was reported above the image along with the time stamp. Scale bar is 3 mm.

2.5.6 Calculations for power output

The mean power output was determined following using for the following formula.[164]

$$P = \frac{\Delta W}{\Delta t} = \frac{m * \ g * \Delta h}{\Delta t} = 1.09 * 10^{-6}\ Watts$$

P = mean power

W = work performed

m = mass that was lifted. Obtained by weight copper wire prior to attachment to hydrogel = ($5.3\text{x}10^{-4}$ kg)

g = acceleration due to gravity = 9.81 m/s^2

Δh = height that the mass was lifted = length of gel at 0 s – length of gel at 30 s. Obtain by measurements using ImageJ of gel length over time in the video = 0.00631 m

Δt= time it took to lift mass to given height = 30 s

Specific power as a figure of merit for engine comparison

A common figure of merit is the power to weight ratio.[144,165] In the case of straited muscle the power to weight ratio is ~200 W/kg and in hydrogel engines it's 0.2 W/kg. [144,164,165] The power to weight ratio (relative to the dry gel), was found to be on par with other reported hydrogel engines.

$$\frac{Power}{Weight} = \frac{P}{weight\ of\ dry\ gel} = 0.218\ W/kg$$

Note this calculation does not take in account the work associated with the LCST transition, because the energetics of which are not agreed upon in the community and range from 3-13 kJ/mole.[155]

2.5.7 NMR spectra

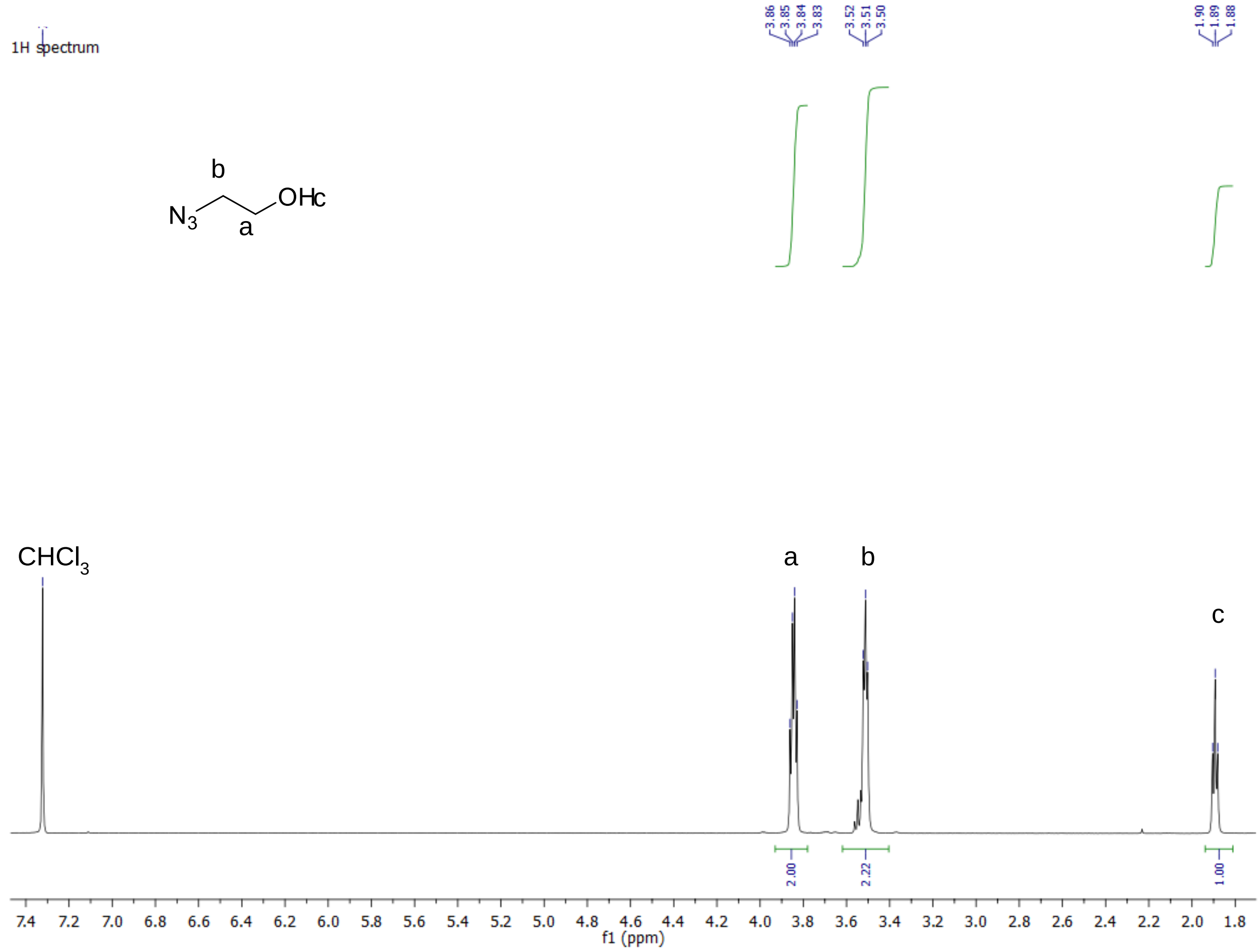

Figure 2.16 ^{1}H NMR spectrum of 2-azidoethanol in $CDCl_3$.

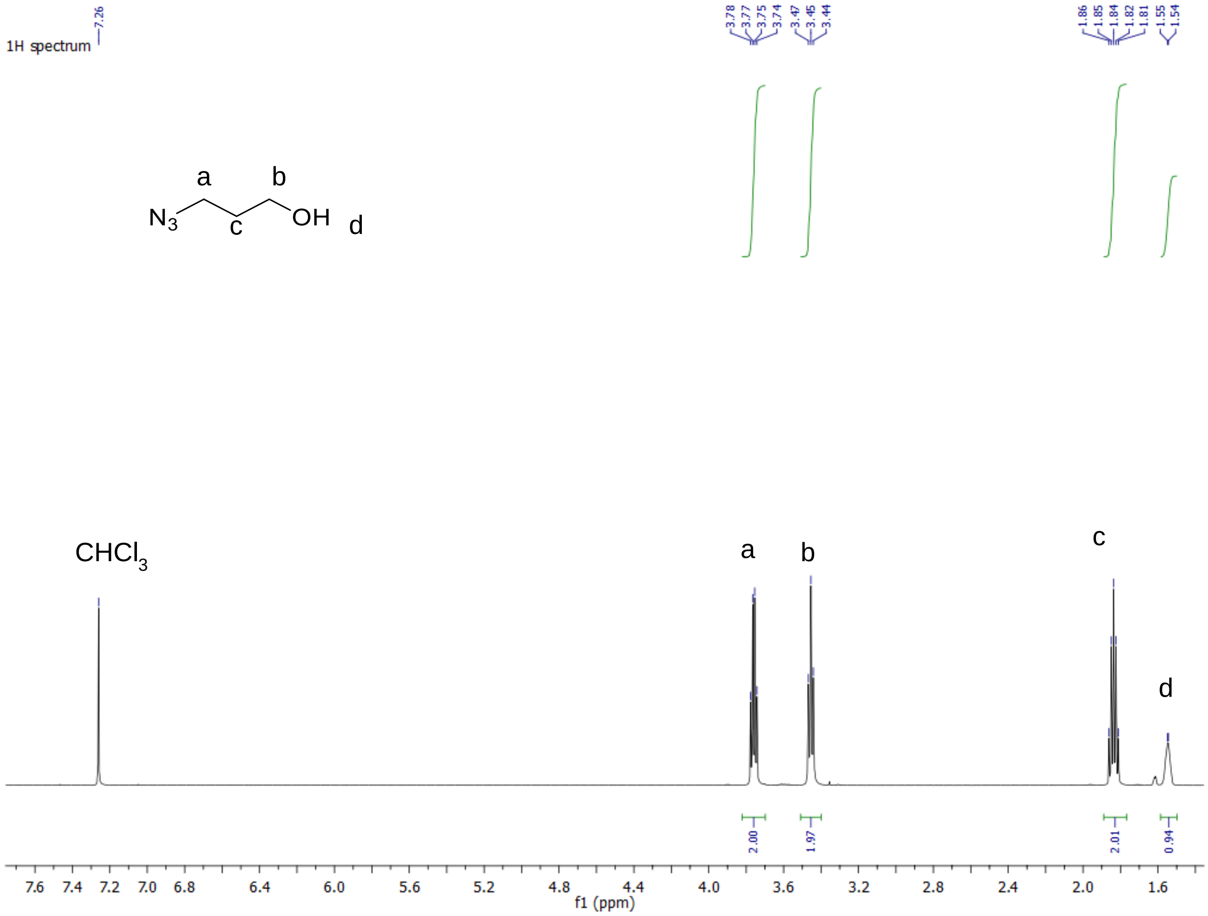

Figure 2.17 ^{1}H NMR spectrum of 3-azidopropanol in $CDCl_3$.

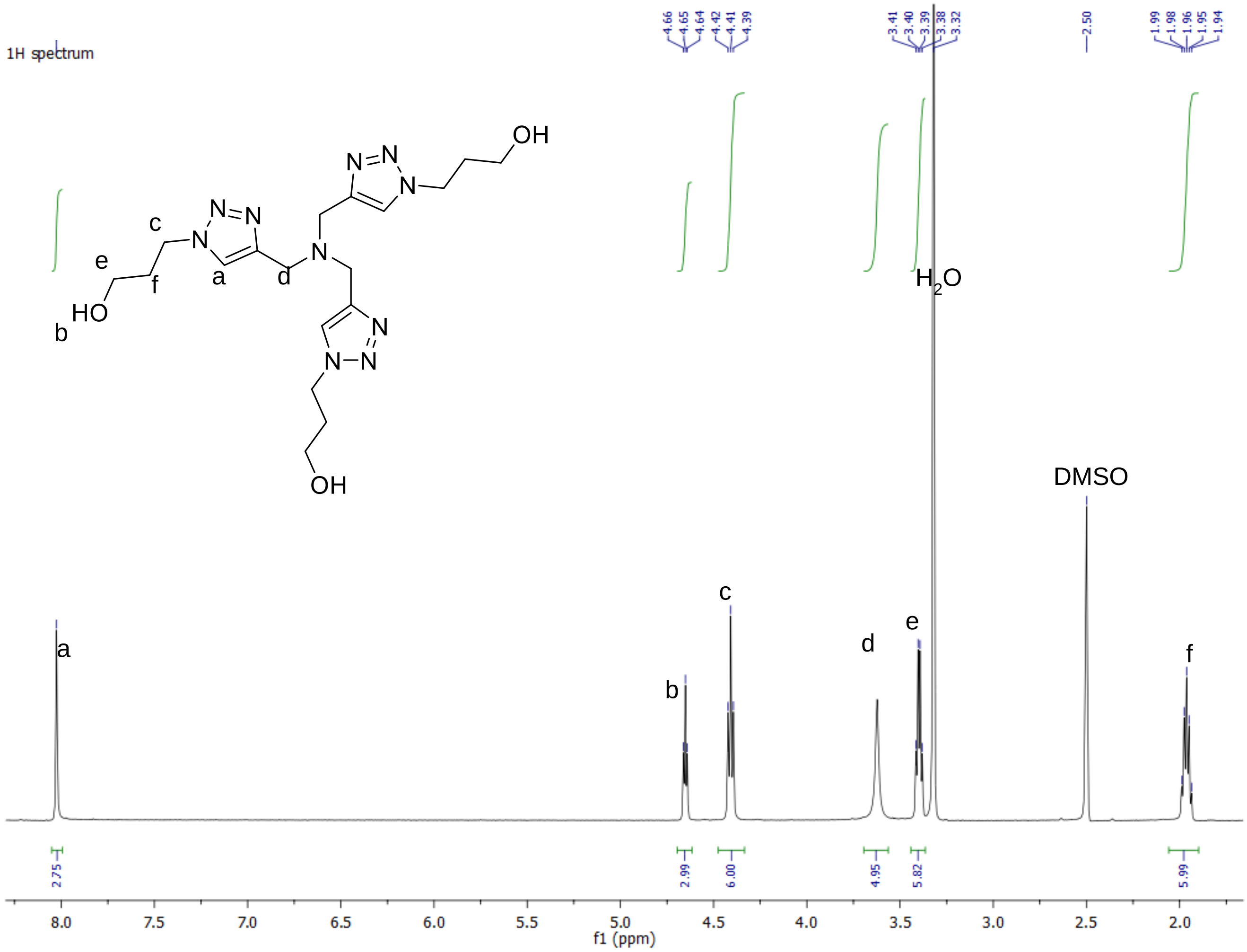

Figure 2.18 ^1H NMR spectra of tris(3-hydroxypropyltriazolylmethyl)amine (THPTA) in d_6-DMSO.

Chapter 3: Progress Towards Self-regulating Materials

3.1 Introduction to self-regulating materials

In pursuit of bioinspired materials, scientists aim to solve complex materials problems by drawing inspiration from the solutions nature has developed over millions of years of evolution.[166] Bioinspired materials research has given rise to significant advancements in the field of smart materials.[44] Recently, there is a growing interest to more closely mimic biology by creating smart materials that operate out-of-equilibrium.[32,46] In living organisms, nonequilibrium systems consume and dissipate energy to the environment to power important life processes such as cell division and cellular motility.[133] Operating far from equilibrium gives rise to advanced adaptive behavior by interactively interfacing with the environment.[13,36]

Nonequilibrium system in biology give rise to various forms of adaptive behavior such as self-healing, self-regulating, memory, and even learned behavior.[12] In nature, self-regulation occurs across all length scales; from the molecular scale as seen in insulin regulation,[167] to the macroscopic scale such as the emergent patterns on zebrafish.[12,128] Adaptive nonequilibrium systems in nature can demonstrate learned behavior with varying degrees of complexity.[168,169] Biochemical circuits are one of the simpler forms of learning that capitalize on programmed responses to various stimuli in an orthogonal fashion to yield associative learned behavior.[170] Synthetic materials able to mimic even the simplest forms of learned behavior are just beginning to emerge as an area of interest due to the potential to create artificial living materials.[36,132] The ability to replicate this level of control in synthetic nonequilibrium materials would allow scientist to create truly life-like materials with significant impacts in the field of medical implants and sustainable materials for energy usage.[171–173]

The pursuit of synthetic nonequilibrium materials with self-regulatory properties takes advantage of a variety of opposing chemical and physical feedback loops.[171] A common approach is to pair two opposing feedback loops, as seen in the example by Hauser *et al.* that uses photothermally generated Marangoni stresses and capillary forces on a fluid interface to achieve nonequilibrium oscillatory movement on the millimeter scale.[174] Photochemical coupling of a *trans*/*cis* isomerization of azobenzene-based liquid crystals to the mechanical deformation has also demonstrated oscillatory behavior attributed to a self-shadowing mechanism.[175] Biological systems ubiquitously use chemical driving forces coupled with mechanical deformations to drive self-regulation.[60] While there are examples of chemically driven, self-regulatory manmade systems in the field of system chemistry—it remains a challenge to extend this behavior to self-regulation of macroscopic mechanical deformations.[32,176] He *et al.* demonstrated a synthetic mimic using a catalytic exothermic reaction coupled with mechanical actuation of a biphasic system to yield a system able to regulate temperature on a 2-dimensional surface.[124] To better mimic biology it is imperative to develop chemically driven nonequilibrium materials with macroscopic mechanical self-regulatory behavior in 3-dimensions.

3.2 Our design of self-regulating materials

Here we describe progress towards the development of chemically driven self-regulatory nonequilibrium systems. We employ hydrogels with lower critical solution temperature (LCST) phase transition that induce chemothermal mechanical actuation to switch on and off a catalyzed exothermic reaction to achieve self-regulation of temperature. Below we outline the key design features in pursuit of a 3-dimensional self-regulating system.

The role of the LCST polymer in the system is to control the reaction rate of the exothermic reaction. At temperatures below the LCST transition, hydrogels are swollen and have a large mesh size allowing for diffusion of chemical fuels to the catalytic sites grafted onto the hydrogels. At temperatures above the LCST hydrogels shrink by expelling water, resulting in a decrease in mesh size of crosslinked polymer networks. In the collapsed state the hydrogel should limit the diffusion of reactants to the buried catalytic sites, which is expected to turn off the catalyzed exothermic reaction and corresponding heat generation. To establish two distinct on and off states it is vital to design an LCST-type polymer with a large, rapid and reversible LCST transition. The large degree of change between the swollen and collapsed state will dictate the relative rates of reaction. The transition needs to occur very rapidly to ensure high reaction turnover to generate sufficient heat to cause an LCST transition. Additionally, the LCST transition must be highly reversible to allow for multiple cycles to achieve self-regulation. Poly-N-isopropyl acrylamide (pNIPAAm),[151] and comb-type polyethylene glycol (PEG)[177] polymers are well known for their LCST behavior and were employed in efforts reported here to develop a self-regulating nonequilibrium material. The comb-type architecture of PEG was investigated due to the increased potential to shut off catalytic activity due to the sterically congested nature of the polymer architecture.

The chemical reaction used in the self-regulating device had to fit several design criteria including that it be catalyst controlled, compatible with aqueous solvent, highly exothermic and have a high reaction rate. To modulate the reaction rate, a catalytic reaction was so chosen such the reaction rate can be tuned through controlling the diffusion to the catalytic species. The chosen reaction also must be compatible with aqueous solvents because the LCST transition is fundamentally driven by hydrogen bonding of water to the polymer sidechains. Lastly, the reaction chosen must by highly exothermic in nature to generate enough heat to trigger an LCST transition. For these reasons, we chose the copper catalyzed azide alkyne cycloaddition (CuAAc) – referred to as a “click reaction”- which is commonly used in aqueous solvents, catalytic and is reported to have reaction enthalpies of nearly 50 kcal/mole.[152] To ensure high reactions rates, ligands were added to complex with the Cu(I) catalyst.[153] Previous reports have shown that tris(3-hydroxypropyltriazolylmethyl) amine (THPTA) to complex Cu results in increased catalytic activity for CuAAc reactions compared to uncomplexed copper.[153] Complexation of the Cu catalyst is also necessary in order to tether the catalyst to a polymer or nanoparticle support. In addition to THPTA, ligands with higher binding affinities to Cu,[178,179] such as nitrilotriacetic acid (NTA)-based ligands were explored. The higher binding affinities were investigated to minimize potential leaching of the copper catalyst due to the competitive binding effects from the triazole waste from the chemically fueled process.

The rate of heat generation is also dependent on the architecture of the polymer and catalyst attachment. For this reason, a variety of different architectures including macroscopic bulk hydrogel, meso-scale hydrogels, as well as nanogels were explored. It should also be noted that in the systems investigated the catalyst attachment was accomplished *via* copolymerization of an acrylate-bearing ligand to allow for loading of the Cu catalyst by swelling the gel in a Cu solution. This approach of copolymerization results in a system where the LCST properties and the catalyst loading are dependent on one another due to the change in hydrophilicity of the copolymer network. For this reason, alternative architectures such as core-shell nanoparticles were also explored.

3.3 Results and discussion

3.3.1 Bulk hydrogel approach

To achieve distinct regimes of active and inactive catalysis macroscopic hydrogels with large, fast, and reversible LCST transition were investigated. N-isopropyl acrylamide (NIPAAm) was chosen as the monomer and N,N'-methylenbisacrylamide as the crosslinker. The polymerization was performed in cryogenic conditions in dimethylsulfoxide (DMSO) to achieve a macroporous structure that is reported in literature to produce large, and rapid LCST tranition.[158] The LCST behavior was probed gravimetrically by immersing the gel in 21 ºC then 40 ºC to mimic oscillatory change in temperature expected for a self-regulating system. The degree of deswelling at 40 ºC was found to be ~25 % of the original weight, indicating a rather large change in swell behavior. This result was repeatable, as shown in the 5 oscillatory cycles shown in the navy curve in Figure 3.1a. The rate of deswelling was observed to be under 2 minutes indicating rapid deswelling which was attributed to the macroporous nature of the hydrogel, consist with literature.[158]

The degree of swelling of gel in the presence of the chemical fuels was investigated. As discussed in Chapter 2, alkyl azides and N,N-dimethylaminopropyne are highly reactive for CuAAc, and thus were used for this work. In the presence of N,N-dimethylaminopropyne (1 M) the gel deswelled to 75 wt% of the original water swollen state (Figure 3.1b). The initial azide investigated was 3-azidopropanol; which, upon equilibration of the gel in 3-azidopropanol (1 M) the degree of swelling of the gel decreased to 39% (Figure 3.1b). While these values are after equilibration (1 h), because the system is designed to operate multiple cycles, the deswelling of the gel over time in response to fuel (or waste product) accumulation is problematic as it convolutes the heat associated deswelling. Lower concentration of fuels minimizes the deswelling effect, but only slightly (Figure 3.1b). By further decreasing the hydrophobicity of the fuel by decreasing the carbon chain from 3 to 2, resulted in significantly less deswelling, 104% compared to 79% at

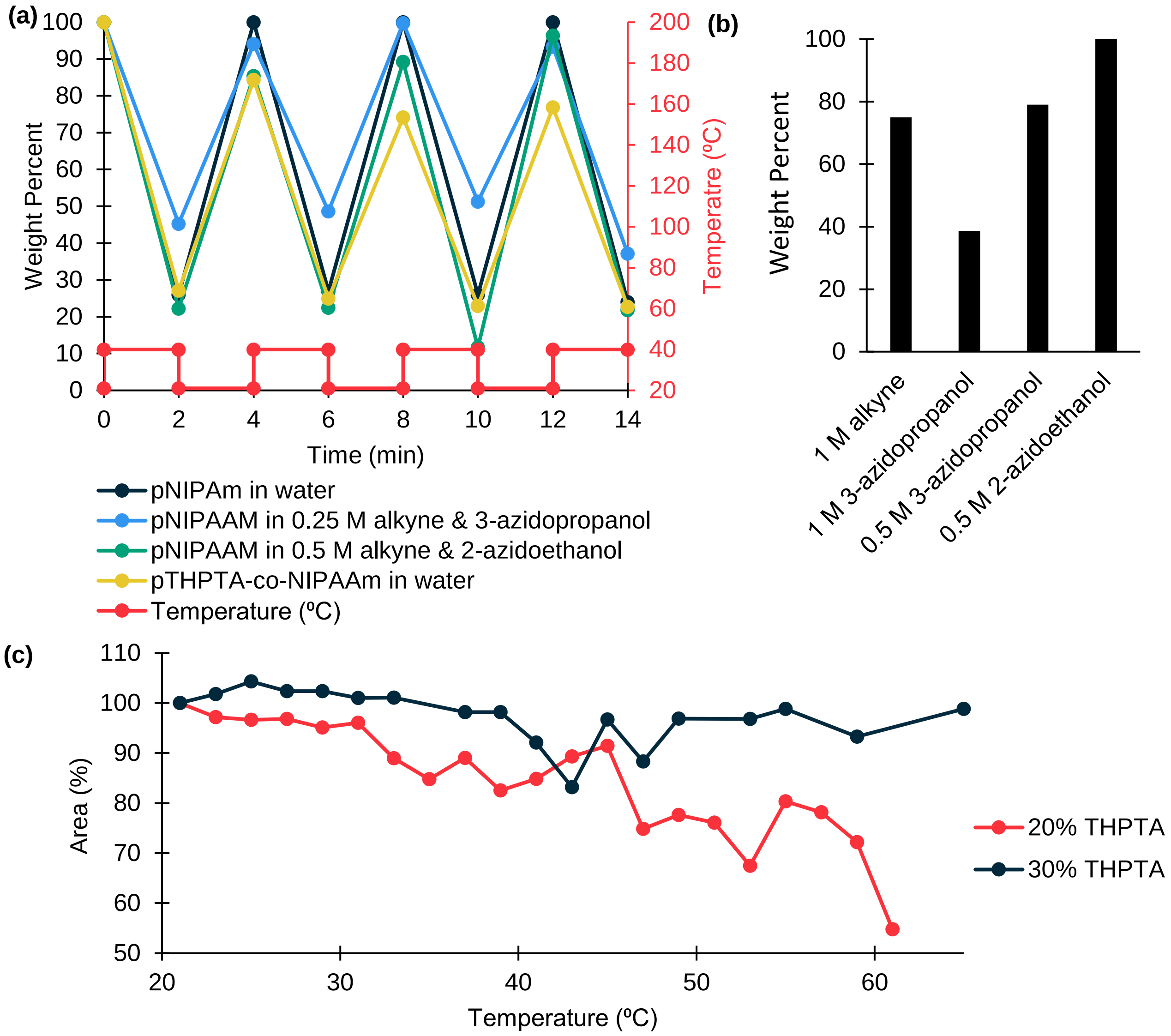

Figure 3.1 Characterization of bulk macroscopic hydrogels. (a) Degree of swelling was determined gravimetrically and normalized to weight of gel at 21 ºC after equilibration in water. Deswelling with increase in temperature oscillating between 21 ºC and 40 ºC for 2 minutes each is reported on the left vertical axis for the following hydrogels pNIPAAm in water (navy), pNIPAAm in 0.25 M each fuel N,N-dimethylaminopropyne and 3-azidopropanol (blue), pNIPAAm in 0.50 M each fuel N,N-dimethylaminopropyne and 2-azidoethanol (green), and pTHPTA-coNIPAAm with 5 mol% feed ratio of THPTAmon relative to NIPAAM in water (yellow). Temperature is plotted in red on the right vertical axis. (b) pNIPAAM gels equilibrated in N,N-dimethylaminopropyne (1 M), 3-azidopropanol (1 M & 0.5 M), 2-azidopropanol (0.5 M) with weight normalized to weight of gel in water (c) Deswelling of 20 and 30 mol% THPTAmon relative to NIPAAm in feed ratio as a function of time. The area of a piece of gel was recorded at different temperatures and normalized to the area at 21 ºC.

0.5 M respectively (Figure 3.1b).

Next, to couple the Cu catalyst to the LCST transition, a LCST polymer with covalently attached catalytic Cu was prepared. THPTA was synthesized in two steps following literature precedent (Scheme 3.3),[154] followed by a statistically functionalization with methacrylic anhydride to yield THPTA attached to a methacrylate handle, termed THPTAmon, which could be copolymerized with NIPAAm (Scheme 3.4). The solubility of the THPTAmon in DMSO is sufficiently high to allow for copolymerization from a feed ratio of 0-50 mol% THPTAmon relative to NIPAAm. The reactivity ratios of methyl methacrylate and acrylamide favor the incorporation of the THPTA bearing monomer.[180] To determine the percent incorporation for these specific monomers linear polymers were synthesized and characterized by ^{1}H NMR to reveal 10% incorporation of THPTAmon with a 3.4 mole % feed ratio of THPTAmon, which is in the reported range of reactivity ratios (Figure 3.10).[180] Next, Cu(II) was loaded into the gel by immersion and equilibration of gel in a Cu(II) acetate solution, which resulted in the gel swelling and a clear color change from an opaque to a vibrant blue gel, attributed to the Cu(II) binding. The binding is attributed to coordination to THPTA copolymerized into the network because upon equilibration of the gel in water overnight the blue color persists.

The LCST properties of the catalytic pTHPTA-co-NIPAAm gels were probed gravimetrically. The copolymerization of NIPAAm with other monomers is known to impact the LCST behavior.[151] For gels synthetized with 5 mol% THPTAmon relative to NIPAAm the LCST properties were impacted minimally with the reswelling being slightly hindered, as shown in the Figure 3.1a yellow curve compared to navy curve. Increasing the THPTAmon monomer feed ratio to 20 mole % resulted in significant impacts to the LCST both in terms of the sharpness of the transition and the temperature the transition occurred, 60 ºC compared to the LCST of 32 ºC for pNIPAAM homopolymers (Figure 3.1c).[151] The 30 and 50 mol% THPTAmon samples did not exhibit any LCST phase transition below 80 ºC. A sufficiently high concentration of catalyst loading is necessary to facilitate heat generation; however, the impact on the LCST behavior must be minimized.

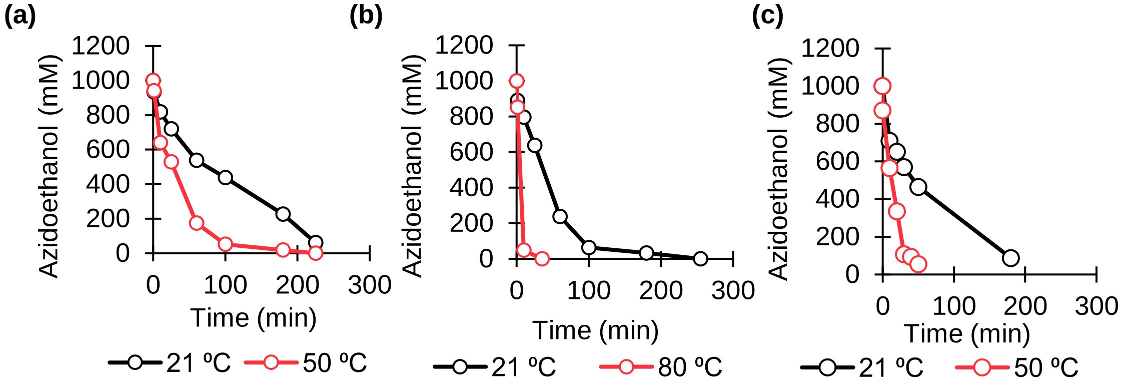

Figure 3.2 Reaction kinetics of catalytic THPTA-co-NIPAAm macroscopic hydrogels. The concentration of 2-azidoethanol is monitored using HPLC at various time points for gels with (a) 5 mol%, (b) 20 mol%, (c) 30 mol% THPTAmon relative to NIPAAm in the feed ratio at different temperatures.

Next the reaction rate was probed at various temperatures above and below the LCST. The reaction rate was expected to decrease at temperatures above the LCST due to decreased pore size and limited diffusion to active catalytic sites. For samples with no observed LCST the reaction rate was expected to increase with increased temperatures. The gel with the least THPTAmon (5 mol%) was expected to have the most substantial change in reactivity upon crossing the LCST transition due to the minimal change in LCST properties. The reaction rate was probed at 21 ºC and 50 ºC; however, the increase in temperature resulted in increased reaction rate as observed by the increased rate of 2-azidoethanol depletion (Figure 3.2a). A similar trend was observed with increased catalyst loading. The reaction rate of the 20 mol% THPTAmon gel was probed at a higher temperature due to the increased LCST, and the effect of temperature increase was even more pronounced as compared to the 5 mol% THPTAmon (Figure 3.2b). The 30 mol% THPTAmon gels did not have a measurable LCST up to 80 ºC, thus it was expected that the increase in temperature would increase reaction rate, which was in line with the observed reaction rates at 21 and 50 ºC seen in Figure 3.2c. These results demonstrate that the LCST transition does not shut down access to catalytic site sufficiently to compensate for the increased reaction rate due to temperature increase. It should be noted that for the 5 mol% THPTAmon gel we do not expect to reach temperatures as high as 50 ºC so at lower temperatures the change in access to active catalytic sites may be sufficient to compensate for the temperature increase.

Next the heat generation of the catalytical gels were probed by monitoring the temperature of the surrounding solution. It should be noted that locally (in the gel) the temperature is expected to be higher since that is the site of catalytic reaction. As control, the reaction was performed with the small molecule catalyst, CuTHPTA (32 mM), N,N-dimethylaminopropyne and 2-azidoethanol (1 M each fuel). To mimic any heat absorption a piece of pNIPAAM crosslinked gel was added to the solution. The maximum temperature of the surrounding solution for the control samples was measured to be 81 ºC (Figure 3.3a). We started with the highest catalyst loading in gels which is the 50 mol% THPTA gel that did not exhibit an LCST below 80 ºC. Initial studies were done with macroscopic pieces of gel in order to minimize the surface area due to the potentially open catalytic site on the external surface of the gel. It was expected that the covalent attachment of the catalyst into the polymer network should decrease the reaction rate and subsequently the overall heat generation. Even the highest catalyst loading gel (50 mol%) only resulted in maximum temperature of 30 ºC (Figure 3.3b). To increase the available surface area for fuel to diffuse into the polymer network to reach the active catalytic sites, the macroscopic gel was crushed into mm-sized pieces, which resulted in a maximum temperature of nearly 40 ºC (Figure 3.3c). The repeated addition of an equivalent amount of azide and alkyne fuel resulted in another increase in temperature reaching a maximum of 43 ºC (Figure 3.3c). This result, as well as HPLC analysis of the surrounding liquid indicated that the fuel had been converted to waste but did not generate as much heat in the surrounding liquid in comparison to the small molecule catalyst. The lack of heat generation was attributed to slow mass flow of azide and alkyne fuels to the catalyst sites. Since increasing the surface area of the bulk gels by crude methods (mechanical damage) to yield mm-sized pieces alleviated this problem—more refined methods of producing catalytic gels with reduced dimensions were pursued. Additionally, it was observed that over the course of several hours catalytic gels left in the 1 M waste solution leached copper catalyst into the surrounding solution, as evident by the blue color of Cu(II). Leaching is attributed to the much higher concentration of triazole product relative to THPTA, 1 M to 32 mM respectively.

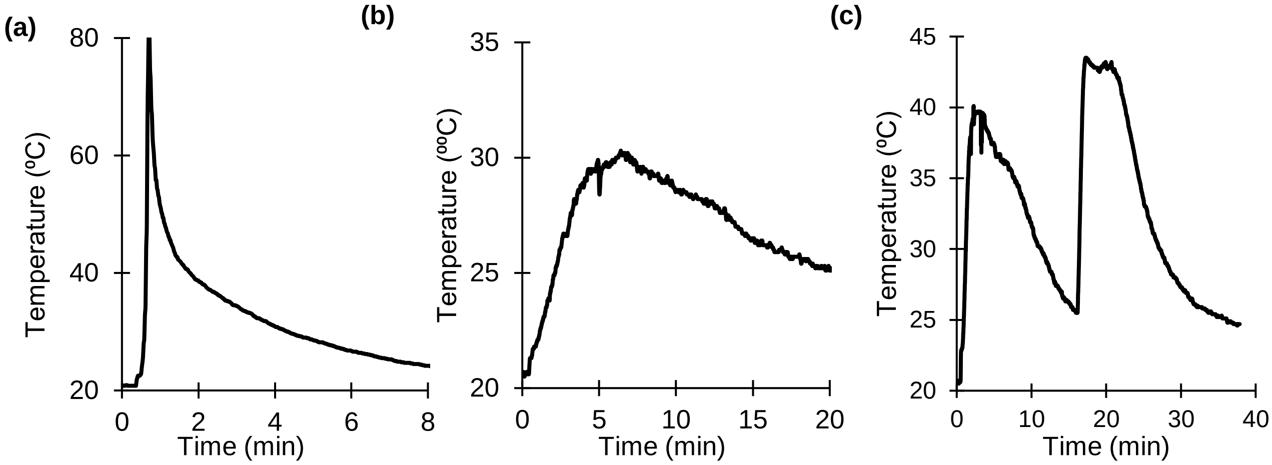

Figure 3.3 Heat generation of catalytic THPTA-co-NIPAAm hydrogels. (a) Control with CuTHPTA small molecule catalyst (32 mM) with 1 M each fuel, 2-azidoethanol and N,N-dimethylaminopropyne added at 0.25 min (b) 50 mol% THPTAmon relative to NIPAAm in feed macroscopic gels 0.62 cm^3 with a local concentration in the gel 60 mM and 32 mM concentration globally with 1 M each fuel, 2-azidoethanol and N,N-dimethylaminopropyne added at 0 min (c) 50 mol% THPTAmon relative to NIPAAm in feed macroscopic gels pulverized to mm size pieces with a local concentration in the gel 60 mM and 32 mM concentration globally with 1 M each fuel, 2-azidoethanol and N,N-dimethylaminopropyne added at 0 min.

3.3.2 Hydrogel nanoparticle approach

Two key design features—scale and catalyst ligand—were modified based on the results from the macroscopic hydrogel approach. A nanoparticle polymer system with increased surface area should allow for increased mass diffusion of the fuel to the active catalytic site. To address the leaching of the active Cu species from the backbone of the polymer into the surrounding solution, the binding affinity of the ligand was increased. Instead of THPTA as a ligand which has a dissociation constant of 1.1 x 10^{-10} for Cu(I)[178] a nitrilotriacetic acid (NTA) ligand with a dissociation constant of 6.0 x 10^{-11} which has three carboxylates for metal coordination instead of three triazole rings.[179]

The heat generation of model reaction was evaluated using CuNTA small molecule as the catalyst. Initial studies using 2-azidethanol (0.5 M) and N,N'-dimethylaminopropyne (0.5 M) and CuNTA (16 mM) did not result in any reaction progress and subsequently no heat generation. Upon addition of sodium ascorbate reaction proceeded rapidly and the overall temperature of the solution increased to 30 ºC (Figure 3.4a). Sodium ascorbate is necessary for the reduction of Cu(II) to the active Cu(I) species, which was not needed for CuTHPTA catalysis.[153] To conserve fuel, the system was brought to a higher temperature closer to the LCST such that less fuel had to be consumed before reaching the LCST. To mimic these conditions, heat generation experiments with small molecule catalyst CuNTA were performed and exhibited a temperature increase from 34 to 35.5 ºC (Figure 3.4b). The relatively smaller increase in temperature was due to more rapid heat dissipation due to the water bath around the reaction vessel, as compared to air cooling (Figure 3.4b).

After demonstration of small molecule catalysis with CuNTA, the NTA ligand was incorporated *via* copolymerization with NIPAAm. To allow for copolymerization an NTA bearing monomer was synthesized. NTA bearing a primary amine was synthesized according to literature precedent (Scheme 3.5),[181] followed by addition into acryloyl chloride in biphasic basic conditions with water and toluene to yield an acrylamide monomer bearing NTA, termed NTAmon (Scheme 3.6). Next the NTA monomer was incorporated at 5 mol% feed ratio into NIPAAm based nanoparticles (NPs), referred to as catalytic NP *via* precipitation polymerization.[156,157] The size

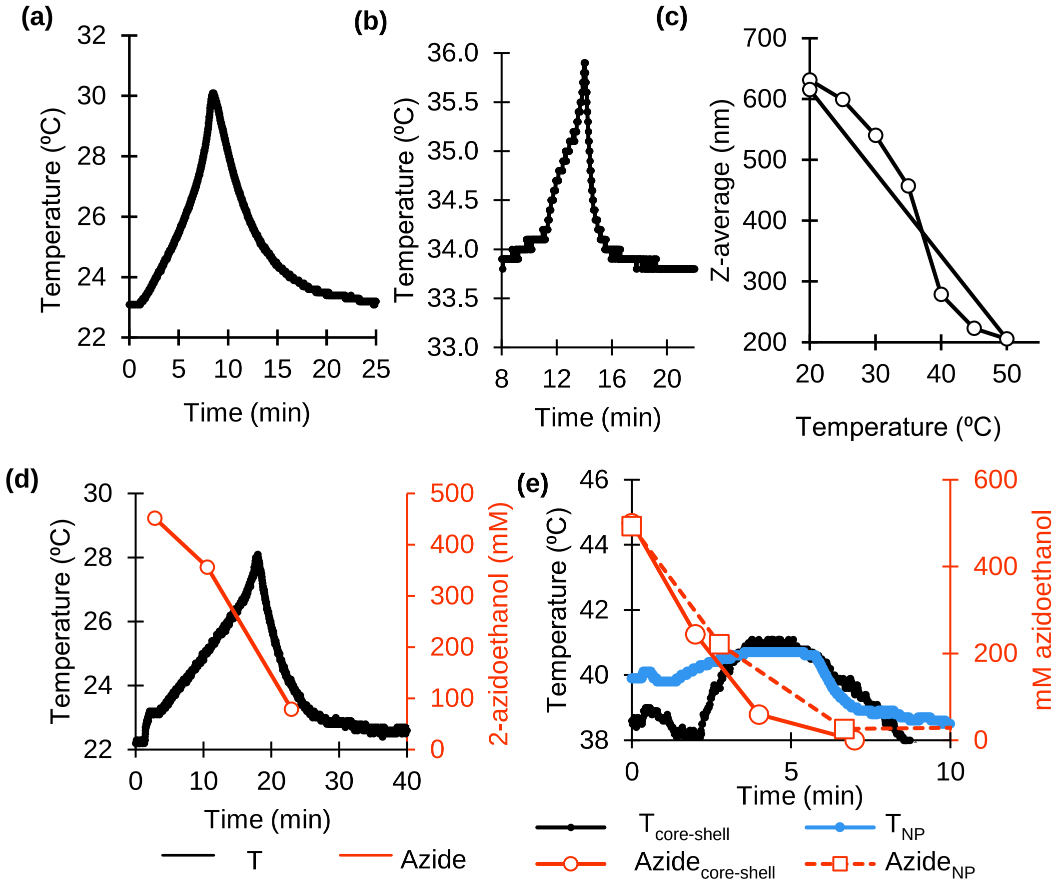

Figure 3.4 Catalytic CuNTA nanoparticle system. (a) Small molecule heat generation with CuNTA (16 mM) sodium ascorbate (32 mM), 2-azidoethanol (0.5 M), N,N-dimethylaminopropyne (0.5 M) (b) Small molecule heat generation with CuNTA (16 mM) sodium ascorbate (32 mM), 2-azidoethanol (0.5 M), N,N-dimethylaminopropyne (0.5 M) performed at a starting temperature of 34 ºC. (c) Z-average diameter of pNTA-co-NIPAAm with a 5 mol% NTAmon in the feed ratio after Cu(II) complexation by dynamic light scattering. (d) Heat generation experiments with pNTA-co-NIPAAm NP with a 5 mol% NTAmon in the feed ratio. Performed with CuNTA (16 mM), sodium ascorbate (32 mM), 2-azidoethanol (0.5 M), N,N-dimethylaminopropyne (0.5 M. Temperature of solution is reported on the left vertical axis and concentration of 2-azidoethanol is reported on the right vertical axis. (e) Heat generation experiments with pNTA-co-NIPAAm NP with a 5 mol% NTAmon in the feed ratio and core-shell NP with a shell of pNIPAAm homopolymer. Performed with CuNTA (16 mM), sodium ascorbate (32 mM), 2-azidoethanol (0.5 M), N,N-dimethylaminopropyne (0.5 M) Temperature of solution is reported on the left vertical axis and concentration of 2-azidoethanol is reported on the right vertical axis.

and temperature response of the nanoparticles were probed via dynamic light scattering (DLS) after complexation of Cu(II) (Figure 3.5). The LCST properties are shifted slightly to higher temperatures as compared to homo pNIPAAM polymers which is attributed to the increase in hydrophilicity.

Next the reaction rates and heat generation above and below the LCST were probed. The reaction rate was expected to decrease at temperatures above the LCST due to decreased pore size and limited diffusion to active catalytic sites. At temperatures below the LCST the high surface area was expected to allow for high mass diffusion to facilitate rapid heat generation. Starting the system at room temperature and mimicking the small molecule experiments from Figure 3.4a the maximum temperature achieved using the catalytic NPs was 28 ºC and the 2-azidoethanol was nearly depleted in less than 20 min (Figure 3.4c). The catalytic NPs achieved a maximum temperature of just 2 ºC lower than that of the small molecule indicating that the increased surface area allowed for faster mass diffusion to active catalyst sites as compared to the bulk gels. At temperatures above the LCST the catalytic nanoparticles exhibited a temperature increase of less than 1 ºC and consumption of 2-azidoethanol in less than 7 min (Figure 3.4e). This result indicated that the reaction proceeded faster at elevated temperatures regardless of the deswelling of the catalytic NPs associated with the LCST. This result was attributed to the exposed catalytic sites on the surface of the catalytic NP regardless of whether the particles is in the swollen or deswollen state.

3.3.3 Acrylamide core-shell nanoparticle approach

To minimize the available active sites on the surface of the catalytic NP, a core-shell NP system was designed. Using the catalytic NP described above as the core, we grew a shell of crosslinked pNIPAAM to serve as an added barrier at temperatures above LCST to minimize diffusion of the small molecule fuels. The catalytic core-shell NPs were synthesized by using the catalytic NPs (before the swelling in of the Cu) as the seeds for a subsequent precipitation polymerization with NIPAAm.[156] The seeds and the core-shell NPs were characterized by DLS, and exhibited an increase in the diameter by 59 nm indicating successful growth of a pNIPAAm shell. The temperature response of the core-shell NPs with and without Cu complexation were probed by DLS and revealed and LCST of ~ 36 ºC.

Next the reaction rates and heat generation above and below the LCST were probed. At temperatures above the LCST the catalytic core-shell NPs exhibited a temperature increase of ~3 ºC and consumption of 2-azidoethanol in less than 7 min (Figure 3.4e). This result indicated that the reaction proceeded faster at elevated temperatures regardless of the pNIPAAM shell, which can be attributed to the large surface area and small hydrodynamic size of the 2-azidoethanol and N,N-dimethylaminopropyne fuels which allows for facile diffusion to the catalytic site regardless of the degree of swelling in the gel.

3.3.4 Mesoporous silica/polyethylene glycol core-shell nanoparticle approach

Due to the challenge in turning off the catalytic reaction for core-shell pNIPAAm particles, the core-shell system was modified to increase the steric congestion with the hypothesis that the increased congestion would be more effective at turning off the catalytic reaction. For this reason, we turned to comb-type polyethylene glycol (PEG), another well studied LCST polymer.[177]

We chose to use mesoporous silica nanoparticles as the scaffold for attaching the CuNTA catalyst as well as a chain transfer agent (CTA) which will facilitate grafting of comb-type PEG from the surface of the nanoparticles. Azide functionalized particles were used to facilitate functionalization of both NTA and CTA in one step using copper catalyzed click chemistry.[153] A CTA was synthesized with an alkyne handle on the R-group side, termed CTAalkyne, following modified literature protocols (Figure 3.5a).[182] NTA was synthesized with alkyne handle, termed NTAalkyne, according to modified literature protocols (Figure 3.5a).[183] Azide functionalized mesoporous silica nanoparticles were synthesized *via* literature protocol and characterized by elemental analysis which revealed functionalized of 0.97 mmoles N_3/g particles, which is in agreement with literature.[184] The particles were next functionalized in one step using copper catalyzed click chemistry to yield CTA and NTA functionalized particles (Figure 3.5a). It should be noted that small molecule control experiments using 2-azidoethanol as a model substrate were performed to determine conditions to allow for successful functionalization of azide particles. Since the NTAalkyne binds to the Cu catalyst, a stoichiometric amount of Cu must be added to pre-complex the NTA. The IR spectra showed the disappearance of the azide stretch at 2100 cm^{-1} and emergence of carbonyl and trithiocarbonate stretches associate with NTA and CTA, respectively (Figure 3.5c) indicating successful conversion of surface azides. Additionally, the functionalization of the particles was supported by thermogravimetric analysis which revealed a decrease in the inorganic nonvolatile component from 83.5 wt% to 69.8 wt% inorganic material for the azide and CTA/NTA particles, respectively.

Next the comb-type PEG polymer was grafted to the surface of the nanoparticles *via* surface-initiated reversible addition-fragmentation chain-transfer (RAFT) polymerization. Prior to the surface-initiated RAFT, solution phase experiments were performed in the presence of CuNTA to confirm the Cu complex did not influence the radical polymerization. Gel permeation chromatography revealed polydispersity index (PDI) of 1.19 regardless of the CuNTA presence. The solution phase conditions with 5 mol% poly(ethylene glycol) methyl ether methacrylate (OEGMA, Mn=475 g/mole) relative to di(ethylene glycol) methyl ether methacrylate (MEO2MA) were then applied to the CTA/NTA particles to yield core-shell PEG nanoparticles. The polymerization was run to 53% (degree of polymerization 106, M_n = 21.4 kDa) completion as determined by monomer depletion by ^{1}H NMR spectroscopy. The molecular weight of the free polymer in solution was characterized by gel permeation chromatography to reveal a number average molecular weight of 22.6 kDa and PDI of 1.50, which is consistent with the calculated M_n from monomer consumption.

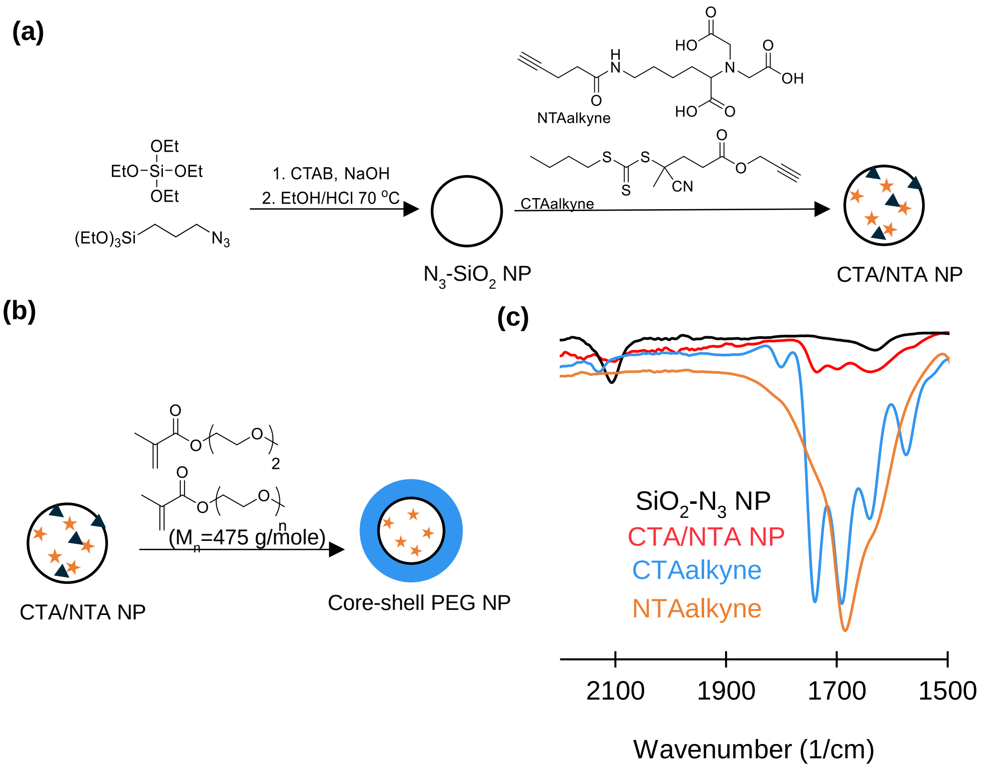

Figure 3.5 Core-shell PEG nanoparticle system. (a) Schematic of synthesis of azide-containing particles (N_3-SiO_2 NP) following literature precedent. [184] Followed by functionalization of the nanoparticles surface *via* copper catalyzed azide alkyne cycloaddition reaction using NTAalkyne and CTAalkyne in a 1:1 molar ratio to yield CTA/NTA NP. (b) Schematic of the functionalization of the CTA/NTA NP with 5 mol% poly(ethylene glycol) methyl ether methacrylate (OEGMA, Mn=475 g/mole) relative to di(ethylene glycol) methyl ether methacrylate (MEO2MA) *via* surface-initiated RAFT polymerization. (c) Infrared spectroscopy characterization of the N_3-SiO_2 NP (black), CTA/NTA NP (red), CTAalkyne (blue), and NTAalkyne (orange).

The resulting particles yielded a cloudy, unstable colloidal solution at room temperature in water. The turbidity decreased with decreasing temperature, which is consistent with an LCST transition. Characterization of colloidal size *via* light scattering revealed an increase in particle size with increasing temperature. This observation was attributed to aggregation of the particles above the LCST due to the hydrophobic interactions, indicating a depression of the LCST (from 35 ºC for linear polymers of the same chemical composition).[177] Changes in the LCST of PEG polymers has been observed for various nanoparticles grafted LCST polymers; however, is still not well understood.[185–187] It should be noted that the grafting of the PEG was also supported by thermogravimetric analysis which revealed an increase in volatile organic content from 26.7 to 96.0 wt%. This supports the claim that the stability of the nanoparticles is due to the PEGylation.

3.4 Conclusion

Here we outlined efforts towards achieving chemically driven self-regulatory behavior in 3-dimensions. We describe the design, synthesis, and characterization of novel catalytic hydrogels. The potential of these hydrogels to achieve self-regulatory behavior was probed *via* determination of relative reactions rates and testing the ability to achieve temperature regulation. Macroscopic catalytic hydrogels did not lead to sufficient heat generation, which is necessary for self-regulatory behavior . This was attributed to poor mass diffusion to active catalytic sites. Catalytic microgels were tested to address the challenge of mass diffusion; however, upon probing of reaction rates it was found that the increased surface area of microgels resulted in the inability to shut off catalysis at elevated temperatures. This prompted investigation of core-shell microgels which yielded similar results. The approach of relying solely on the change in diffusion of a small molecule into a hydrogel network has proved to be insufficient for achieving self-regulating behavior ; however, it is unclear if the increased steric congestion of the comb-type PEG polymers could address this.

The aggregation of the core-shell PEG particles could be used as an advantage in efforts to achieve a self-regulating system. LCST induced aggregation allows for phase-transfer of the particles from water into toluene at temperature above the LCST, which could serve as a new strategy for shutting off catalysis.[188] If the fuel for the reaction remains in the aqueous layer, at temperature below the LCST the catalytic particles will be in the water layer and catalytic reaction will proceed and generate heat. The generated heat is expected to cause LCST phase transition which will result in phase transfer of the particles out of the fuel rich aqueous layer. If successful the catalytic particles will remain in the toluene layer, unable to catalyze the click reaction until the temperature drops below the LCST and the particle return to the fuel rich aqueous layer. This approach has increase potential to shut off catalysis because it separates the catalyst from the fuel *via* an immiscible liquid rather than solely relying on changes in diffusion as a result of decreased mesh size above the LCST.

3.5 Experimental

General experimental details

All commercial reagents were used as received and stirred with a magnetic stir bar unless otherwise noted. 3-dimethylaminopropyne, 2-bromoethanol, *N,N'*-methylenebisacrylamide (MBAAm), tripropargylamine were all purchased from Acros Organics. 3-bromopropanol was purchased from Oakwood Chemicals. $Cu(OAc)_2 \bullet H_2O$ was purchased from Alfa Aesar Chemicals. All other chemicals were purchased from Sigma Aldrich. *N*-isopropylacrylamide (NIPAAm) was recrystallized from hexanes prior to use. Dimethylsulfoxide (DMSO) was dried over activated molecular sieves (3 Å). All yields refer to isolated yields. Nuclear magnetic resonances (NMR) spectra were recorded at 500 MHz CRYO-500 spectrometers at 298 K. ^{1}H NMR chemical shifts are reported as δ values in ppm relative to residual solvent: $CDCl_3$ (δ=7.26 ppm) or DMSO-*d6* (δ=2.50 ppm). ^{1}H NMR data are reported as follows: chemical shift (in ppm), multiplicity (s = singlet, d = doublet, t = triplet, q = quartet, br = broad), relative integration in number of protons, and coupling constants in Hz. Multiplets (m) are reported over the range of chemical shift at which they appear. Differential Scanning Calorimetry (DSC) was done on a TA Instruments DSC Q2000 (endotherm down). Samples were loaded into a Tzero aluminum pan and hermetically sealed. Nitrogen was used to purge the furnace at 40 mL/min. The furnace is equilibrated at 30 ^oC followed by a temperature ramp at 10 ^oC/min to 0 ^oC, followed by a 15 min isothermal period, then a temperature ramp of 10 ^oC/min to 50 ^oC. Light scattering experiments were done on a Cary-60

UV/Vis spectrophotometer. Dynamic light scattering (DLS) was done on a Malvern Zetasizer ZS Nano DLS. The refractive index of polyacrylamide of 1.490 was used. The solvent used was MilliQ water and the value for viscosity at 21.0 ºC was 0.9781 cP and a refractive index of 1.330. The Z-average diameter and polydispersity index (PDI) are reported as an average of 3 measurements with 10 scans each taken at 21.0 ºC. The response to temperature was determined using 1 measurement consisting of 10 scans at each temperature from 20.0 – 50.0 ºC at 5 ºC increments with a 15 second equilibration time between different temperatures.

3.5.1 Synthesis of small molecules and polymers

Scheme 3.1 Synthesis of 2-azidoethanol

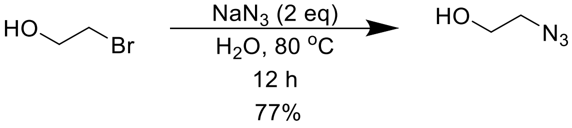

2-azidoethanol was synthesized following the literature reported protocol.[163] It should be noted that lower molecular weight organoazides are explosive and should be handled with caution! Reactions were performed on less than 13 g NaN_3 scale and protected with a blast shield. No explosion was encountered. Sodium azide (5.85 g, 90 mmoles, 2 equiv.) was carefully weighed using a glass pipet into a plastic weight boat and transferred using water (54 mL) into a round bottom flask equipped with a stir bar. 2-Bromoethanol (3.19 mL, 5.62 g, 45 mmole, 1 equiv.) was added and the reaction flask was placed in an oil bath at room temperature equipped with a reflux condenser and a blast shield. The oil bath was heated to 80 °C and held at that temperature overnight. The reaction mixture was cooled to room temperature and transferred to a separatory funnel for extraction with diethyl ether (50 mL, x3). The aqueous layer was handled with caution and quenched by adding 7 mL of 20 wt.% sodium nitrite solution per gram of sodium azide (assuming all sodium azide remains). Next, the aqueous layer was acidified *via* the slow addition of concentrated sulfuric acid until the evolution of brown gas stopped. The combined organic layers were dried over $MgSO_4$ and concentrated under reduced pressure to yield 2-azidoethanol (77% yield). ^1H NMR spectral data agrees with literature reports.[163] ^1H NMR (500 MHz, $CDCl_3$, 298 K) δ 3.85 (dd, 1H, *J* = 10.2, 5.7 Hz), 3.53 – 3.50 (m, 1H), 1.89 (t, 1H, *J* = 5.8 Hz).

Scheme 3.2 Synthesis of 3-azidopropanol

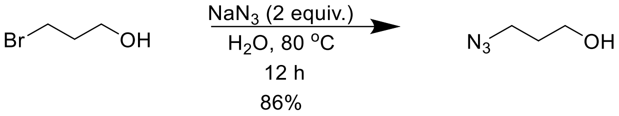

3-azidopropanol was synthesized following the literature reported protocol.[154] It should be noted that lower molecular weight organoazides are explosive and should be handled with caution! Reactions were performed on less than 20 g NaN_3 scale and protected with a blast shield. No explosion was encountered. Sodium azide (18.7 g, 0.228 moles, 2 equiv.) was carefully weighed using a glass pipet into a plastic weight boat and transferred using water (150 mL) into a round bottom flask equipped with a stir bar. 3-bromopropanol (20.0 g, 0.144 mmole, 1 equiv.) was added and the reaction flask was placed in a room temperature oil bath equipped with a reflux condenser and a blast shield. The oil bath was heated to 50 °C and kept at that temperature overnight. The reaction mixture was cooled and transferred to a separatory funnel for extraction with diethyl ether (150 mL, x3). The aqueous layer was handled with caution and quenched using the same protocol described above. The combined organic layers were dried over $MgSO_4$ and concentrated under reduced pressure. Next, the product was distilled under vacuum to yield 3-azidopropanol (86% yield). ^1H NMR spectral data agrees with literature.[154] ^1H NMR (500 MHz, $CDCl_3$, 298 K) δ 3.76 (dd, 1H, *J* = 11.2, 5.9 Hz), 3.45 (t, 1H, *J* = 6.6 Hz), 1.88 – 1.80 (m, 2H), 1.55 (s, 1H).

Scheme 3.3 Synthesis Tris(3-hydroxypropyltriazolylmethyl)amine (THPTA)

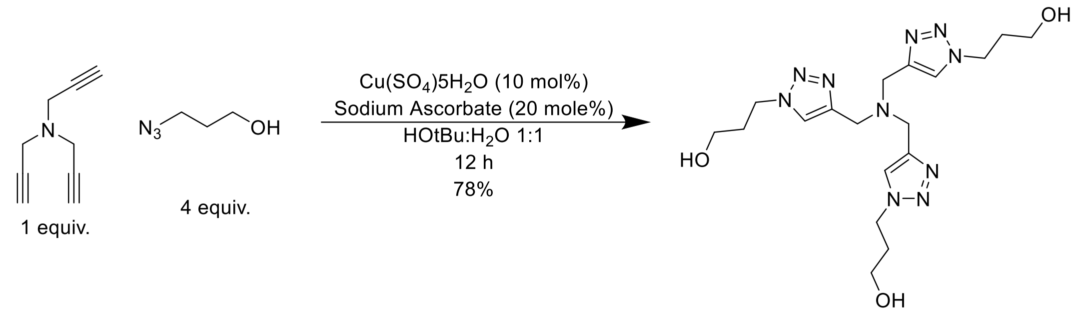

Tris(3-hydroxypropyltriazolylmethyl)amine (THPTA) was synthesized following the literature reported protocol.[154] Tripropargylamine (0.393 g, 3 mmoles, 1 equiv.), and 3-azidopropanol (1.211 g, 12 mmoles, 4 equiv.) were added to a round bottom flask equipped with a stir bar and dissolved with 1:1 tert-butanol:water (6 mL). To this was added $CuSO_4$●$5H_2O$ (74.9 mg, 0.3 mmoles, 0.1 equiv.), and *L*-sodium ascorbate (119 mg, 0.6 mmoles, 0.2 equiv.). The reaction flask warmed slightly due to heat generation. The reaction was stirred at room temperature overnight. Saturated disodium ethylenediaminetetraacetate dihydrate (20.0 mL) was added to the reaction mixture then transferred to a separatory funnel and washed with dichloromethane (15 mL, x3). The aqueous layer was concentrated under reduced pressure to yield a bluish-green solid. The solid was dissolved with minimal amount 80:20 dichloromethane:methanol (~8 mL) and loaded on a plug of neutral alumina. The product was eluted with 80:20 dichloromethane:methanol (~200 mL). The product was concentrated under reduced pressure to yield a yellow oil. The oil was diluted with 80:20 dichloromethane:methanol (4 mL) and precipitated into diethyl ether (250 mL). The resulting cloudy solution was refrigerated overnight, filtered and dried under vacuum at 40 ºC overnight to yield THPTA as an off-white solid (78% yield). ^1H NMR spectral data agrees with literature.[154] ^1H NMR (500 MHz, DMSO, 298 K) δ 8.03 (s, 1H), 4.65 (t, 1H, *J* = 5.0 Hz), 4.41 (t, 2H, *J* = 7.1 Hz), 3.62 (s, 2H), 3.40 (dd, 2 H, *J* = 11.3, 5.9 Hz), 2.06 – 1.88 (m, 2H, *J* = 6.5 Hz).

Scheme 3.4 Synthesis of THPTAmon

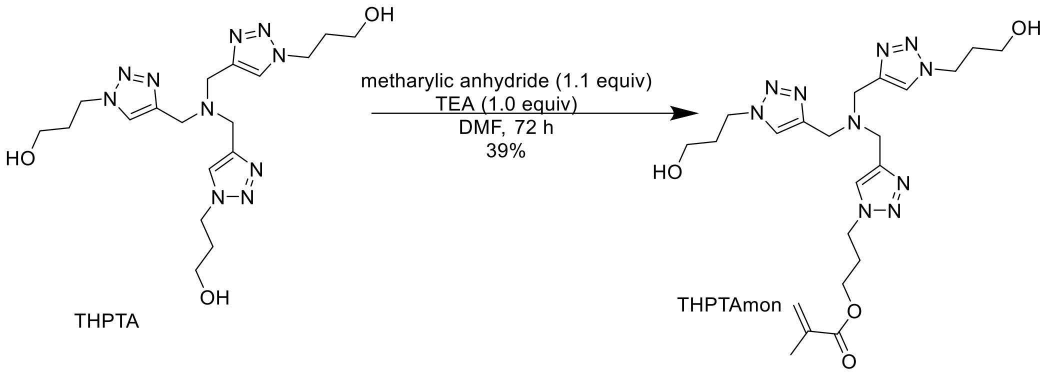

Tris(3-hydroxypropyltriazolylmethyl)amine (2.16 g, 1 equiv, 4.82 mmoles) was added to a flame dried round bottom flask under nitrogen protection, equipped with a stir bar and dissolved with anhydrous DMF (107 mL) and triethylamine (TEA, 0.67 mL, 1 equiv., 4.82 mmoles). Methacrylic anhydride (0.79 mL, 1.1 equiv., 5.31 mmoles) was added via syringe pump (7 uL/min). The reaction was stirred at room temperature for 48 h. 4-methoxyphenol was added as a radical inhibitor and crude reaction mixture was concentrated *in vacuo* and purified by column chromatography with DCM 5% NH_4OH in methanol to yield THPTAmon as yellow oil (39% yield). 1H NMR (500 MHz, DMSO, 298 K) δ 8.07 (s, 1H), 8.02 (s, 2H), 6.01 (s, 1H), 5.66 (s, 1H), 4.65 (m, 2H), 4.47 (s, 2H), 4.41 (t, 4H, J = 7.1 Hz), 4.07-4.09 (m, 6H), 3.60-3.64 (s, 6H), 3.37-3.41 (m, 4H), 2.25 – 2.15 (m, 2H), 2.01 – 1.92 (m, 4H), 1.86 (s, 3H).

Scheme 3.5 Synthesis of 2,2'-((5-amino-1-carboxypentyl)azanediyl)diacetic acid (N6-NTA)

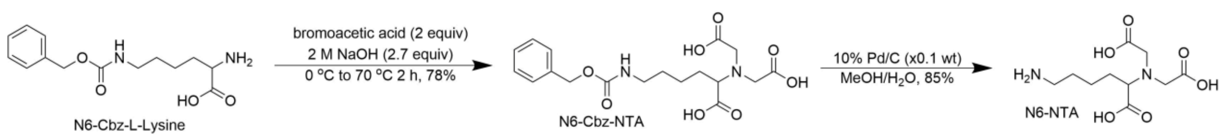

2,2'-((5-amino-1-carboxypentyl)azanediyl)diacetic acid (N6-NTA) was synthesized following literature precedent.[189] N6-((benzyloxy)carbonyl)lysine (N6-Cbz-L-Lysine) (3.36 g, 1 equiv.,12 mmoles) was dissolved in 2 M NaOH (16 mL) and added dropwise to a stirred solution of bromoacetic acid (3.33 g, 2 equiv., 24 mmoles) in 2 M NaOH (18 mL) cooled in an ice bath. The solution was slowly warmed to room temperature over 12 h, and heated to 70 ºC for 2 h. The crude reaction mixture was cooled to room temperature and acidified with 1 M HCl to pH 2 to precipitate the crude product. To isolate disubstituted product, the crude precipitate was dissolved with 1 M NaOH and precipitated using 1 M HCl. Precipitate was filtered and dried under vacuum at 40 ºC to yield N6-Cbz-NTA as a white solid in 78% yield. N6-Cbz-NTA (3.00 g, 7.57 mmoles) is dissolved in 16:1 MeOH:H_2O (50 mL). 10% Pd/C (0.1 wt, 0.30 g) was added and the reaction was stirred under H_2 for 18 h. Crude reaction mixture was filtered over a plug of celite and concentrated *in vacuo* to yield product in 85% yield. 1H NMR spectral data agrees with literature.[189] 1H NMR (500 MHz, D_2O) δ 4.01 – 3.86 (m, 5H), 3.06 (t, J = 7.3 Hz, 2H), 2.09 – 1.86 (m, 2H), 1.82 – 1.72 (m, 2H), 1.72 – 1.49 (m, 2H).

Scheme 3.6 Synthesis of 2,2'-((5-acrylamido-1-carboxypentyl)azanediyl)diacetic acid (NTAmon)

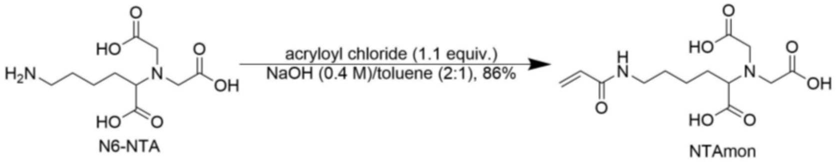

2,2'-((5-acrylamido-1-carboxypentyl)azanediyl)diacetic acid (NTAmon) was synthesized using literature precedent with minor modifications.[183] N6-NTA (0.52 g, 1 equiv., 2 mmoles) was dissolved in 0.4 M NaOH (17 mL). Acryloyl chloride (0.18 mL, 1.1 equiv., 2.2 mmoles) was diluted with anhydrous toluene (9 mL) and added dropwise to the stirred solution of N6-NTA. Reaction flask was stirred overnight, toluene was removed *in vacuo* at 25 ºC. Remaining aqueous solution was acidified to pH 2 with 1 M HCl, then lyophilized. EtOH was added to the white solid, and undissolved precipitate was filtered off. EtOH solution was concentrated *in vacuo* to yield

NTAmon as a viscous oil in 86% yield. 1H NMR (500 MHz, D_2O) δ 6.34 – 6.12 (m, 2H), 5.78 (d, J = 10.0 Hz, 1H), 4.37 – 4.14 (m, 5H), 3.39 – 3.26 (m, 2H), 2.14 – 1.90 (m, 2H), 1.73 – 1.47 (m, 4H).

Scheme 3.7 Synthesis of 2,2'-((1-carboxy-5-(pent-4-ynamido)pentyl)azanediyl)diacetic acid (NTAalkyne)

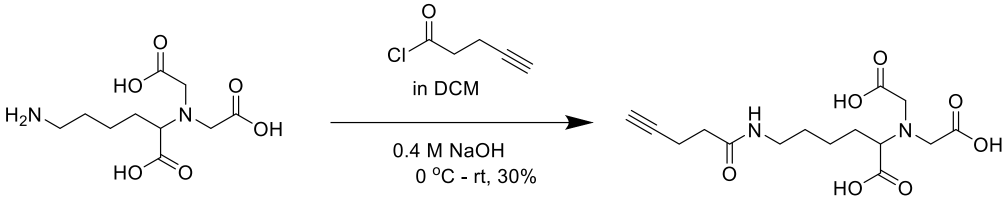

Synthesis of NTA-containing nanoparticle (catalytic NPs)

NIPAAm nanoparticles (NP) were synthesized following the literature reported protocol.[156,157] NIPAAm was recrystallized from hexanes and stored in refrigerator until ready to use. To a flask equipped with a stir bar, NIPAAm (61.1 mg, 0.541 mmoles) and NTAmon (9.0 mg, 0.0284 mmoles) were added and dissolved with MilliQ water (3.52 mL). Stock solutions of *N,N'*-methylenebis(acylamide) (10 mg/mL), sodium dodecyl sulfate (5 mg/mL), and potassium persulfate (10 mg/mL) were prepared fresh using MilliQ water. *N,N'*-methylenebis(acylamide) (0.63 mL stock solution, 6.3 mg, 0.0409 mmoles) was added to the monomer solution and the solution was sparged with nitrogen gas for 15 minutes before the addition of sodium dodecyl sulfate (0.36 mL stock solution, 1.8 mg, 0.00624 mmoles). The monomer solution was sparged for an additional 5 minutes then immersed in an oil bath at 70 ºC for 10 minutes. A sparged solution of potassium persulfate (0.5 mL stock solution, 5 mg, 0.0185 mmole) was added and the vessel was kept at 70 ºC for 3 h. The solution became turbid within 30 minutes. After 3 h the solution was exposed to air, cooled and transferred to a dialysis bag (molecular weight cut-off 12,000 g/mol). The nanoparticles were dialyzed against water for 3 days changing the water twice a day. To complex, $Cu(II)(OAc)_2$●H_2O (3.2 mg, 0.031 mmoles) was added and the solution was stirred for 12 h prior to removal of unbound Cu(II) by dialysis with molecular weight cut-off 12,000 g/mol. Nanoparticle size was determined using DLS. Z-averaged NP diameter of 15 scans is reported to be 616 nm at 20 ºC and 223 nm at 45 ºC, respectively.

Synthesis of catalytic core-shell NPs

The core NP were synthesized as described above for the catalytic nanoparticles (with the exception that Cu(II) was not complexed) and used as seeds for a subsequent seeded precipitation polymerization to yield the catalytic core-shell NPs following literature precedent.[190] The seed NP solution (300 mg, 5.79 mL) was diluted with water (35 mL) and sparged with nitrogen for 1 h. Separately, NIPAAm (0.38 g), N,N'-methylenebis(acylamide) (27.7 mg, 5 mol% relative to NIPAAm), sodium dodecyl sulfate (15.5 mg, 0.29 mg/mL), and ammonium persulfate (18.8 mg, 2.3 mol% relative to monomer) were dissolved in water (8.1 ml) and sparged with nitrogen for 30 min. The seed solution was placed in an oil bath at 70 ºC for 15 minutes prior to the dropwise addition of the shell precursor solution into the stirred solution of seeds. After 3 hours the solution was exposed to air, cooled and transferred to a dialysis bag (molecular weight cut-off 12,000 g/mol). The core-shell NPs were dialyzed against water for 3 days changing the water twice a day. To complex, $Cu(II)(OAc)_2$●H2O (22.2 mg, 0.11 mmoles) was added and the solution was stirred for 12 h prior to removal of unbound Cu(II) by dialysis with molecular weight cut-off 12,000 g/mol. Nanoparticle size was determined using DLS.

Synthesis of NTA/CTA nanoparticles

Azide functionalized mesoporous silica nanoparticles can be synthesized *via* literature protocol and characterized by elemental analysis which revealed functionalized of 0.97 mmoles N_3/g particles, which is slightly lower that the reported literature (1.57 mmoles N_3/g).[184] The Z-average diameter of the azide particle were also characterized by dynamic light scattering to be 178 nm with a PDI of 0.192, which is also in agreement with literature (159 nm by DLS, 50-70 nm by transmission electron microscopy.[184] The Barrett, Joyner and Halenda (BJH) pore diameter reported in literature indicates a 2.4 nm pore size and a (BET) surface area of 800 m^2/g, as determined by N_2-adsorption–desorption isotherms.[184] To functionalize the azide particles with a CTA and NTA derivatives with alkyne handle copper catalyzed click chemistry was used. The conditions were optimized using using 2-azidoethanol as a model substrate to determine optical conditions to allow for successful functionalization. The small molecule conditions that yielded successful conversion were 250 mM azidoethanol, 750 mM triethylamine, 50 mM sodium ascorbate, and 250 mM Cu(II) acetate in 20% dimethylsulfoxide in water to aid in solubility. These conditions were then applied to the azide particles using a 1:1 molar ratio of CTAalkyne:NTAalkyne. Particles were purified *via* washing with water:dimethylsulfoxide (1:1) and centrifugation (5,000 RCF, 20 min, x6).

Synthesis of PEG grafted nanoparticles

Solution phase RAFT polymerization was performed with and without the presence of CuNTA with CTAalkyne:monomer: azobisisobutyronitrile (AIBN) of (1:80:0.25) with a monomer feed ratio of 5 mol% poly(ethylene glycol) methyl ether methacrylate (OEGMA, M_n=475 g/mole) relative to di(ethylene glycol) methyl ether methacrylate (MEO_2MA) in 1,4-dioxanes (0.5 M monomer). The reaction was heated at 70 °C and run to 92% and 85% conversion as determined by monomer depletion by ^{1}H NMR spectroscopy without and with the presence of Cu(II)NTA salts (1 equiv. Cu and 1.1 equiv. NTA), respectively. The polymers were characterized by gel permeation chromatography (GPC) using PEG standards and both had a polydispersity index (PDI) of 1.19. These conditions were applied to the CTA/NTA particles using CTA/NTA particles:monomer:AIBN (1:200:0.25) with the same monomer feed ratio. The mmoles of CTA was estimated using azide content as determined by elemental analysis, and the click reaction was assumed to go to 80% conversion. The polymerization was run to 53% conversion (degree of polymerization = 106, M_n= 21.4 kDa) as determined by monomer depletion by 1H NMR spectroscopy. The free polymer in solution was characterized by GPC (M_n=22.6 kDa PDI 1.50). The particles were purified *via* dialysis and characterized by dynamic light scattering (DLS), nanoparticle tracking analysis NanoSight NS300, and thermogravimetric analysis (TGA) TA Q500. DLS indicated unstable nanoparticle solution with an observed increase in size with increased temperature (10 to 25 ⁰C). Due to the unreliable size characterization of the DLS, the particles were characterized by NanoSight NS3000, which showed that observed size increase is due to nanoparticle aggregation. TGA revealed a substantial increase in volatile mass from 26.7 to 96.0 wt% indicating successful grafting of polymer from the surface of the particles.

Synthesis of macroscopic temperature-responsive THPTA-containing pNIPAAm hydrogels

pNIPAAm hydrogels were synthesized following the literature reported protocol.[158] NIPAAm (100 mg, 0.884 mmoles), *N,N'*-methylenebis(acylamide) (5 mg, 0.032 mmoles, 3.6 mol% crosslinking relative to NIPAAm), and THPTAmon (0-50 mol % relative to NIPAAm keeping crosslinking density of NIPAAm+THPTAmon relative to MBAAm at 3.6 mol%) were dissolved with dry DMSO (0.9 mL) and sparged with nitrogen for 10 minutes. A freshly prepared stock solution of ammonium persulfate (20 mg/mL in DMSO) was sparged with nitrogen for 10 minutes. Ammonium persulfate (0.1 mL of the stock, 2 mg, 0.009 mmoles) was added to the monomer and crosslinker solution, followed by *N, N, N', N'*-tetramethylethylenediamine (TEMED, 20 uL, 0.133 mmoles). The reaction flask was immediately placed in a refrigerator at 0 ºC for 3 days. The gel was removed from the test tube using a spatula and addition of water to hydrate the gel. To remove residual monomer the gel placed in 1 L of water and the water was replaced twice a day for 3 days.

3.5.2 Characterization of temperature responsive polymers

The swelling and deswelling properties of the hydrogels (~0.5 g scale) were probed gravimetrically. The weight percent (wt%) of the gels were normalized to the initial weight of the gel at room temperature. The gel was then transferred to a 40 ºC water bath for 2 minutes before the mass was recorded. The gel was then transferred to a 20 ºC water bath for 2 minutes before the mass was recorded again. This cycle was repeated four times to demonstrate the reversible, rapid and large LCST transition, shown in Figure 3.1a, which is attributed to the cryogenic polymerization conditions which have been reported to produce a macroporous structure.[158]

Investigation of swelling and deswelling of pNIPAAm nanoparticle hydrogels

Table 3.1 DLS characterization of catalytic 5 mol% NTA-co-NIPPAm NP size at pH 7.

	T (ºC)	**Z-avg (nm)**	**PDI**
No Cu	20	364	0.055
	40	171	0.045
Cu	20	403	0.089
	40	305	0.060

Table 3.2 DLS characterization of core-shell NP before Cu(II) complexation size at pH 2.

Particles	T (ºC)	Z-avg (nm)	PDI
Seeds	20	327	0.086
	25	292	0.038
	30	241	0.002
Core-shell	20	386	0.112
	25	380	0.093
	30	312	0.002

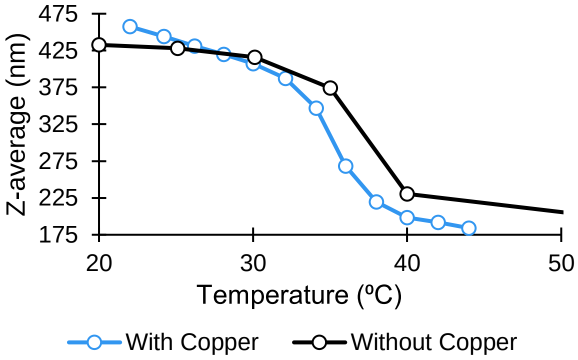

Figure 3.5 DLS characterization of core-shell NP size at pH 7.

3.5.3 NMR spectra

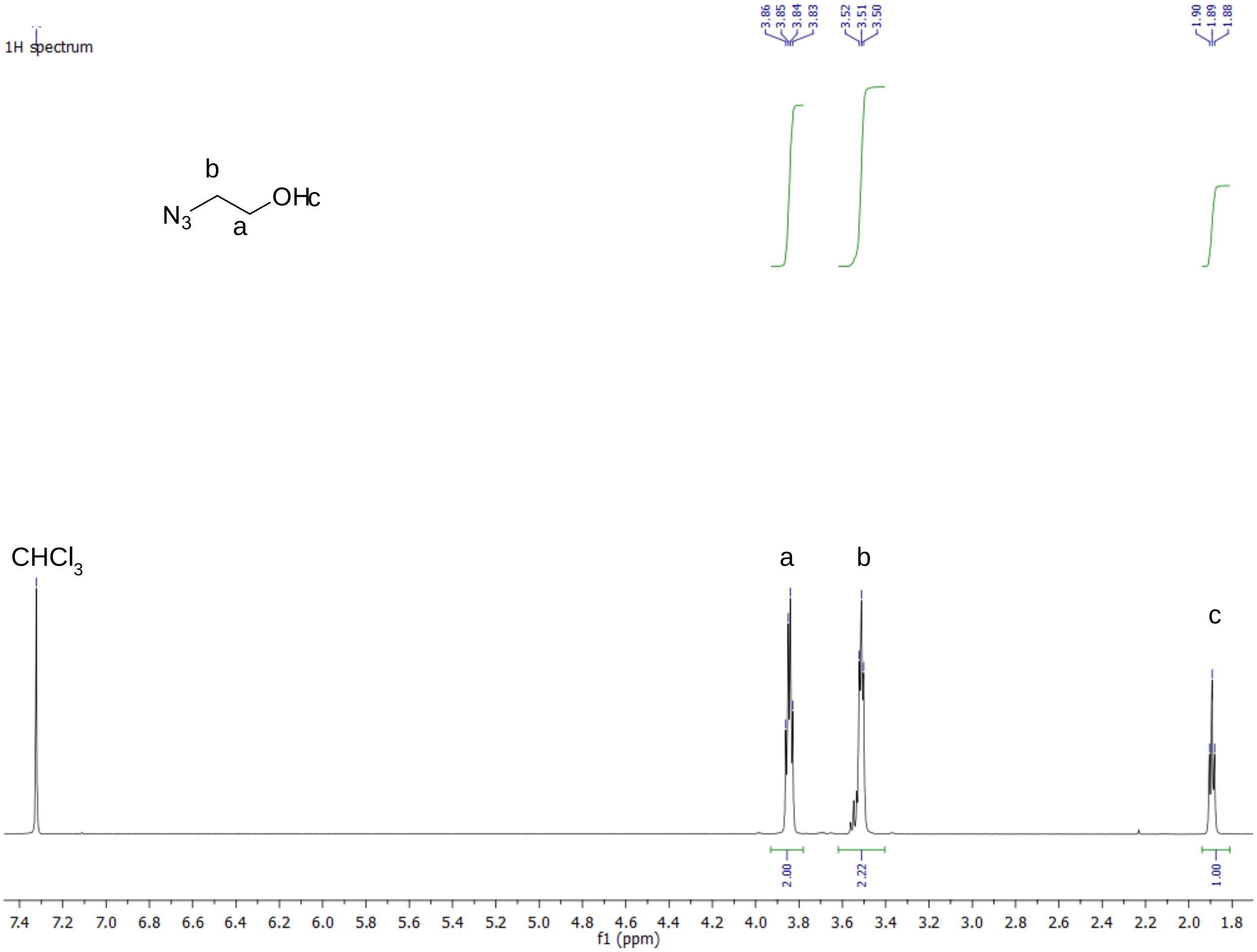

Figure 3.6 ^{1}H NMR spectrum of 2-azidoethanol in $CDCl_3$.

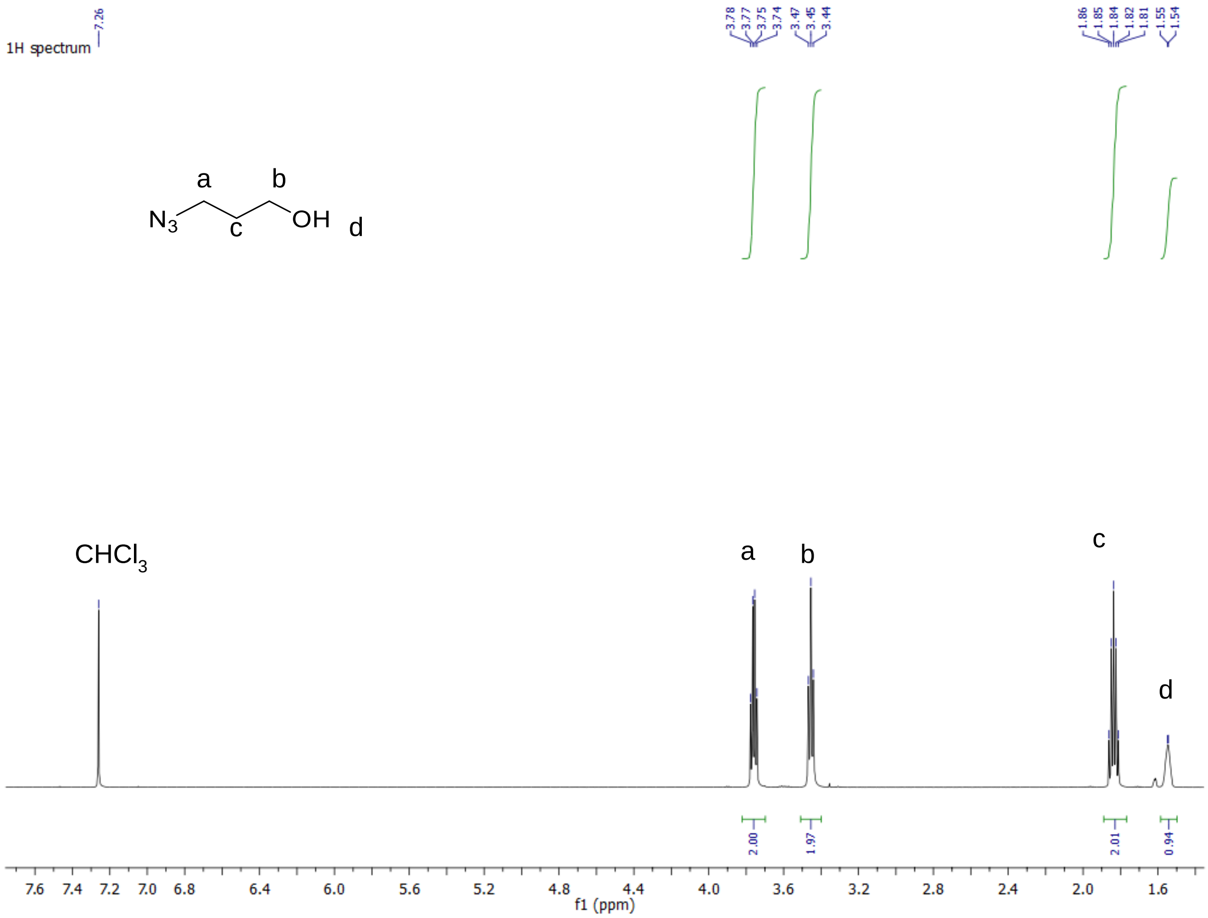

Figure 3.7 ^{1}H NMR spectrum of 3-azidopropanol in $CDCl_3$.

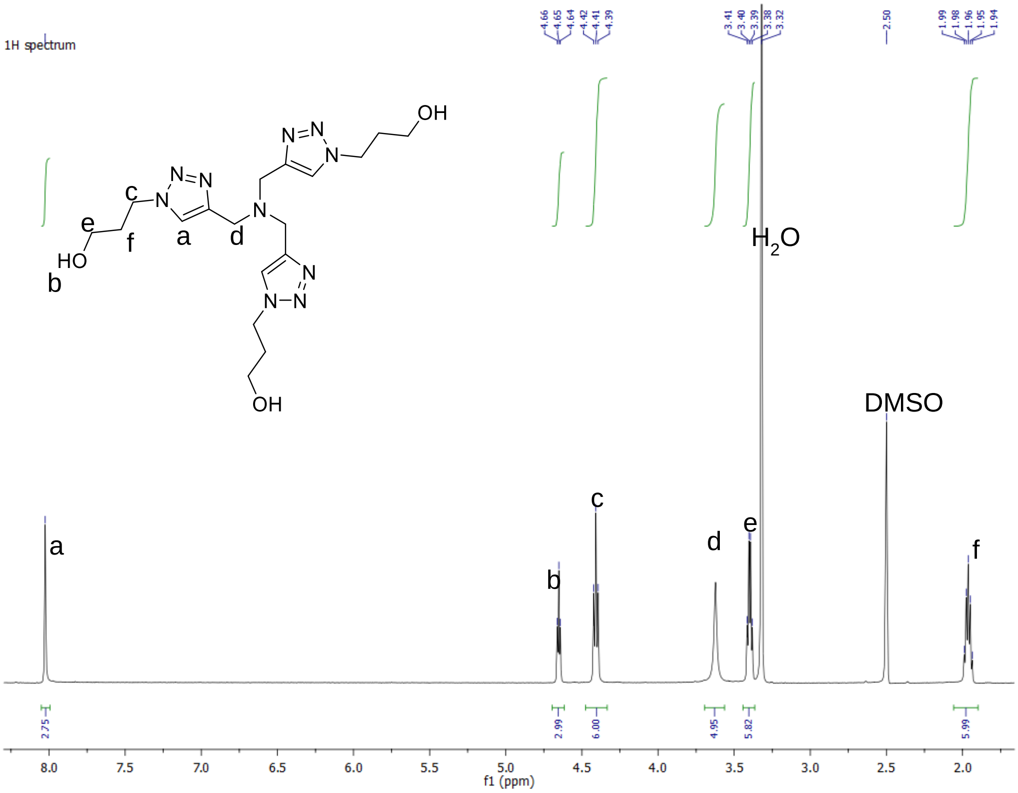

Figure 3.8 ^{1}H NMR spectrum of THPTA in d_6-DMSO.

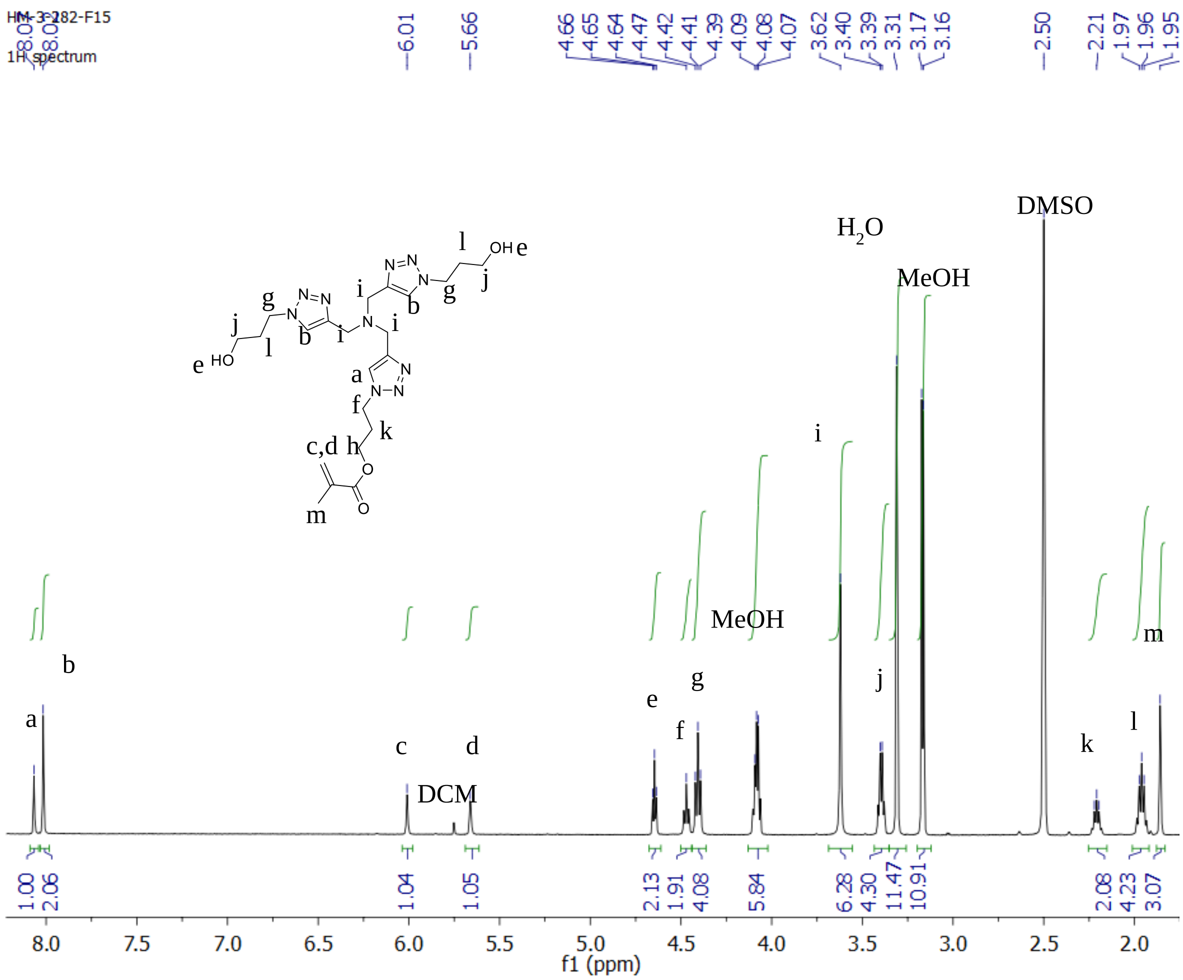

Figure 3.9 ^{1}H NMR spectrum of THPTAmon in d_6-DMSO.

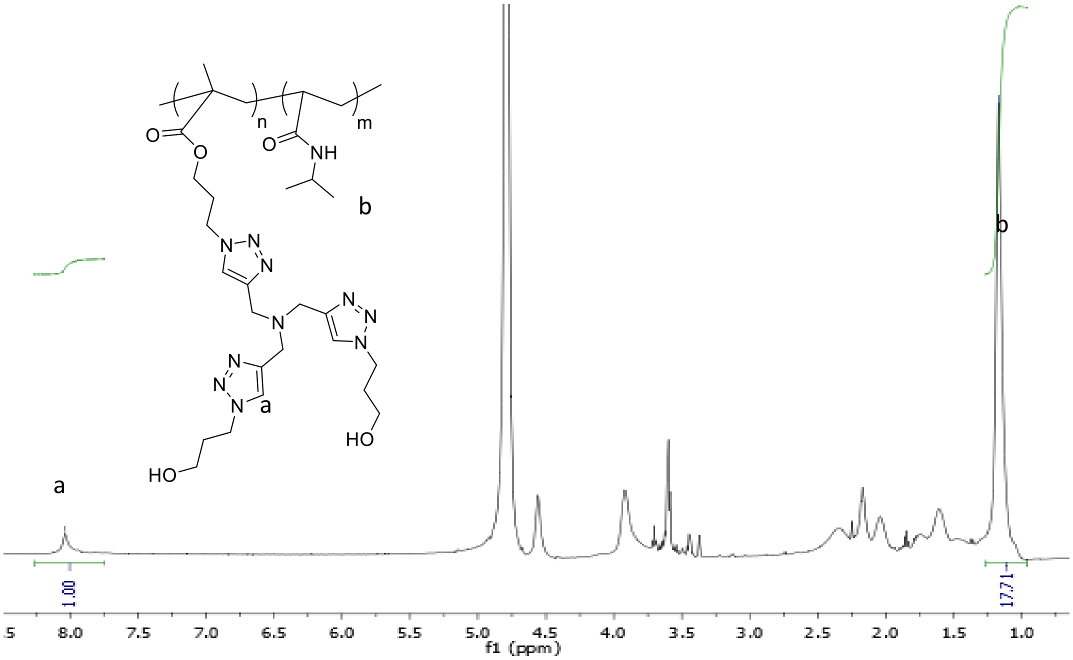

Figure 3.10 ^{1}H NMR spectrum of p-THPTA-co-NIPAAm polymer in d_6-DMSO. Polymer was synthesized with 3.4 mol% THPTAmon feed ratio relative to NIPAAm which resulted in 10.1% incorporation of THPTAmon relative to NIPAAm in the final copolymer which agrees with reactivity ratios in literature for methacryate and acrylamide-based monomers.[180]

Chapter 4: Self-healing Magnetic Nanocomposites

4.1 Introduction to self-healing materials

As the life cycle of a materials comes to an end, the material usually experiences crack propagation that leads to the ultimate mechanical failure. Extending the functional life cycle of materials is typically accomplished by engineering more mechanically robust materials; however, an alternative approach that inspired by nature has emerged as an alternative method. Self-healing is a ubiquitous process in biological systems that allows for repairing of damage. To draw on a specific example in biology let us consider healing in mammals. When we incur damage, the first mode of response for the body is to minimize blood loss. This is followed by removal of damaged cells *via* phagocytosis and replacement with new healthy cells. Lastly, the newly grown tissue is remodeled via removal of extraneous cells. While biological systems use multistep complex self-healing mechanisms, synthetic mimics aim to draw inspiration from the fundamental lesson of creating longer lived materials by imparting them with the ability to self-heal. Self-healing materials can be broadly classified into two approaches: extrinsic and intrinsic self-healing.

Extrinsically self-healing materials rely on embedded capsules that rupture and release healing agents to fix mechanical damage. Commonly, this is achieved by embedding a capsule filled with monomer into a hard material that contains a catalyst for polymerization. Upon mechanical damage to the material, the capsules rupture, releasing liquid monomer that is then polymerized via the dispersed catalyst to fill the site at which damage occurred. In one notable example, White *et al.* demonstrated the use of Grubbs' catalyst in ring-opening metathesis polymerization to achieve capsule based healing.[191] By incorporating of dicyclopentadiene monomer into 50-20 µm size capsules using standard microencapsulation techniques the monomer is protected from premature polymerization during material processing. To facilitate polymerization Grubb' catalyst is dispersed throughout the epoxy-based material. Upon generation of cracks through the material, capsules break filling the void with liquid monomer that upon contact with the catalyst filled epoxy will result in polymerization to heal the damage that was incurred. Multi-capsule based systems have also been demonstrated; in one example, the encapsulation of the two components necessary for platinum-catalyzed hydrosilylation, known as Sylgard ® 180.[192] In this work the platinum catalyzed was encapsulated into separate capsules as the vinyl-terminated polydimethylsiloxane (PDMS) precursor to yield curing upon rupture of both capsule in a given area.[192] Capsule based approaches allow for self-healing of mechanically robust materials; however, are limited to one healing cycle per location due to the limited supply of microcapsules. Vascular based approaches can address this challenge by capitalizing on hollow channels filled with reactive healing agents that can be replenished.[193] Vascular networks are commonly made by direct-ink-writing, which is an extrusion based additive manufacturing method that allows for control over the network topology of the vasculature, but limits identify of the surrounding matrix.[193] Capsule and vascular approach mimic natures use of multicomponent systems to achieve self-healing behavior.

Intrinsic self-healing capitalizes on reversible bonds that can break and reform, which are intrinsic to the polymer itself.[194] As compared to extrinsic methods of self-healing, intrinsic polymers can repair damage at the same location multiple times because there is no reliance on a limited supply of capsules. When damage is incurred in the form of a crack, the two resulting interfaces can be recovered if they are within proximity due to the ability for the reversible dynamic bonds to shuffle and form new bonds across the cut interface. The dynamic functional handles need to find new respective sites to form a new bond. This method of self-healing relies on polymer flow, rather than liquid monomer flows as in extrinsically self-healing methods, which is inherently slower. For this reason, self-healing efficiencies for intrinsic systems are highly dependent on temperature relative to the glass transition temperature (T_g) or melting temperature (T_m) for semi-crystalline materials. Many different motifs including reversible covalent,[195,196] and noncovalent bonds have been implemented to achieve self-healing.[197,198] In a key example, the thermally reversible Diels-Alder reaction was employed to demonstrate intrinsic self-healing.[195] Polymers functionalized with furan and maleimide handles were employed as the diene and dienophile respectively. Upon curing the Diels-Alder reaction proceeds and forms a crosslinked network that exhibits a modulus of 4.72 GPa. The resulting material demonstrated the ability to self-healing at temperatures above 100 ºC.[195] This demonstrate the use of reversible covalent bonds to achieve self-healing behavior . The robust mechanical properties and high temperature needed for healing are quite common for this approach. Noncovalent interactions tend to require lower temperature and are generally weaker materials, with low T_g's. Polymers able to hydrogen bond with one another have been developed to achieve self-healing at lower temperatures.[198] Approaches using multiphasic materials have been made in order to address this issue by using phase-separating polymers.[197] By incorporating the dynamic motif in a soft, lower T_g phase, but still maintaining robust mechanical properties with a higher T_g phase, spontaneous self-healing can be achieved.[197]

4.2 Introduction to self-healing magnetic composites

Polymeric nanocomposites with magnetic nanoparticles (MNPs) have wide applications in stimuli-responsive materials, actuators, and soft robotics. The magnetic properties of such nanocomposites allow for actuation without physical contact by using an external magnetic field.[4] Increasing the actuation potential of these materials is critical for their wide-spread use as remote actuators and is commonly achieved by increasing the fraction of MNPs.[199,200] However, the increased nanoparticle content often results in aggregation of nanoparticles and decreased mechanical performance of these materials.[201,202] Furthermore, using magnetic nanocomposites as actuators in soft robotics requires robust and durable mechanical properties.[203] Repeated motion can build up stress, generating defects that propagate and finally lead to catastrophic mechanical failure.[203,204] This is especially challenging for materials with high fractions of MNPs that are inherently more brittle.[205,206]

One approach to making magnetic actuators with robust mechanical properties is to impart the materials with self-healing ability; self-healing increases the durability and functional lifetime of the material.[204,207] Intrinsically self-healing materials leverage dynamic, reversible interactions that can be accessed repeatedly upon damage to facilitate healing.[193,194,208–210] Such interactions include non-covalent interactions,[197,198,211–214] or dynamic covalent bonds,[195,215–218] that prevent the cascade of the damage and the delay of eventual catastrophic failure of the material.[210]

There have been significant efforts to develop magnetic nanocomposites with self-healing capabilities.[204] A common approach capitalizes on the inductive heating effect of MNPs in an alternating magnetic field.[219–228] The local heat produced from this process allows for various forms of self-healing such as melting of a thermoplastic phase,[219,220,223,227,228] facilitating bond exchange,[225,229–231] or accessing reversible reactions.[221] This method has yielded magnetic composites with good self-healing and mechanical properties; but, not all applications are amendable to applying an alternating magnetic field.

A promising alternative approach relies on the intrinsic self-healing nature of the polymeric matrices of MNP nanocomposites, without relying on the magnetic properties of the MNPs.[232–236] This approach has been demonstrated in hydrogels,[231,232,235–237] and in solid-state bulk materials;[233,238,239,234,231] however, in all these cases there is a non-covalent bond between the MNPs and the self-healing polymer. Due to the inherent attractive nature of MNPs, these approaches are susceptible to nanoparticle aggregations and macroscopic phase separation.[202] More recently, Xu et al.[240] reported a self-healing magnetic nanocomposite using a graft-from approach such that there is a covalent linkage between the dynamic polymer and the MNPs, preventing aggregation. This represents a step forward toward the development of intrinsically self-healing bulk magnetic nanocomposites; however, the synthesis required specially designed monomers, limiting its general applicability and practical applications.

4.3 Our design for self-healing magnetic nanocomposites

Here, we developed a bulk self-healing magnetic nanocomposite using commercially available inexpensive monomers and a graft-from approach to yield stable and homogenous MNP dispersion (Scheme 4.1). The use of commodity monomers is expected to facilitate translation of the material into real world applications. Our goal was to develop intrinsically self-healing magnetic nanocomposites with high actuation potential and good mechanical properties *via* a graft-from approach using readily available monomers that have not yet been investigated for self-healing behavior. We synthesized MNPs with a narrow size distribution, then functionalized the MNPs with a radical chain-transfer agent (CTA) to allow for reversible deactivation radial polymerization from the surface. By using the graft-from approach we were able to achieve high weight percent (wt %) and homogenous dispersion of MNPs.[202] We employed an inexpensive commodity monomer, acrylamide (Am), to introduce the dynamic self-healing motif with its hydrogen-bonding amide group. To maintain polymer chain dynamics for spontaneous healing under ambient conditions, we copolymerized Am with another inexpensive commodity monomer, *n*-butyl acrylate (BA), to yield the copolymer termed BAAm. Mechanical properties and self-healing behavior of the BAAm MNP nanocomposite were thoroughly characterized by mechanical testing. Finally, simple actuation of the magnetic nanocomposite was demonstrated by remote actuation using a commodity external magnet.

Scheme 4.1 Design and synthesis of self-healing magnetic nanocomposites

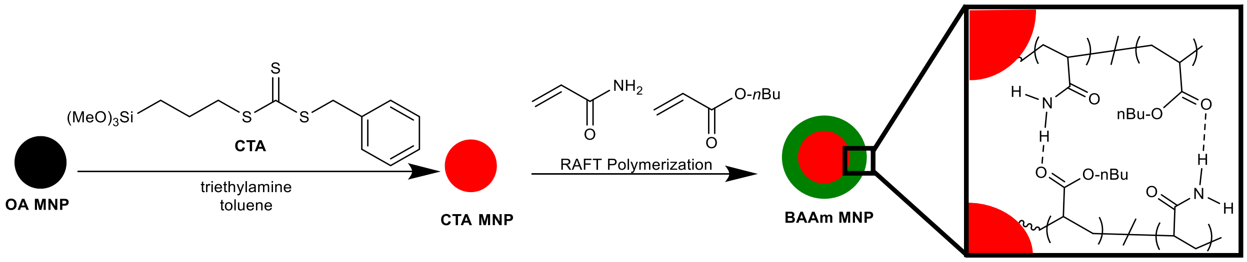

4.4 Results and discussion

4.4.1. Synthesis and characterization of magnetic particles

Specifically, we first synthesized MNPs *via* a two-step thermal decomposition method to yield iron oxide nanoparticles with narrow size distribution.[241] To obtain particles we first generated an iron-oleate precursor that was characterized by differential scanning calorimetry (DSC) (Figure 4.4).[242] In the second step, thermal decomposition of the precursor yielded iron oxide nanoparticles with a diameter of 21.5±1.9 nm as determined by transmission electron microscopy (TEM) (Figure 4.5). The quality of the crystalline nature of iron oxide nanoparticles was evident by the lattice fringes seen in the fast Fourier transform of the high-resolution TEM image (Figure 4.5). We also characterized the surface chemistry of the MNPs *via* attenuated total reflectance (ATR) Fourier transform infrared (FTIR) spectroscopy. The two signals at 1450 and 1375 cm^{-1}, as indicated by red arrows in Figure 4.1b, are characteristic of coordinated asymmetric and symmetric carboxylates stretches, which appear at a lower frequency as compared an unbound carboxylic acid that would display a signal at 1700 cm^{-1}, demonstrating the bond formation between the oleate ligand and the surface of the oleic acid (OA) MNPs.[243,244]

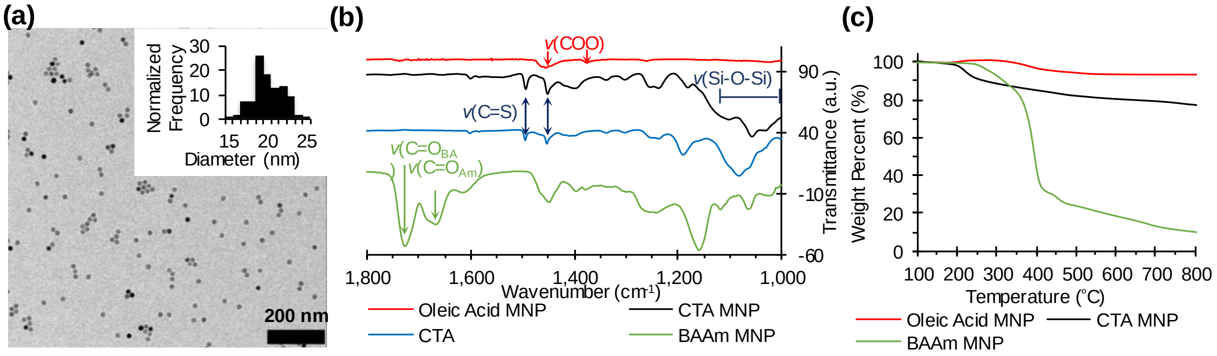

Figure 4.1 MNP Characterization. (a) Transmission electron micrograph of oleic acid MNPs. Inset showing size distribution in terms of normalized frequency with an average diameter of 21.5±1.9 nm. Scale bar is 200 nm. (b) Attenuated total reflectance Fourier transform infrared spectroscopy of oleic acid MNP (red), CTA MNP (black), free CTA (blue), and BAAm-MNP-75 (green) (c) Thermogravimetric analysis of oleic acid MNP (red), CTA MNP (black), and BAAm MNP-75 (green).

Next, the OA MNPs were functionalized with a radical chain-transfer agent (CTA) to facilitate polymerization from the surface. A trimethoxy-containing CTA was synthesized in one step (Scheme 4.2) and characterized by 1H NMR spectroscopy (Figure 4.6).[245] Next the particles were modified with the CTA *via* a base-catalyzed ligand exchange that results in the covalent attachment of the CTA *via* a Fe-O-Si linkages.[246,247] The surface chemistry of the resulting particles, termed CTA MNPs, was characterized *via* ATR FTIR spectroscopy, which revealed the emergence of new vibrational stretches that corresponds to the CTA (Figure 4.1b, full range FTIR spectra in Figure 4.8). The characteristic peaks that confirmed successful ligand exchange include trithiocarbonate stretches from 1450-1490 cm^{-1} marked with blue double headed arrows, and siloxane stretches from 1000-1100 cm^{-1} (Figure 4.1b, blue and black curves).[248–250] Surface functionalization of CTA MNPs was also supported by thermogravimetric analysis (TGA) (Figure 4.1c, red and black curves), which show an increase in volatile organic content from 7 to 25 wt % after functionalization with the CTA indicating successful functionalization (Table 4.1). The increase in organic content upon functionalization with a lower molecular weight ligand is attributed to a higher density of the CTA as compared to the oleate ligand. The higher density of CTA (4.6 mmole/g) is ascribed to the facile base-catalyzed condensation of alkoxysilanes generating multi-layer siloxane shell, commonly seen in literature. [251–253]

The CTA MNPs were then subject to surface-initiated reversible addition-fragmentation chain transfer (si-RAFT) [254–257] polymerization with the comonomers acrylamide (Am) and *n*-butyl acrylate (BA), yielding MNPs grafted with the BAAm copolymer. The feed ratio of Am to BA was chosen to be 30 mole % Am and 70 mole % BA to maintain a relatively high concentration of dynamic hydrogen-bonding motifs while maintaining the sufficient polymer chain dynamics (owing to the lower glass transition temperature of BA).[258] The polymerization was monitored by ^{1}H NMR spectroscopy using mesitylene as an internal standard to ensure percent conversion was less than 50%. A range of composites with varying amounts of polymer were synthesized by quenching the polymerization at different time points. The composites are referred to as BAAm-MNP-XX, where XX is the weight percent of volatile organic components as determined by thermogravimetric analysis including XX = 75, 81, 85, 86 (Table 4.1). After si-RAFT copolymerization the BAAm-MNPs were purified from unreacted monomer *via* precipitation prior to characterization. BAAm-MNP nanocomposites were characterized by TGA, revealing an increase in the organic content from 25 wt % in the CTA-MNPs (Figure 4.1c, black curve) to 75-86 wt %, as seen in Table 4.1, for the range of BAAM-MNP nanocomposites synthesized (TGA characterization of all composites in Figure 4.7). FTIR spectroscopy further supports the functionalization of BAAm copolymer on the surface of the nanoparticles as evident in the signals at 1724 and 1672 cm^{-1}, marked with two green arrows in Figure 4.1b, which are characteristic of carbonyl stretches for BA and Am, respectively (Figure 4.1b, green curve).[250] Due to the graft-from approach, it is possible to achieve large wt % of the inorganic phase while maintaining homogeneity of nanoparticle distribution. This is evident in the TEM characterization of BAAm MNPs that show the nanoparticles to be colloidally stable and well dispersed from one another (Figure 4.2a). Homogenous dispersion of the MNP is attributed to the graft-from approach that results in a covalent linkage between the dynamic polymer and the MNPs, which overcomes the phase separation issue that is common when physically blending incompatible materials.

4.4.2 Mechanical properties of magnetic nanocomposites

Next the mechanical properties of the nanocomposites with varying content of MNPs were characterized by uniaxial mechanical testing (Fig. 2b & Table S1). Stress-strain curves showed clear differences in the mechanical properties that correlate with the relative polymeric content (Fig. 2c). All samples exhibited high extensibility from 540 % for BAAm-MNP-75 to 1200% for BAAm-MNP-86, respectively (Figure 4.2b, black and green curves). There is a clear trend that the extensibility increases with increased weight percent organic content, owing to the increase polymer content (Figure 4.2c). Additionally, the toughness nearly doubles from 28 to 52 MJ/m^3 upon increasing the weight percent from 75 to 86 (Table 4.1). As expected, increasing the fraction of flexible and dissipative polymer chains endows the nanocomposite with higher extensibility and toughness. The reinforcing effects of the MNPs to the nanocomposite mechanical properties can be clearly seen in comparison to a control BAAm polymer without MNP (Figure 4.9). The stress at break increases from 0.8 MPa for the control sample to 6.9 MPa for the BAAm-MNP-75 sample, demonstrating an eight-fold increase, while the extensibility for the BAAm-MNP-75 remains high at 540 % (Table 4.1). The BAAm-MNP-75 sample also exhibits a high Young's modulus of 70 MPa, significantly higher than the control which had a Young's modulus of 12 MPa (Table 4.1). The high modulus and extensibility are both unprecedented for self-healing magnetic composites that self-heal in ambient conditions.

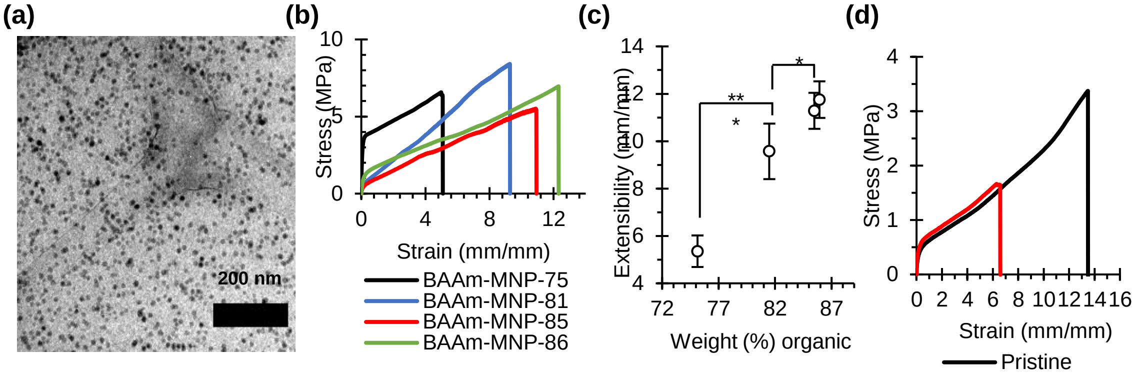

Figure 4.2 Mechanical characterization of BAAm-MNP composites. (a) Transmission electron micrograph of BAAm MNP composite, scale bar 200 nm. (b) Uniaxial mechanical testing strained at 100 mm/min of representative composites. (c) Analysis of extensibility with regards to weight percent organic material. Error bars represent standard deviation from minimum of three samples. (d) Representative stress-strain curves of mechanical testing of BAAm-MNP-75 pristine and healed samples. Healing was carried out for 5 h at 30 ºC (strained at 100 mm/min).

After thorough molecular, mechanical, and morphological characterization, we set to investigate the self-healing behavior of the BAAm-MNP nanocomposites. Polymers with hydrogen bonding capabilities has been previously shown to yield robust self-healing dynamic materials.[197,198] Here, we capitalized on the dynamic hydrogen bonds between the commodity monomers Am and BA, to allow for facile recovery of mechanical properties after incurring damage. The self-healing capabilities are tested by introducing a cut through 50% of the width of a sample, then pressing the cut interfaces together and allowing for healing for desired duration. The self-healing efficiency was quantified by uniaxial mechanical testing in comparison to pristine, uncut sample subject to the same conditions (Figure 4.2d). BAAm-MNP-33 recovered 75% of its original extensibility when healed at 80 ºC for 5 h under reduced pressure (Figure 4.11 and Table 4.5). In more application relevant conditions, the BAAm-MNP-85 sample recovered 41% of the extensibility when healed at ambient conditions of 30 °C for 2 h (Figure 4.10 & Table 4.3). It is expected that the self-healing of composites with lower amounts of polymeric material, such as in BAAm-MNP-33, to be more challenging. For this reason, the healing of BAAm-MNP-33 was extended to 5 h at 30 ºC, after which 46% of the extensibility was recovered (Figure 4.2d & Table 4.3). The observed self-healing efficiency is presumably due to the formation of new hydrogen bonds between BAAm grafts on MNPs at the cut interface (Scheme 4.1c).

4.4.3 Magnetic actuation of nanocomposites

Finally, we demonstrated the potential of using the BAAm-MNP nanocomposites in practical actuation using an external magnetic source. To achieve high magnetic actuation there must be sufficiently high MNP loading. Owing to the graft-from approach, we can incorporate 25 wt % inorganic material in BAAm-MNP-75, which allowed for actuation using a commodity neodymium magnetic with a 54 kg pull force. This was demonstrated by affixing one side of a dog-bone shaped BAAm-MNP-75 sample, while bringing the magnet towards the other end of the sample, as seen in Figure 4.3. The magnet was moved downwards to the sample until actuation started when the magnetic was 2 cm away (Figure 4.3d&e). The nanocomposite was then actuated in the opposite direction by changing the location of the magnet, (Figure 4.3f-h). Upon removal of the magnetic field the composite returned to an equilibrium position (Figure 4.3i). This simple experiment demonstrates that this nanocomposite allows for facile and rapid actuation in addition of self-healing in ambient conditions, making these promising for multifunctional materials for applications as magnetic actuators.

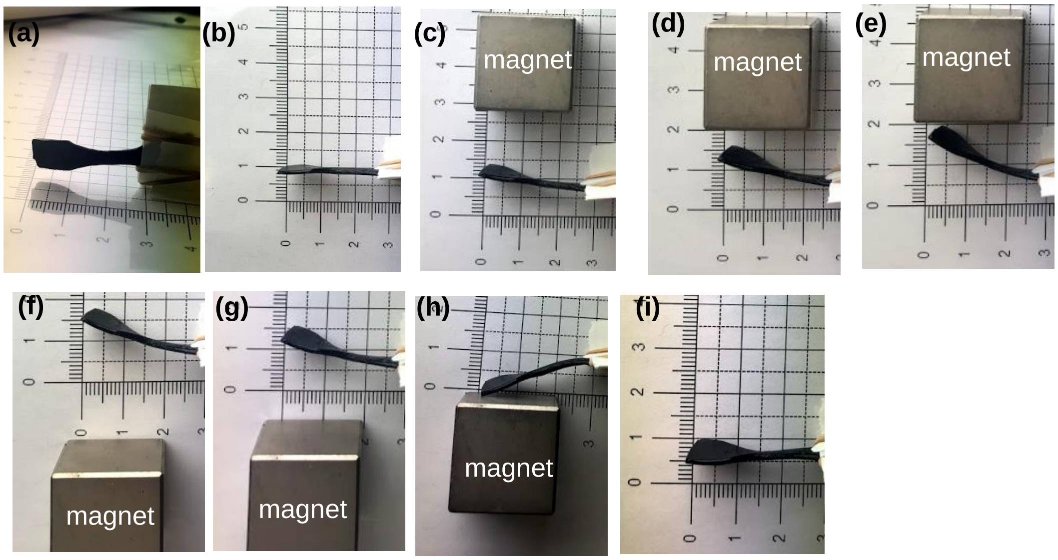

Figure 4.3 Actuation of BAAm-MNP-75 sample using 2.54 cm3 neodymium magnet (54 kg pull force). Grid in background is for measuring distance. A dog-bone sample was affixed in position in (a) a parallel view and (b) perpendicular view. (c) Magnet was placed on the 3 cm mark and (d) moved to the 2 cm mark where actuation starts and (e) finishes in less than 30 seconds. (f) Magnet was placed to the opposite side and (g) moved closer by 0.5 cm (h), then by 1 cm where actuation occurred. (i) Finally, the magnet was removed from area and the sample resumed to its original position**.**

4.5 Conclusion

Here we demonstrated the use of a graft-from polymerization approach to generate MNPs functionalized with an intrinsically self-healing polymer matrix that is composed of readily available inexpensive monomers. The two notable features of this work include the use of inexpensive commodity monomers which is expected to increase translation into practical applications, and the impressive mechanical properties. The magnetic nanocomposite exhibits a high Young's modulus of 70 MPa and excellent extensibility of over 500% while retaining the ability to self-heal in ambient conditions. By using readily available monomers, i.e., acrylamide and *n*-butyl acrylate, the nanocomposite can self-heal mechanical damage with ~ 50% efficiency in as short as 2 hours in ambient conditions. This work contributes to the field of magnetic nanocomposites by using commodity monomers to achieve a self-healing material with excellent mechanical properties and high actuation potential, opening many applications that benefit from robust materials with prolonged lifetimes including such as remote actuation, artificial muscles and soft robotics.

4.6 Experimental

General experimental details

All commercial reagents were used as received and stirred with a magnetic stir bar unless otherwise noted. *n*-Butyl acrylate was passed through a basic alumina column to remove radical inhibitor prior to polymerization. Flash column chromatography was performed with silica gel using an automated column (CombiFlash® Teledyne Isco). Thin-layer chromatography (TLC) was performed on 0.2 mm silica gel-coated glass sheets with F254 indicator. TLC plates were also stained with basic potassium permanganate solution consisting of 1.5 g $KMnO_4$, 10 g K_2CO_3, and 1.3 mL 10 % NaOH in 200 mL water. All yields refer to isolated yields. Nuclear magnetic resonances (NMR) spectra were recorded at 500 MHz CRYO-500 spectrometers. ^1H NMR chemical shifts are reported as δ values in ppm relative to residual solvent: $CDCl_3$ (δ=7.26 ppm). ^1H NMR data are reported as follows: chemical shift (in ppm), multiplicity (s = singlet, d = doublet, t = triplet, q = quartet, br = broad), coupling constants in Hz, and relative integration in number of protons. Multiplets (m) are reported over the range of chemical shift at which they appear. Attenuated total reflection (ATR) Fourier transform infrared (FT-IR) spectra were collected on a Jasco 4700 FTIR equipped with ATR-PRO ONE single bounce ATR with monolithic diamond. Transmission electron microscopy (TEM) images were obtained by a FEI/Philips CM20 200kV LaB_6 with a side-mounted Gatan TEM CCD camera. For TEM imaging 200-mesh carbon grids were used. *J*-KEM Scientific (Model Apollo) was used for PID temperature control for the thermal decomposition of the iron-oleate precursor. Thermogravimetric Analysis (TGA) was conducted on TA Instruments Q500 TGA. Differential Scanning Calorimetry (DSC) was done on a TA Instruments DSC Q2000 (endotherm down, exotherm up). 5 mg of iron-oleate precursor that had been dried at 100 ºC under vacuum overnight was used. Tzero aluminum hermitically sealed pans were used. Reference pan was also an empty Tzero aluminum hermitically sealed. Nitrogen was used to purge the furnace at 50 mL/min. Sample pan and reference pan were equilibrated at 40 ºC, followed by a temperature ramp at 10 ºC/min until 400 ºC. Gel Permeation Chromatography (GPC) traces were obtained on an Agilent 1100 SEC system using a PLGel Mixed-C column from Polymer Labs (Amherst, MA). Dimethylformamide with 1 wt% LiBr was used as eluting solvent at a flow rate of 1.0 mL/min. Number averaged and weight averaged molecular weight distributions (Mn and Mw, respectively) of samples were measured with respect to polystyrene (PS) standards purchased from Aldrich (Milwaukee, WI).

4.6.1 Synthesis of BAAm MNP composites

Synthesis of Oleic Acid MNPs (OA MNPs)

Step 1. A 100 mL round bottom flask equipped with a stir bar and reflux condenser was charged with $FeCl_3{\bullet}H_2O$ (2.70 g, 10.0 mmol), sodium oleate (9.13 g, 30.0 mmol), ethanol (20 mL), water (15 mL), and hexanes (35 mL). The reaction flask refluxed for 4 hours. The reaction was cooled to room temperature, transferred to a separatory funnel, and washed with water (100 mL, x3). The organic layer was concentrated *in vacuo* to yield the red colored iron-oleate precursor. The iron-oleate precursor was dried at 100 °C under vacuum overnight. *Step 2.* A three neck, 100-mL round bottom flask equipped with a Schlenk adapter, reflux condenser, thermocouple, and stir bar were charged with the iron-oleate precursor (6.82 g, 7.58 mmol) and 1-octadecene (48.4 mL). The solution was then deoxygenated by reducing pressure and backfilling with nitrogen (x3) followed by a distillation to remove residual water. Oleic acid (0.80 mL, 2.53 mmol) was then added and heated to 320 °C and kept at this temperature for 1 hour. Particles were purified by precipitation with acetone (4 x 100 mL), dispersing in hexanes in between washes.

Synthesis of CTA

Scheme 4.2 Synthesis of benzyl(3-trimethoxysilylpropyl)trithiocarbonate (CTA)

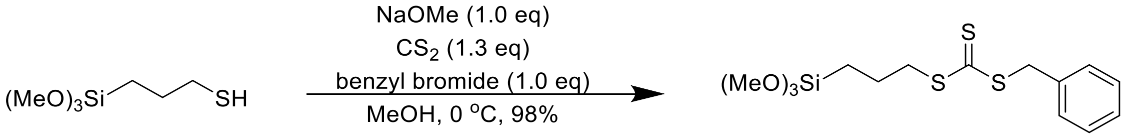

Benzyl(3-trimethoxysilylpropyl)trithiocarbonate (CTA): A 250 mL round bottom flask was charged 3-mercaptopropyltrimethoxysilane (19.6 g, 100 mmol) and anhydrous methanol (30.0 mL) under N_2. The solution was cooled with an ice bath before the dropwise addition of sodium methoxide (18.0 g, 100 mmole, 1.0 equiv.), in a 25% solution in MeOH over 30 min at 0 °C. The solution was stirred at room temperature for an additional 30 minutes before the dropwise addition of carbon disulfide (7.60 g, 100 mmol, 1.0 equiv.) which resulted in a color change from pink to yellow. The reaction was stirred for an additional 5 hours followed by the dropwise addition of benyl bromide (12.6 g, 100 mmol). Reaction was stirred overnight, then concentrated *in vacuo.* The remaining liquid was diluted with dichloromethane, filtered through a glass frit to remove salts, and concentrated *in vacuo.* ^{1}H NMR (500 MHz, $CDCl_3$): δ 7.41-7.32 (m, 5H), 4.67 (s, 2H), 3.63 (s, 8H), 3.46 (t, *J* = 7.4 Hz, 2H), 1.92-1.86 (m, 2H), 0.85-0.81 (m, 2H) which is in agreement with literature reports.[245]

Synthesis of CTA MNPs

Oleic acid functionalized nanoparticles (25 mg) were suspended in toluene (5.0 mL) by ultrasonication for 15 minutes. To the nanoparticle solution, triethylamine (0.50 mL) and CTA (50 mg) were added. The reaction was stirred for 48 hours under N_2 atmosphere. The resulting nanoparticles were purified by concentrating *in vacuo*, followed by resuspending in dichloromethane, and precipitation with hexanes, and magnetic separation using a 2.54 cm^3 neodymium magnetic with a 54 kg pull force.

Synthesis of BAAm MNPs

CTA-MNPs (0.0626 g, 4.6 mmole CTA/g as determined by thermogravimetric analysis) were dispersed in DMF (120 mL) using ultrasonication. A Schlenk flask was charged with n-butyl acrylate (15.7642 g), acrylamide (3.7468 g), mesitylene (2.300 g, as internal standard), AIBN (9.6 mg), and the CTA-MNPs dispersed in DMF (monomer:CTA = 600:1). The flask was sealed with copper wire and a septum. The side arm was used for deoxygenation via bubbling nitrogen for 1.5 h. Prior to immersing in oil bath set at 57 °C a 100 μL aliquot was taken out and the MNP are removed magnetically to allow for NMR analysis. The conversion and subsequent degree of polymerization was calculated with ^{1}H NMR by comparing the integration of vinyl protons with respect to mesitylene protons. Once desired percent conversion was obtained (all kept <50%), 4-methoxyphenol was added as radical inhibitor. The polymer solution was precipitated by slow addition to 1 L of methanol-water mixture, (1:1 v/v), followed centrifugation in 250 mL Nalgene tubes at 7,000 rcf. The supernatant was discarded, and the polymer was solubilized in methanol-chloroform (1:1 v/v). The precipitation process was repeated 3 times. Polymer was then precipitated in 1 L hexanes (x2) followed by another two precipitations in methanol-water (1:1 v/v). Polymers were then dried overnight at 100 °C under vacuum and stored in a desiccator. Due to the magnetic nature of the nanoparticles NMR analysis of the resulting polymers could not be conducted.

4.6.2 Characterization of small molecules and composites

^{1}H NMR Characterization of CTA

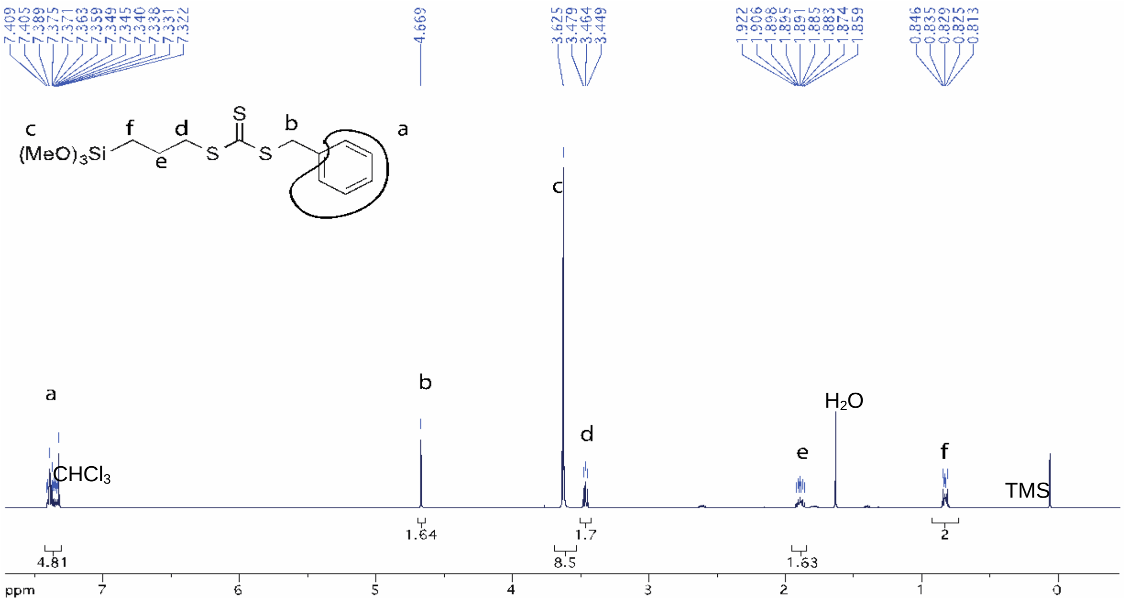

Figure 4.4 ^{1}H NMR spectra of CTA in $CDCl_3$.

Differential Scanning Calorimetry of Iron-oleate Precursor

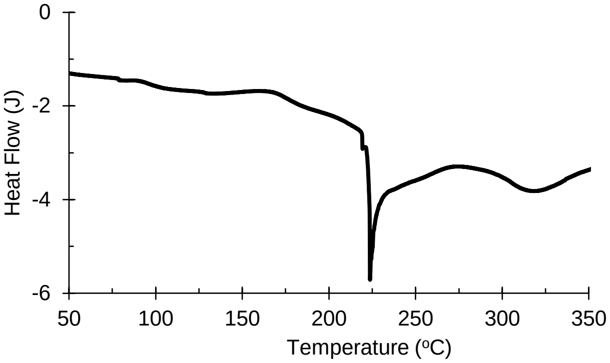

Figure 4.5 Differential scanning calorimetry of iron-oleate precursor. The nucleation (N) and growth (G) phases of nanoparticle synthesis endotherms occur at 220 °C and 320 °C, respectively, which are in agreement with literature.[242]

High Resolution Transmission Electron Micrograph of OA MNPs

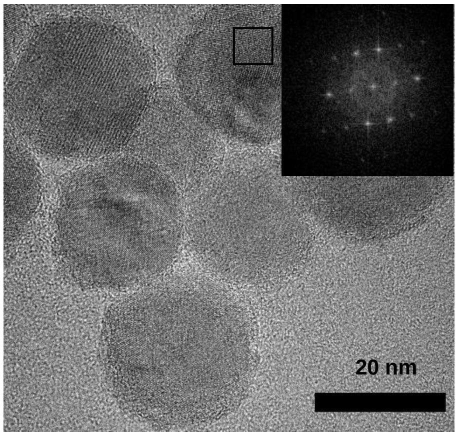

Figure 4.6 High resolution transmission electron micrograph, scale bar is 20 nm. Inset showing fast Fourier transform of the area outlined in the box showing lattice fringes indicative of crystallinity.

Thermogravimetric Analysis of BAAM-MNP Composites

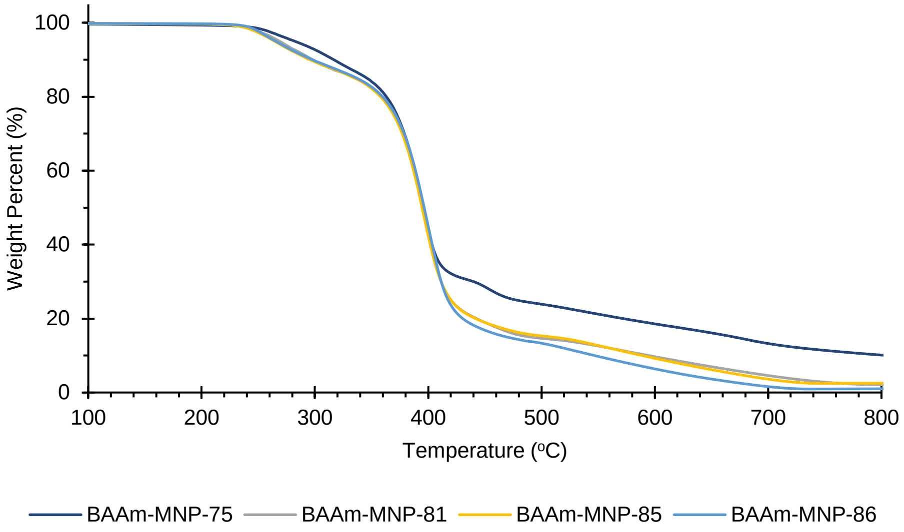

Figure 4.7 Thermogravimetric Analysis (TGA) was conducted on TA Instruments Q500 TGA. Samples were equilibrated at 100 ºC for 30 minutes under nitrogen, followed by a temperature ramp of 10 ºC/min to 800 ºC.

ATR FTIR Spectroscopy

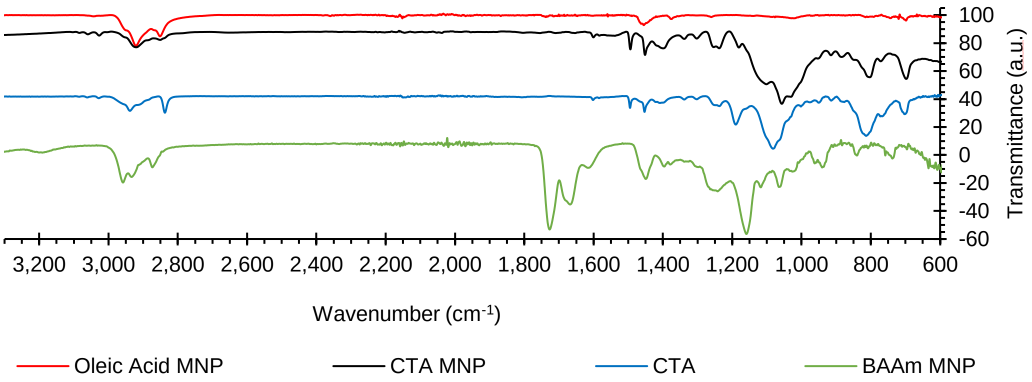

Figure 4.8 Full FTIR spectra of nanoparticles

Mechanical Testing Procedure

Samples were prepared by hot-pressing the composite into heated dog-bone Teflon molds at 100 °C followed by cooling to room temperature while maintaining the pressure (cooling time approximately 20 min). Average sample size was 13 mm × 3 mm × 1 mm (length, width, thickness). The mechanical properties of the composites were measured using an Instron 3365 machine in standard stress/strain experiments. The specimen was extended at 100 mm/min at room temperature. Each measurement was repeated at least three times.

Table 4.1 Mechanical and Thermal Properties of BAAm-MNP

Sample	wt % [a]	E (MPa) [b]	ε (mm/mm) [c]	σ (MPa) [d]	U (MJ/m^3) [e]
OA-MNP	7	N/A	N/A	N/A	N/A
CTA-MNP	25	N/A	N/A	N/A	N/A
BAAm-MNP-75	75	70 ± 10	5.4 ± 0.7	6.9 ± 0.8	28 ± 6
BAAm-MNP-81	81	10 ± 4	10 ± 1	8 ± 1	38 ± 6
BAAm-MNP-85	85	11 ± 4	11.3 ± 0.8	6 ± 1	40 ± 8
BAAm-MNP-86	86	16 ± 4	11.8 ± .8	8.0 ± 0.8	52 ± 6
BAAm-control[g]	100	12 ± 4	[f]	0.8 ± 0.1	[f]

[a] Weight percent (wt %) of volatile organic material as determined by thermogravimetric analysis (TGA). [b] Youngs modulus (E) is determined by calculating the initial slope from the uniaxial mechanical testing. [c] Extensibility at break (ε) is reported at a mm/mm. [d] The maximum stress at break (σ) is reported in MPa. [e] The toughness (U) is calculated by taking the area under the curve for the stress-strain curve. [f] BAAm-control is a linear copolymer BAAm with no MNP as control synthesized with small molecule CTA analogue and has a Mw of 38 kDa as determined by gel permeation chromatography. [f] No ε or U reported because samples did not break.

Mechanical Properties in Comparison to BAAm-control

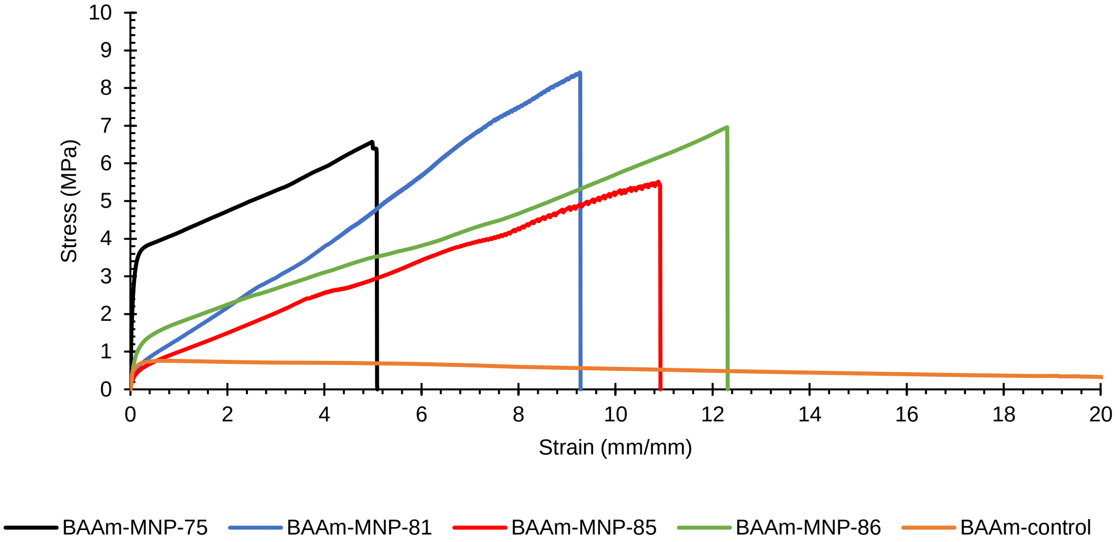

Figure 4.9 Mechanical properties of BAAm-MNP and BAAm-control. Samples strained at 100 mm/min.

Sample Damaging and Healing Tests

For self-healing tests, samples were prepared by hot-pressing the composite into heated dog-bone Teflon molds at 100 °C and cooling to room temperature while maintaining pressure (cooling time approximately 20 min). Average sample size was 13 mm × 3 mm × 1 mm (length, width, thickness). Samples were cleanly cut to 50% the width of the sample using a razor blade. The cut interfaces were gently pressed together for 1 minutes. Then samples were subject to different self-healing conditions. A pristine or uncut sample was subject to the same subsequent conditions and used for controls to determine self-healing efficiency. The samples were then allowed to cool down to room temperature (15 min) and were subjected to stress-strain tests at room temperature using an Instron 3365 machine in standard stress/strain experiments. Each experiment was repeated at least three times.

Strain-strain Curves BAAm-MNP-85 at 30 ºC for 2 h.

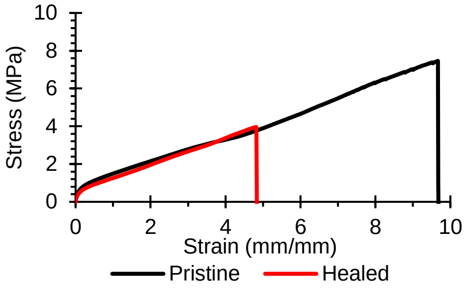

Figure 4.10 Stress-strain curves for BAAM-MNP-85. Samples strained at 100 mm/min.

Table 4.2 Mechanical Properties of Healed and Pristine BAAm-MNP-75 & 85 (ambient conditions).

Sample	**Healing (h)**	**Healing (ºC)**	**E (MPa)**	**ε (mm/mm)**	**σ (MPa)**	**U (MJ/m^3)**
BAAm-MNP-33	5	30	6 ± 1	7 ± 2	1.4 ± 0.2	7 ± 2
BAAm-MNP-33-Pristine	5	30	6 ± 1	16 ± 2	3.6 ± 0.6	29 ± 7
BAAm-MNP-85	2	30	17 ± 5	4.4 ± 0.4	4.1 ± 0.6	11 ± 2
BAAm-MNP-85-Pristine	2	30	13 ± 1	11 ± 3	7 ± 1	37 ± 14

Mechanical properties calculated from stress-strain curves at 100 mm/min and average and standard deviation reported from minimum of three samples. Youngs modulus (E) is determined by taking the slope of the second to seventh data point from the uniaxial mechanical testing. Extensibility at break (ε) is reported at a mm/mm. The maximum stress at break (σ) is reported in MPa. The toughness (U) is calculated by taking the area under the curve for the stress-strain curve.

Table 4.3 Self-healing Efficiency BAAm-MNP-33 & 85 (ambient conditions)

Samples	Healing (h)	Healing (ºC)	Recovery % of E (MPa)	Recovery % of ε (mm/mm)	Recovery % of σ (MPa)	Recovery % of U (MJ/m^3)
BAAm-MNP-33	5	30	90 ± 21	46 ± 13	39 ± 6	23 ± 6
BAAm-MNP-85	2	30	123 ± 38	41 ± 4	55 ± 9	25 ± 5

Youngs modulus (E) is determined by taking the slope of the second to seventh data point from the uniaxial mechanical testing run at 100 mm/min. Extensibility at break (ε) is reported at a mm/mm. The maximum stress at break (σ) is reported in MPa. The toughness (U) is calculated by taking the area under the curve for the stress-strain curve. The percentage is the percent of the property that was recovered of a damaged sample relative to an undamaged sample subject to the same environmental conditions.

Strain-strain Curves BAAm-MNP-33 at 80 ºC for 5 h (under reduced pressure)

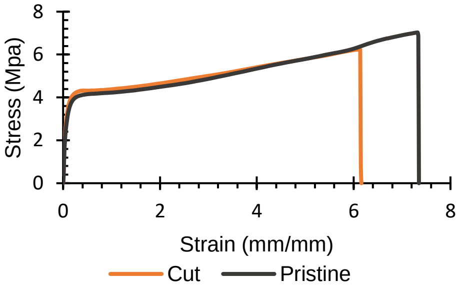

Figure 4.11 Stress-strain curves BAAm-MNP-33 at 80 ºC for 5 h. Samples strained at 200 mm/min.

Table 4.4 Mechanical Properties of Healed and Pristine BAAm-MNP-33 (80 ºC, 5h)

Sample	Healing (h)	Healing (ºC)	E (MPa)	ε (mm/mm)	σ (MPa)	U (MJ/m^3)
BAAm-MNP-33	5	80	54 ± 10	6.0 ± 0.9	6.2 ± 0.1	2216 ± 333
BAAm-MNP-33-Pristine	5	80	47 ± 19	8.6 ± 1.3	6.9 ± 0.3	3206 ± 1369

Mechanical properties calculated from stress-strain curves at 200 mm/min and average and standard deviation reported from minimum of three samples. Youngs modulus (E) is determined by taking the slope of the second to seventh data point from the uniaxial mechanical testing. Extensibility at break (ε) is reported at a mm/mm. The maximum stress at break (σ) is reported in MPa. The toughness (U) is calculated by taking the area under the curve for the stress-strain curve.

Table 4.5 Self-healing Efficiency BAAm-MNP-33 (80 ºC, 5h, reduced pressure)

Samples	Healing (h)	Healing (ºC)	Recovery % of E (MPa)	Recovery % of ε (mm/mm)	Recovery % of σ (MPa)	Recovery % of U (MJ/m^3)
BAAm-MNP-33	5	80	110 ± 22	74 ± 6	90 ± 1	75 ± 5

Youngs modulus (E) is determined by taking the slope of the second to seventh data point from the uniaxial mechanical testing at 200 mm/min. Extensibility at break (ε) is reported at a mm/mm. The maximum stress at break (σ) is reported in MPa. The toughness (U) is calculated by taking the area under the curve for the stress-strain curve.

Cleaving of BAAm Polymer from MNPs

100 mg of the BAAm-MNP-86 composite was dissolved in 3.5 mL of toluene in a high-density polyethylene bottle. Hydrofluoric acid (3.5 mL, 5%) was added and the solution was stirred at room temperature overnight. 4.0 mL of a saturated sodium bicarbonate solution was added and the resulting emulsion was precipitated in 200 mL of MeOH:H_2O (1:1) solution. The resulting

solid was characterized by gel permeation chromatography and H NMR spectroscopy to determine molecular weight and percent incorporation of acrylamide.

GPC of Cleaved BAAm Polymer from MNPs

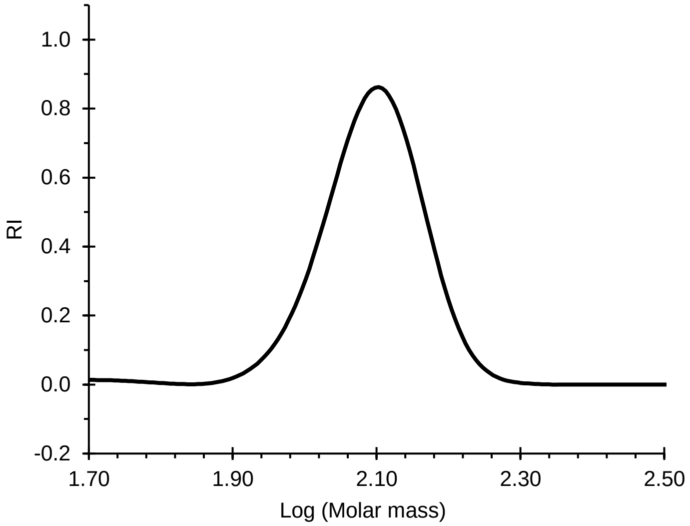

Figure 4.12 Gel permeation chromatogram of cleaved BAAm polymer. Gel permeation chromatogram (GPC) of cleaved BAAm polymer from MNPs. Mn=71.2 kDa Mw=115 kDa and polydispersity index of 1.62. The polymer corresponds to BAAm-MNP-86.

NMR of Cleaved BAAm Polymer from MNPs

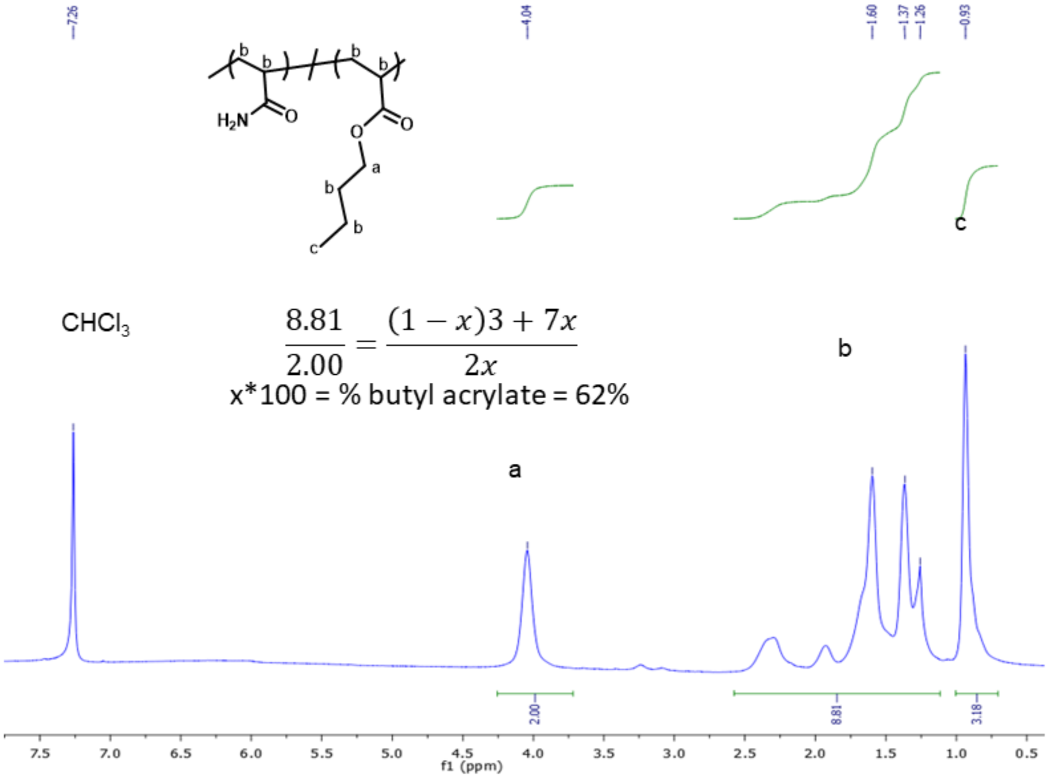

Figure 4.13 ^{1}H NMR spectra of BAAm-MNP-86 after cleaving from particles. NMR analysis of BAAm-MNP-86 after cleaving from MNP using hydrofluoric acid. The calculation for percent incorporation of butyl acrylate is shown above. The percent incorporation of butyl acylate is 62% and for acrylamide it’s 38% given a feed ratio of 60% and 30% of butyl acrylate and acrylamide, respectively.

References

(1) Ivanova, E.; Bazaka, K.; Crawford, R. *New Functional Biomaterials for Medicine and Healthcare*, 1st ed.; Woodhead Publishing. 2013

(2) Banerjee, S.; Tyagi, A. K. *Functional Materials*, 1st ed.; Elsevier, 2011.

(3) Poplavko, Y.; Yakymenko, Y. *Functional Dielectrics for Electronics*, 1st ed.; Woodhead Publishing, 2020.

(4) Filipcsei, G.; Csetneki, I.; Szilágyi, A.; Zrínyi, M. Magnetic Field-Responsive Smart Polymer Composites. In *Oligomers - Polymer Composites - Molecular Imprinting*; Gong, B., Sanford, A. R., Ferguson, J. S., Eds.; Advances in Polymer Science; Springer Berlin Heidelberg: Berlin, Heidelberg, 2007; pp 137–189. https://doi.org/10.1007/12_2006_104.

(5) Wu, L.; He, J.; Shang, W.; Deng, T.; Gu, J.; Su, H.; Liu, Q.; Zhang, W.; Zhang, D. Optical Functional Materials Inspired by Biology. *Advanced Optical Materials* **2016**, *4* (2), 195–224. https://doi.org/10.1002/adom.201500428.

(6) Yuan, K.; Shi, J.; Aftab, W.; Qin, M.; Usman, A.; Zhou, F.; Lv, Y.; Gao, S.; Zou, R. Engineering the Thermal Conductivity of Functional Phase-Change Materials for Heat Energy Conversion, Storage, and Utilization. *Advanced Functional Materials* **2020**, *30* (8), 1904228. https://doi.org/10.1002/adfm.201904228.

(7) Chapter 7 - Functional Materials. In *Pergamon Materials Series*; Cahn, R. W., Ed.; The Coming of Materials Science; Pergamon, 2001; Vol. 5, pp 253–304. https://doi.org/10.1016/S1470-1804(01)80010-9.

(8) Mozafari, M.; Chauhan, N. *Advanced Functional Polymers for Biomedical Applications*, 1st ed.; Elsevier, 2019.

(9) Sheikhpour, M.; Barani, L.; Kasaeian, A. Biomimetics in Drug Delivery Systems: A Critical Review. *Journal of Controlled Release* **2017**, *253*, 97–109. https://doi.org/10.1016/j.jconrel.2017.03.026.

(10) F. Turner, A. P. Biosensors: Sense and Sensibility. *Chemical Society Reviews* **2013**, *42* (8), 3184–3196. https://doi.org/10.1039/C3CS35528D.

(11) Liu, Y.; Pharr, M.; Salvatore, G. A. Lab-on-Skin: A Review of Flexible and Stretchable Electronics for Wearable Health Monitoring. *ACS Nano* **2017**. https://doi.org/10.1021/acsnano.7b04898.

(12) Alberts, B.; Johnson, A. D.; Lewis, J.; Morgan, D.; Raff, M.; Roberts, K.; Walter, P. *Molecular Biology of the Cell*, 6th ed.; W. W. Norton & Company: New York, NY, 2014.

(13) Rossum, S. A. P. van; Tena-Solsona, M.; Esch, J. H. van; Eelkema, R.; Boekhoven, J. Dissipative Out-of-Equilibrium Assembly of Man-Made Supramolecular Materials. *Chem. Soc. Rev.* **2017**, *46* (18), 5519–5535. https://doi.org/10.1039/C7CS00246G.

(14) Boekhoven, J.; Brizard, A. M.; Kowlgi, K. N. K.; Koper, G. J. M.; Eelkema, R.; van Esch, J. H. Dissipative Self-Assembly of a Molecular Gelator by Using a Chemical Fuel. *Angewandte Chemie International Edition* **2010**, *49* (28), 4825–4828. https://doi.org/10.1002/anie.201001511.

(15) K. Dambenieks, A.; Q. Vu, P. H.; M. Fyles, T. Dissipative Assembly of a Membrane Transport System. *Chem. Sci* **2014**, *5* (9), 3396–3403. https://doi.org/10.1039/C4SC01258E.

(16) Leira-Iglesias, J.; Tassoni, A.; Adachi, T.; Stich, M.; Hermans, T. M. Oscillations, Travelling Fronts and Patterns in a Supramolecular System. *Nat. Nanotechol.* **2018**, *13* (11), 1021–1027. https://doi.org/10.1038/s41565-018-0270-4.

(17) Kelly, T. R.; Cai, X.; Damkaci, F.; Panicker, S. B.; Tu, B.; Bushell, S. M.; Cornella, I.; Piggott, M. J.; Salives, R.; Cavero, M.; Zhao, Y.; Jasmin, S. Progress toward a Rationally Designed, Chemically Powered Rotary Molecular Motor. *J. Am. Chem. Soc.* **2007**, *129* (2), 376–386. https://doi.org/10.1021/ja066044a.

(18) Yoshida, R.; Ichijo, H.; Hakuta, T.; Yamaguchi, T. Self-Oscillating Swelling and Deswelling of Polymer Gels. *Macromolecular Rapid Communications* **1995**, *16* (4), 305–310. https://doi.org/10.1002/marc.1995.030160412.

(19) Zhang, D. Y.; Seelig, G. Dynamic DNA Nanotechnology Using Strand-Displacement Reactions. *Nat. Chem.* **2011**, *3* (2), 103–113. https://doi.org/10.1038/nchem.957.

(20) Green, L. N.; Subramanian, H. K. K.; Mardanlou, V.; Kim, J.; Hariadi, R. F.; Franco, E. Autonomous Dynamic Control of DNA Nanostructure Self-Assembly. *Nat. Chem.* **2019**, *11* (6), 510–520. https://doi.org/10.1038/s41557-019-0251-8.

(21) Debnath, S.; Roy, S.; Ulijn, R. V. Peptide Nanofibers with Dynamic Instability through Nonequilibrium Biocatalytic Assembly. *J. Am. Chem. Soc.* **2013**, *135* (45), 16789–16792. https://doi.org/10.1021/ja4086353.

(22) Carnall, J. M. A.; Waudby, C. A.; Belenguer, A. M.; Stuart, M. C. A.; Peyralans, J. J.-P.; Otto, S. Mechanosensitive Self-Replication Driven by Self-Organization. *Science* **2010**, *327* (5972), 1502–1506. https://doi.org/10.1126/science.1182767.

(23) Zhang, J.; Yan, J.; Granick, S. Directed Self-Assembly Pathways of Active Colloidal Clusters. *Angewandte Chemie International Edition* **2016**, *55* (17), 5166–5169. https://doi.org/10.1002/anie.201509978.

(24) Bissell, R. A.; Córdova, E.; Kaifer, A. E.; Stoddart, J. F. A Chemically and Electrochemically Switchable Molecular Shuttle. *Nature* **1994**, *369* (6476), 133–137. https://doi.org/10.1038/369133a0.

(25) Tierney, H. L.; Murphy, C. J.; Jewell, A. D.; Baber, A. E.; Iski, E. V.; Khodaverdian, H. Y.; McGuire, A. F.; Klebanov, N.; Sykes, E. C. H. Experimental Demonstration of a Single-Molecule Electric Motor. *Nature Nanotechnology* **2011**, *6* (10), 625–629. https://doi.org/10.1038/nnano.2011.142.

(26) Rakotondradany, F.; Whitehead, M. A.; Lebuis, A.-M.; Sleiman, H. F. Photoresponsive Supramolecular Systems: Self-Assembly of Azodibenzoic Acid Linear Tapes and Cyclic Tetramers. *Chemistry – A European Journal* **2003**, *9* (19), 4771–4780. https://doi.org/10.1002/chem.200304864.

(27) Klajn, R.; Wesson, P. J.; Bishop, K. J. M.; Grzybowski, B. A. Writing Self-Erasing Images Using Metastable Nanoparticle "Inks." *Angew. Chem. Int. Ed.* **2009**, *48* (38), 7035–7039. https://doi.org/10.1002/anie.200901119.

(28) Go, D.; Rommel, D.; Liao, Y.; Haraszti, T.; Sprakel, J.; C. Kuehne, A. J. Dissipative Disassembly of Colloidal Microgel Crystals Driven by a Coupled Cyclic Reaction Network. *Soft Matter* **2018**, *14* (6), 910–915. https://doi.org/10.1039/C7SM02061A.

(29) Herder, M.; Lehn, J.-M. The Photodynamic Covalent Bond: Sensitized Alkoxyamines as a Tool To Shift Reaction Networks Out-of-Equilibrium Using Light Energy. *J. Am. Chem. Soc.* **2018**, *140* (24), 7647–7657. https://doi.org/10.1021/jacs.8b03633.

(30) Grzybowski, B. A.; Fitzner, K.; Paczesny, J.; Granick, S. From Dynamic Self-Assembly to Networked Chemical Systems. *Chem. Soc. Rev.* **2017**, *46* (18), 5647–5678. https://doi.org/10.1039/C7CS00089H.

(31) Lozano, R.; Brogliato, B.; Egeland, O.; Maschke, B. Dissipative Systems. In *Dissipative Systems Analysis and Control: Theory and Applications*; Lozano, R., Brogliato, B., Egeland, O., Maschke, B., Eds.; Communications and Control Engineering; Springer: London, 2000; pp 111–166. https://doi.org/10.1007/978-1-4471-3668-2_4.

(32) Mattia, E.; Otto, S. Supramolecular Systems Chemistry. *Nat. Nanotechol.* **2015**, *10* (2), 111–119. https://doi.org/10.1038/nnano.2014.337.

(33) Bradshaw, R. A.; Dennis, E. A. *Handbook of Cell Signaling*, 1st ed.; Elsevier, 2003. https://doi.org/10.1016/B978-0-12-124546-7.X5358-3.

(34) Ranjith, P.; Mallick, K.; Joanny, J.-F.; Lacoste, D. Role of ATP-Hydrolysis in the Dynamics of a Single Actin Filament. *Biophys J* **2010**, *98* (8), 1418–1427. https://doi.org/10.1016/j.bpj.2009.12.4306.

(35) Katkar, H. H.; Davtyan, A.; Durumeric, A. E. P.; Hocky, G. M.; Schramm, A. C.; De La Cruz, E. M.; Voth, G. A. Insights into the Cooperative Nature of ATP Hydrolysis in Actin Filaments. *Biophysical Journal* **2018**, *115* (8), 1589–1602. https://doi.org/10.1016/j.bpj.2018.08.034.

(36) Walther, A. Viewpoint: From Responsive to Adaptive and Interactive Materials and Materials Systems: A Roadmap. *Advanced Materials* *n/a* (n/a), 1905111. https://doi.org/10.1002/adma.201905111.

(37) Kondepudi, D.; Petrosky, T.; Pojman, J. A. Dissipative Structures and Irreversibility in Nature: Celebrating 100th Birth Anniversary of Ilya Prigogine (1917–2003). *Chaos* **2017**, *27* (10), 104501. https://doi.org/10.1063/1.5008858.

(38) Ness, H. C. V. *Understanding Thermodynamics*; Courier Corporation, 1983.

(39) Brinke, E. te; Groen, J.; Herrmann, A.; Heus, H. A.; Rivas, G.; Spruijt, E.; Huck, W. T. S. Dissipative Adaptation in Driven Self-Assembly Leading to Self-Dividing Fibrils. *Nat. Nanotechol.* **2018**, *13* (9), 849. https://doi.org/10.1038/s41565-018-0192-1.

(40) Prigogine, I.; Nicolis, G. Biological Order, Structure and Instabilities1. *Quarterly Reviews of Biophysics* **1971**, *4* (2–3), 107–148. https://doi.org/10.1017/S0033583500000615.

(41) Jarzynski, C. Nonequilibrium Equality for Free Energy Differences. *Phys. Rev. Lett.* **1997**, *78* (14), 2690–2693.

(42) Gümrah Dumanli, A.; Savin, T. Recent Advances in the Biomimicry of Structural Colours. *Chemical Society Reviews* **2016**, *45* (24), 6698–6724. https://doi.org/10.1039/C6CS00129G.

(43) Volstad, N. L.; Boks, C. On the Use of Biomimicry as a Useful Tool for the Industrial Designer. *Sustainable Development* **2012**, *20* (3), 189–199. https://doi.org/10.1002/sd.1535.

(44) Lurie-Luke, E. Product and Technology Innovation: What Can Biomimicry Inspire? *Biotechnology Advances* **2014**, *32* (8), 1494–1505. https://doi.org/10.1016/j.biotechadv.2014.10.002.

(45) Pezzato, C.; Cheng, C.; Stoddart, J. F.; Astumian, R. D. Mastering the Non-Equilibrium Assembly and Operation of Molecular Machines. *Chem. Soc. Rev.* **2017**, *46* (18), 5491–5507. https://doi.org/10.1039/C7CS00068E.

(46) Esch, J. H. van; Klajn, R.; Otto, S. Chemical Systems out of Equilibrium. *Chem. Soc. Rev.* **2017**, *46* (18), 5474–5475. https://doi.org/10.1039/C7CS90088K.

(47) Qiao, S.; Wang, H. Temperature-Responsive Polymers: Synthesis, Properties, and Biomedical Applications. *Nano Res.* **2018**, *11* (10), 5400–5423. https://doi.org/10.1007/s12274-018-2121-x.

(48) Kocak, G.; Tuncer, C.; Bütün, V. PH-Responsive Polymers. *Polym. Chem.* **2016**, *8* (1), 144–176. https://doi.org/10.1039/C6PY01872F.

(49) Reichardt, C. Solvatochromic Dyes as Solvent Polarity Indicators. *Chem. Rev.* **1994**, *94* (8), 2319–2358. https://doi.org/10.1021/cr00032a005.

(50) Zhao, Y.; Ikeda, T. *Smart Light-Responsive Materials: Azobenzene-Containing Polymers and Liquid Crystals*; John Wiley & Sons, 2009.

(51) Pucci, A.; Ruggeri, G. Mechanochromic Polymer Blends. *Journal of Materials Chemistry* **2011**, *21* (23), 8282–8291. https://doi.org/10.1039/C0JM03653F.

(52) Stuart, M. A. C.; Huck, W. T. S.; Genzer, J.; Müller, M.; Ober, C.; Stamm, M.; Sukhorukov, G. B.; Szleifer, I.; Tsukruk, V. V.; Urban, M.; Winnik, F.; Zauscher, S.; Luzinov, I.; Minko, S. Emerging Applications of Stimuli-Responsive Polymer Materials. *Nature Materials* **2010**, *9* (2), 101–113. https://doi.org/10.1038/nmat2614.

(53) Pucci, A.; Bizzarri, R.; Ruggeri, G. Polymer Composites with Smart Optical Properties. *Soft Matter* **2011**, *7* (8), 3689–3700. https://doi.org/10.1039/C0SM01038C.

(54) Leng, J.; Lan, X.; Liu, Y.; Du, S. Shape-Memory Polymers and Their Composites: Stimulus Methods and Applications. *Progress in Materials Science* **2011**, *56* (7), 1077–1135. https://doi.org/10.1016/j.pmatsci.2011.03.001.

(55) M Mendes, P. Stimuli-Responsive Surfaces for Bio-Applications. *Chemical Society Reviews* **2008**, *37* (11), 2512–2529. https://doi.org/10.1039/B714635N.

(56) Guo, F.; Guo, Z. Inspired Smart Materials with External Stimuli Responsive Wettability: A Review. *RSC Advances* **2016**, *6* (43), 36623–36641. https://doi.org/10.1039/C6RA04079A.

(57) Mohammed, J. S.; Murphy, W. L. Bioinspired Design of Dynamic Materials. *Advanced Materials* **2009**, *21* (23), 2361–2374. https://doi.org/10.1002/adma.200803785.

(58) Urban, M. W. *Stimuli-Responsive Materials*; 2016.

(59) J. Kloxin, C.; N. Bowman, C. Covalent Adaptable Networks: Smart, Reconfigurable and Responsive Network Systems. *Chemical Society Reviews* **2013**, *42* (17), 7161–7173. https://doi.org/10.1039/C3CS60046G.

(60) Grinthal, A.; Aizenberg, J. Adaptive All the Way down: Building Responsive Materials from Hierarchies of Chemomechanical Feedback. *Chem. Soc. Rev.* **2013**, *42* (17), 7072–7085. https://doi.org/10.1039/C3CS60045A.

(61) Ge, F.; Zhao, Y. A New Function for Thermal Phase Transition-Based Polymer Actuators: Autonomous Motion on a Surface of Constant Temperature. *Chem. Sci* **2017**, *8* (9), 6307–6312. https://doi.org/10.1039/C7SC01792H.

(62) Palacci, J.; Sacanna, S.; Steinberg, A. P.; Pine, D. J.; Chaikin, P. M. Living Crystals of Light-Activated Colloidal Surfers. *Science* **2013**, *339* (6122), 936–940. https://doi.org/10.1126/science.1230020.

(63) Klajn, R. Spiropyran-Based Dynamic Materials. *Chem. Soc. Rev.* **2013**, *43* (1), 148–184. https://doi.org/10.1039/C3CS60181A.

(64) Samanta, D.; Klajn, R. Aqueous Light-Controlled Self-Assembly of Nanoparticles. *Advanced Optical Materials* **2016**, *4* (9), 1373–1377. https://doi.org/10.1002/adom.201600364.

(65) Ragazzon, G.; Baroncini, M.; Silvi, S.; Venturi, M.; Credi, A. Light-Powered Autonomous and Directional Molecular Motion of a Dissipative Self-Assembling System. *Nature Nanotechnology* **2015**, *10* (1), 70–75. https://doi.org/10.1038/nnano.2014.260.

(66) Serreli, V.; Lee, C.-F.; Kay, E. R.; Leigh, D. A. A Molecular Information Ratchet. *Nature* **2007**, *445* (7127), 523–527. https://doi.org/10.1038/nature05452.

(67) Wang, H.; Oster, G. Ratchets, Power Strokes, and Molecular Motors. *Applied Physics A* **2002**, *75* (2), 315–323. https://doi.org/10.1007/s003390201340.

(68) Chattopadhyay, K.; Varghese, V. Understanding Mechanical Energy Driven Nonequilibrium Processing: Some Results. *Materials Science and Engineering: A* **2004**, *375–377*, 72–77. https://doi.org/10.1016/j.msea.2003.10.006.

(69) Suryanarayana, C. Mechanical Alloying and Milling. *Progress in Materials Science* **2001**, *46* (1), 1–184. https://doi.org/10.1016/S0079-6425(99)00010-9.

(70) Kim, J.; Yoon, J.; Hayward, R. C. Dynamic Display of Biomolecular Patterns through an Elastic Creasing Instability of Stimuli-Responsive Hydrogels. *Nature Materials* **2010**, *9* (2), 159–164. https://doi.org/10.1038/nmat2606.

(71) Kelly, T. R.; De Silva, H.; Silva, R. A. Unidirectional Rotary Motion in a Molecular System. *Nature* **1999**, *401* (6749), 150–152. https://doi.org/10.1038/43639.

(72) Cheng, C.; McGonigal, P. R.; Schneebeli, S. T.; Li, H.; Vermeulen, N. A.; Ke, C.; Stoddart, J. F. An Artificial Molecular Pump. *Nature Nanotechnology* **2015**, *10* (6), 547–553. https://doi.org/10.1038/nnano.2015.96.

(73) Wilson, M. R.; Solà, J.; Carlone, A.; Goldup, S. M.; Lebrasseur, N.; Leigh, D. A. An Autonomous Chemically Fuelled Small-Molecule Motor. *Nature* **2016**, *534* (7606), 235–240. https://doi.org/10.1038/nature18013.

(74) Koumura, N.; Zijlstra, R. W. J.; van Delden, R. A.; Harada, N.; Feringa, B. L. Light-Driven Monodirectional Molecular Rotor. *Nature* **1999**, *401* (6749), 152–155. https://doi.org/10.1038/43646.

(75) Greb, L.; Lehn, J.-M. Light-Driven Molecular Motors: Imines as Four-Step or Two-Step Unidirectional Rotors. *J. Am. Chem. Soc.* **2014**, *136* (38), 13114–13117. https://doi.org/10.1021/ja506034n.

(76) Beves, J. E.; Blanco, V.; Blight, B. A.; Carrillo, R.; D'Souza, D. M.; Howgego, D.; Leigh, D. A.; Slawin, A. M. Z.; Symes, M. D. Toward Metal Complexes That Can Directionally Walk Along Tracks: Controlled Stepping of a Molecular Biped with a Palladium(II) Foot. *J. Am. Chem. Soc.* **2014**, *136* (5), 2094–2100. https://doi.org/10.1021/ja4123973.

(77) Leira-Iglesias, J.; Sorrenti, A.; Sato, A.; A. Dunne, P.; M. Hermans, T. Supramolecular Pathway Selection of Perylenediimides Mediated by Chemical Fuels. *Chem. Comm.* **2016**, *52* (58), 9009–9012. https://doi.org/10.1039/C6CC01192F.

(78) Boekhoven, J.; Hendriksen, W. E.; Koper, G. J. M.; Eelkema, R.; Esch, J. H. van. Transient Assembly of Active Materials Fueled by a Chemical Reaction. *Science* **2015**, *349* (6252), 1075–1079. https://doi.org/10.1126/science.aac6103.

(79) Kariyawasam, L. S.; Hartley, C. S. Dissipative Assembly of Aqueous Carboxylic Acid Anhydrides Fueled by Carbodiimides. *J. Am. Chem. Soc.* **2017**, *139* (34), 11949–11955. https://doi.org/10.1021/jacs.7b06099.

(80) Prasad, S. K.; Nair, G. G.; Hegde, G. Dynamic Self-Assembly of the Liquid-Crystalline Smectic A Phase. *Advanced Materials* **2005**, *17* (17), 2086–2091. https://doi.org/10.1002/adma.200500161.

(81) Maiti, S.; Fortunati, I.; Ferrante, C.; Scrimin, P.; Prins, L. J. Dissipative Self-Assembly of Vesicular Nanoreactors. *Nat. Chem.* **2016**, *8* (7), 725–731. https://doi.org/10.1038/nchem.2511.

(82) Heinen, L.; Walther, A. Temporal Control of I-Motif Switch Lifetimes for Autonomous Operation of Transient DNA Nanostructures. *Chemical Science* **2017**, *8* (5), 4100–4107. https://doi.org/10.1039/C7SC00646B.

(83) Epstein, I. R.; Xu, B. Reaction–Diffusion Processes at the Nano- and Microscales. *Nature Nanotechnology* **2016**, *11* (4), 312–319. https://doi.org/10.1038/nnano.2016.41.

(84) Yoshida, R.; Ueki, T. Evolution of Self-Oscillating Polymer Gels as Autonomous Polymer Systems. *NPG Asia Materials* **2014**, *6* (6), e107. https://doi.org/10.1038/am.2014.32.

(85) Tan, Z.; Chen, S.; Peng, X.; Zhang, L.; Gao, C. Polyamide Membranes with Nanoscale Turing Structures for Water Purification. *Science* **2018**, *360* (6388), 518–521. https://doi.org/10.1126/science.aar6308.

(86) Illien, P.; Golestanian, R.; Sen, A. ‘Fuelled’ Motion: Phoretic Motility and Collective Behaviour of Active Colloids. *Chem. Soc. Rev.* **2017**, *46* (18), 5508–5518. https://doi.org/10.1039/C7CS00087A.

(87) Paxton, W. F.; Kistler, K. C.; Olmeda, C. C.; Sen, A.; St. Angelo, S. K.; Cao, Y.; Mallouk, T. E.; Lammert, P. E.; Crespi, V. H. Catalytic Nanomotors: Autonomous Movement of Striped Nanorods. *J. Am. Chem. Soc.* **2004**, *126* (41), 13424–13431. https://doi.org/10.1021/ja047697z.

(88) Ibele, M. E.; Lammert, P. E.; Crespi, V. H.; Sen, A. Emergent, Collective Oscillations of Self-Mobile Particles and Patterned Surfaces under Redox Conditions. *ACS Nano* **2010**, *4* (8), 4845–4851. https://doi.org/10.1021/nn101289p.

(89) Feynman, R. P.; Leighton, R. B.; Sands, M. *The Feynman Lectures on Physics, Vol. I: The New Millennium Edition: Mainly Mechanics, Radiation, and Heat*; Basic Books, 2011.

(90) Astumian, R. D. Stochastic Conformational Pumping: A Mechanism for Free-Energy Transduction by Molecules. *Annu. Rev. Biophys.* **2011**, *40* (1), 289–313. https://doi.org/10.1146/annurev-biophys-042910-155355.

(91) Collins, B. S. L.; Kistemaker, J. C. M.; Otten, E.; Feringa, B. L. A Chemically Powered Unidirectional Rotary Molecular Motor Based on a Palladium Redox Cycle. *Nature Chemistry* **2016**, *8* (9), 860–866. https://doi.org/10.1038/nchem.2543.

(92) Stoddart, J. F. Mechanically Interlocked Molecules (MIMs)—Molecular Shuttles, Switches, and Machines (Nobel Lecture). *Angewandte Chemie International Edition* **2017**, *56* (37), 11094–11125. https://doi.org/10.1002/anie.201703216.

(93) Sauvage, J.-P. From Chemical Topology to Molecular Machines (Nobel Lecture). *Angewandte Chemie International Edition* **2017**, *56* (37), 11080–11093. https://doi.org/10.1002/anie.201702992.

(94) Dietrich-Buchecker, C. O.; Sauvage, J. P.; Kern, J. M. Templated Synthesis of Interlocked Macrocyclic Ligands: The Catenands. *J. Am. Chem. Soc.* **1984**, *106* (10), 3043–3045. https://doi.org/10.1021/ja00322a055.

(95) Eelkema, R.; Pollard, M. M.; Vicario, J.; Katsonis, N.; Ramon, B. S.; Bastiaansen, C. W. M.; Broer, D. J.; Feringa, B. L. Nanomotor Rotates Microscale Objects. *Nature* **2006**, *440* (7081), 163–163. https://doi.org/10.1038/440163a.

(96) Li, Q.; Fuks, G.; Moulin, E.; Maaloum, M.; Rawiso, M.; Kulic, I.; Foy, J. T.; Giuseppone, N. Macroscopic Contraction of a Gel Induced by the Integrated Motion of Light-Driven

Molecular Motors. *Nature Nanotechnology* **2015**, *10* (2), 161–165. https://doi.org/10.1038/nnano.2014.315.

(97) Tena-Solsona, M.; Rieß, B.; Grötsch, R. K.; Löhrer, F. C.; Wanzke, C.; Käsdorf, B.; Bausch, A. R.; Müller-Buschbaum, P.; Lieleg, O.; Boekhoven, J. Non-Equilibrium Dissipative Supramolecular Materials with a Tunable Lifetime. *Nat. Commun.* **2017**, *8*, 15895. https://doi.org/10.1038/ncomms15895.

(98) Jong, J. J. D. de; Hania, P. R.; Pugžlys, A.; Lucas, L. N.; Loos, M. de; Kellogg, R. M.; Feringa, B. L.; Duppen, K.; Esch, J. H. van. Light-Driven Dynamic Pattern Formation. *Angew. Chem. Int. Ed.* **2005**, *44* (16), 2373–2376. https://doi.org/10.1002/anie.200462500.

(99) Wang, G.; Tang, B.; Liu, Y.; Gao, Q.; Wang, Z.; Zhang, X. The Fabrication of a Supra-Amphiphile for Dissipative Self-Assembly. *Chemical Science* **2016**, *7* (2), 1151–1155. https://doi.org/10.1039/C5SC03907J.

(100) Maeda, S.; Hara, Y.; Sakai, T.; Yoshida, R.; Hashimoto, S. Self-Walking Gel. *Adv. Mater.* **2007**, *19* (21), 3480–3484. https://doi.org/10.1002/adma.200700625.

(101) Ogden, W., A.; Guan, Z. Redox Chemical-Fueled Dissipative Self-Assembly of Active Materials - Ogden - - ChemSystemsChem - Wiley Online Library. *ChemSystemsChem* **2019**, *1*, e1900030.

(102) Aragón, J. L.; Barrio, R. A.; Woolley, T. E.; Baker, R. E.; Maini, P. K. Nonlinear Effects on Turing Patterns: Time Oscillations and Chaos. *Phys. Rev. E* **2012**, *86* (2), 026201. https://doi.org/10.1103/PhysRevE.86.026201.

(103) Lagzi, I.; Kowalczyk, B.; Wang, D.; Grzybowski, B. A. Nanoparticle Oscillations and Fronts. *Angew. Chem. Int. Ed.* **2010**, *49*, 8616–8619. https://doi.org/10.1002/anie.201004231.

(104) Suzuki, D.; Sakai, T.; Yoshida, R. Self-Flocculating/Self-Dispersing Oscillation of Microgels. *Angewandte Chemie International Edition* **2008**, *47* (5), 917–920. https://doi.org/10.1002/anie.200703953.

(105) Zhao, H.; Sen, S.; Udayabhaskararao, T.; Sawczyk, M.; Kučanda, K.; Manna, D.; Kundu, P. K.; Lee, J.-W.; Král, P.; Klajn, R. Reversible Trapping and Reaction Acceleration within Dynamically Self-Assembling Nanoflasks. *Nature Nanotechnology* **2016**, *11* (1), 82–88. https://doi.org/10.1038/nnano.2015.256.

(106) Dreyfus, R.; Baudry, J.; Roper, M. L.; Fermigier, M.; Stone, H. A.; Bibette, J. Microscopic Artificial Swimmers. *Nature* **2005**, *437* (7060), 862–865. https://doi.org/10.1038/nature04090.

(107) Wilson, D. A.; Nolte, R. J. M.; Hest, J. C. M. van. Autonomous Movement of Platinum-Loaded Stomatocytes. *Nat. Chem.* **2012**, *4* (4), 268–274. https://doi.org/10.1038/nchem.1281.

(108) Sawczyk, M.; Klajn, R. Out-of-Equilibrium Aggregates and Coatings during Seeded Growth of Metallic Nanoparticles. *J. Am. Chem. Soc.* **2017**, *139* (49), 17973–17978. https://doi.org/10.1021/jacs.7b09111.

(109) van Ravensteijn, B. G. P.; Hendriksen, W. E.; Eelkema, R.; van Esch, J. H.; Kegel, W. K. Fuel-Mediated Transient Clustering of Colloidal Building Blocks. *J. Am. Chem. Soc.* **2017**, *139* (29), 9763–9766. https://doi.org/10.1021/jacs.7b03263.

(110) Zhang, J.; Luijten, E.; A. Grzybowski, B.; Granick, S. Active Colloids with Collective Mobility Status and Research Opportunities. *Chemical Society Reviews* **2017**, *46* (18), 5551–5569. https://doi.org/10.1039/C7CS00461C.

(111) Keh, H. J.; Chen, S. B. Diffusiophoresis and Electrophoresis of Colloidal Cylinders. *Langmuir* **1993**, *9* (4), 1142–1149. https://doi.org/10.1021/la00028a044.

(112) Ibele, M.; Mallouk, T. E.; Sen, A. Schooling Behavior of Light-Powered Autonomous Micromotors in Water. *Angewandte Chemie International Edition* **2009**, *48* (18), 3308–3312. https://doi.org/10.1002/anie.200804704.

(113) Duan, W.; Liu, R.; Sen, A. Transition between Collective Behaviors of Micromotors in Response to Different Stimuli. *J. Am. Chem. Soc.* **2013**, *135* (4), 1280–1283. https://doi.org/10.1021/ja3120357.

(114) Ismagilov, R. F.; Schwartz, A.; Bowden, N.; Whitesides, G. M. Autonomous Movement and Self-Assembly. *Angewandte Chemie International Edition* **2002**, *41* (4), 652–654. https://doi.org/10.1002/1521-3773(20020215)41:4<652::AID-ANIE652>3.0.CO;2-U.

(115) Theurkauff, I.; Cottin-Bizonne, C.; Palacci, J.; Ybert, C.; Bocquet, L. Dynamic Clustering in Active Colloidal Suspensions with Chemical Signaling. *Phys. Rev. Lett.* **2012**, *108* (26), 268303. https://doi.org/10.1103/PhysRevLett.108.268303.

(116) Tu, Y.; Peng, F.; Sui, X.; Men, Y.; White, P. B.; van Hest, J. C. M.; Wilson, D. A. Self-Propelled Supramolecular Nanomotors with Temperature-Responsive Speed Regulation. *Nature Chemistry* **2017**, *9* (5), 480–486. https://doi.org/10.1038/nchem.2674.

(117) Timonen, J. V. I.; Latikka, M.; Leibler, L.; Ras, R. H. A.; Ikkala, O. Switchable Static and Dynamic Self-Assembly of Magnetic Droplets on Superhydrophobic Surfaces. *Science* **2013**, *341* (6143), 253–257. https://doi.org/10.1126/science.1233775.

(118) Cunha, M. P. da; Peeketi, A. R.; Mehta, K.; Broer, D. J.; Annabattula, R. K.; Schenning, A. P. H. J.; Debije, M. G. A Self-Sustained Soft Actuator Able to Rock and Roll. *Chem. Commun.* **2019**, *55* (74), 11029–11032. https://doi.org/10.1039/C9CC05329H.

(119) Horváth, J. Chemomechanical Oscillations with a Non-Redox Non-Oscillatory Reaction. *Chemical Communications* **2017**, *53* (36), 4973–4976. https://doi.org/10.1039/C7CC02497E.

(120) Korevaar, P. A.; Kaplan, C. N.; Grinthal, A.; Rust, R. M.; Aizenberg, J. Non-Equilibrium Signal Integration in Hydrogels. *Nature Communications* **2020**, *11* (1), 1–10. https://doi.org/10.1038/s41467-019-14114-0.

(121) Heuser, T.; Merindol, R.; Loescher, S.; Klaus, A.; Walther, A. Photonic Devices Out of Equilibrium: Transient Memory, Signal Propagation, and Sensing. *Adv. Mater.* **2017**, *29* (17), 1606842. https://doi.org/10.1002/adma.201606842.

(122) Rieß, B.; Boekhoven, J. Applications of Dissipative Supramolecular Materials with a Tunable Lifetime. *ChemNanoMat* **2018**, *4* (8), 710–719. https://doi.org/10.1002/cnma.201800169.

(123) Camazine, S.; Deneubourg, J.-L.; Franks, N. R.; Sneyd, J.; Bonabeau, E.; Theraula, G. *Self-Organization in Biological Systems*; Princeton University Press, 2003.

(124) He, X.; Aizenberg, M.; Kuksenok, O.; Zarzar, L. D.; Shastri, A.; Balazs, A. C.; Aizenberg, J. Synthetic Homeostatic Materials with Chemo-Mechano-Chemical Self-Regulation. *Nature* **2012**, *487* (7406), 214–218. https://doi.org/10.1038/nature11223.

(125) He, X.; Aizenberg, M.; Kuksenok, O.; Zarzar, L. D.; Shastri, A.; Balazs, A. C.; Aizenberg, J. Synthetic Homeostatic Materials with Chemo-Mechano-Chemical Self-Regulation. *Nature* **2012**, *487* (7406), 214–218. https://doi.org/10.1038/nature11223.

(126) Qian, X.; Zhao, Y.; Alsaid, Y.; Wang, X.; Hua, M.; Galy, T.; Gopalakrishna, H.; Yang, Y.; Cui, J.; Liu, N.; Marszewski, M.; Pilon, L.; Jiang, H.; He, X. Artificial Phototropism for

Omnidirectional Tracking and Harvesting of Light. *Nat. Nanotechnol.* **2019**, *14* (11), 1048–1055. https://doi.org/10.1038/s41565-019-0562-3.

(127) Josephson, R. K. Mechanical Power Output from Striated Muscle during Cyclic Contraction. *Journal of Experimental Biology* **1985**, *114* (1), 493–512.

(128) Yamaguchi, M.; Yoshimoto, E.; Kondo, S. Pattern Regulation in the Stripe of Zebrafish Suggests an Underlying Dynamic and Autonomous Mechanism. *PNAS* **2007**, *104* (12), 4790–4793. https://doi.org/10.1073/pnas.0607790104.

(129) Nakamasu, A.; Takahashi, G.; Kanbe, A.; Kondo, S. Interactions between Zebrafish Pigment Cells Responsible for the Generation of Turing Patterns. *PNAS* **2009**, *106* (21), 8429–8434. https://doi.org/10.1073/pnas.0808622106.

(130) Heinen, L.; Walther, A. Programmable Dynamic Steady States in ATP-Driven Nonequilibrium DNA Systems. *Sci. Adv.* **2019**, *5* (7), eaaw0590. https://doi.org/10.1126/sciadv.aaw0590.

(131) Merindol, R.; Walther, A. Materials Learning from Life: Concepts for Active, Adaptive and Autonomous Molecular Systems. *Chem. Soc. Rev.* **2017**, *46* (18), 5588–5619. https://doi.org/10.1039/C6CS00738D.

(132) Zhang, H.; Zeng, H.; Priimagi, A.; Ikkala, O. Programmable Responsive Hydrogels Inspired by Classical Conditioning Algorithm. *Nature Communications* **2019**, *10* (1), 1–8. https://doi.org/10.1038/s41467-019-11260-3.

(133) Prigogine, I.; Nicolis, G.; Babloyantz, A. Nonequilibrium Problems in Biological Phenomena. *Ann. N. Y. Acad. Sci.* **1974**, *231* (1), 99–100. https://doi.org/10.1111/j.1749-6632.1974.tb20557.x.

(134) Hess, H.; Ross, J. L. Non-Equilibrium Assembly of Microtubules: From Molecules to Autonomous Chemical Robots. *Chem. Soc. Rev.* **2017**, *46* (18), 5570–5587. https://doi.org/10.1039/C7CS00030H.

(135) Prigogine, I. *Introduction to Thermodynamics of Irreversible Processes*; Wiley: New York, 1968.

(136) Choudhury, U.; Singh, D., P.; Qui, T.; Fischer, P. Chemical Nanomotors at the Gram Scale Form a Dense Active Optorheological Medium - Choudhury - 2019 - Advanced Materials - Wiley Online Library. *Adv. Mater.* **2019**, *31*, 1807382.

(137) Kundu, P. K.; Samanta, D.; Leizrowice, R.; Margulis, B.; Zhao, H.; Börner, M.; Udayabhaskararao, T.; Manna, D.; Klajn, R. Light-Controlled Self-Assembly of Non-Photoresponsive Nanoparticles. *Nat. Chem.* **2015**, *7* (8), 646–652. https://doi.org/10.1038/nchem.2303.

(138) Mourran, A.; Zhang, H.; Vinokur, R.; Möller, M. Soft Microrobots Employing Nonequilibrium Actuation via Plasmonic Heating. *Advanced Materials* **2017**, *29* (2), 1604825. https://doi.org/10.1002/adma.201604825.

(139) Kudernac, T.; Ruangsupapichat, N.; Parschau, M.; Maciá, B.; Katsonis, N.; Harutyunyan, S. R.; Ernst, K.-H.; Feringa, B. L. Electrically Driven Directional Motion of a Four-Wheeled Molecule on a Metal Surface. *Nature* **2011**, *479* (7372), 208–211. https://doi.org/10.1038/nature10587.

(140) Caton, J. A. The Thermodynamics of Internal Combustion Engines: Examples of Insights. *Inventions* **2018**, *3* (2), 33. https://doi.org/10.3390/inventions3020033.

(141) B. Goodenough, J. Electrochemical Energy Storage in a Sustainable Modern Society. *Energy Environ. Sci.* **2014**, *7* (1), 14–18. https://doi.org/10.1039/C3EE42613K.

(142) Mishra, A.; Korlepara, D. B.; Kumar, M.; Jain, A.; Jonnalagadda, N.; Bejagam, K. K.; Balasubramanian, S.; George, S. J. Biomimetic Temporal Self-Assembly via Fuel-Driven Controlled Supramolecular Polymerization. *Nat. Commun.* **2018**, *9* (1), 1–9. https://doi.org/10.1038/s41467-018-03542-z.

(143) Heuser, T.; Weyandt, E.; Walther, A. Biocatalytic Feedback-Driven Temporal Programming of Self-Regulating Peptide Hydrogels. *Angew. Chem. Int. Ed.* **2015**, *54* (45), 13258–13262. https://doi.org/10.1002/anie.201505013.

(144) Jones, R. A. L. *Soft Machines: Nanotechnology and Life*; Oxford University Press: New York, 2004.

(145) Gelebart, A. H.; Jan Mulder, D.; Varga, M.; Konya, A.; Vantomme, G.; Meijer, E. W.; Selinger, R. L. B.; Broer, D. J. Making Waves in a Photoactive Polymer Film. *Nature* **2017**, *546* (7660), 632–636. https://doi.org/10.1038/nature22987.

(146) Yamada, M.; Kondo, M.; Mamiya, J.; Yu, Y.; Kinoshita, M.; Barrett, C. J.; Ikeda, T. Photomobile Polymer Materials: Towards Light-Driven Plastic Motors. *Angewandte Chemie International Edition* **2008**, *47* (27), 4986–4988. https://doi.org/10.1002/anie.200800760.

(147) Kay, E. R.; Leigh, D. A.; Zerbetto, F. Synthetic Molecular Motors and Mechanical Machines. *Angew. Chem. Int. Ed.* **2007**, *46* (1–2), 72–191. https://doi.org/10.1002/anie.200504313.

(148) Browne, W. R.; Feringa, B. L. Making Molecular Machines Work. *Nat. Nanotechol.* **2006**, *1* (1), 25–35. https://doi.org/10.1038/nnano.2006.45.

(149) Urtel, G.; Estevez-Torres, A.; Galas, J.-C. DNA-Based Long-Lived Reaction–Diffusion Patterning in a Host Hydrogel. *Soft Matter* **2019**, *15* (45), 9343–9351. https://doi.org/10.1039/C9SM01786K.

(150) Kuksenok, O.; Balazs, A. C. Designing Dual-Functionalized Gels for Self-Reconfiguration and Autonomous Motion. *Scientific Reports* **2015**, *5* (1), 1–7. https://doi.org/10.1038/srep09569.

(151) Najafi, M.; Hebels, E.; Hennink, W. E.; Vermonden, T. Poly(N-Isopropylacrylamide): Physicochemical Properties and Biomedical Applications. In *Temperature-Responsive Polymers*; 2018; pp 1–34. https://doi.org/10.1002/9781119157830.ch1.

(152) Jones, G. O.; Houk, K. N. Predictions of Substituent Effects in Thermal Azide 1,3-Dipolar Cycloadditions: Implications for Dynamic Combinatorial (Reversible) and Click (Irreversible) Chemistry. *J. Org. Chem.* **2008**, *73* (4), 1333–1342. https://doi.org/10.1021/jo702295d.

(153) Presolski, Stanislav. I.; Hong, V.; Cho, S.-H.; Finn, M. G. Tailored Ligand Acceleration of the Cu-Catalyzed Azide−Alkyne Cycloaddition Reaction: Practical and Mechanistic Implications | Journal of the American Chemical Society. *J. Am. Chem. Soc 132* (41), 14570–14576. https://doi.org/ttps://doi.org/10.1021/ja105743g.

(154) Kislukhin, A. A.; Hong, V. P.; Breitenkamp, K. E.; Finn, M. G. Relative Performance of Alkynes in Copper-Catalyzed Azide–Alkyne Cycloaddition. *Bioconjugate Chem.* **2013**, *24* (4), 684–689. https://doi.org/10.1021/bc300672b.

(155) Rice, C. V. Phase-Transition Thermodynamics of N-Isopropylacrylamide Hydrogels. *Biomacromolecules* **2006**, *7* (10), 2923–2925. https://doi.org/10.1021/bm060607t.

(156) Debord, J. D.; Lyon, L. A. Synthesis and Characterization of PH-Responsive Copolymer Microgels with Tunable Volume Phase Transition Temperatures. *Langmuir* **2003**, *19* (18), 7662–7664. https://doi.org/10.1021/la0342924.

(157) Hoshino, Y.; Urakami, T.; Kodama, T.; Koide, H.; Oku, N.; Okahata, Y.; Shea, K. J. Design of Synthetic Polymer Nanoparticles That Capture and Neutralize a Toxic Peptide. *Small* **2009**, *5* (13), 1562–1568. https://doi.org/10.1002/smll.200900186.

(158) Zhang, X.-Z.; Chu, C.-C. Thermosensitive PNIPAAm Cryogel with Superfast and Stable Oscillatory Properties. *Chemical Communications* **2003**, *0* (12), 1446–1447. https://doi.org/10.1039/B301423A.

(159) Sun, P.; Zhang, H.; Xu, D.; Wang, Z.; Wang, L.; Gao, G.; Hossain, G.; Wu, J.; Wang, R.; Fu, J. Super Tough Bilayer Actuators Based on Multi-Responsive Hydrogels Crosslinked by Functional Triblock Copolymer Micelle Macro-Crosslinkers. *J. Mater. Chem. B* **2019**, *7* (16), 2619–2625. https://doi.org/10.1039/C9TB00249A.

(160) Zheng, W. J.; An, N.; Yang, J. H.; Zhou, J.; Chen, Y. M. Tough Al-Alginate/Poly(N-Isopropylacrylamide) Hydrogel with Tunable LCST for Soft Robotics. *ACS Appl. Mater. Interfaces* **2015**, *7* (3), 1758–1764. https://doi.org/10.1021/am507339r.

(161) Chiklis, C. K.; Grasshoff, J. M. Swelling of Thin Films. I. Acrylamide–N-isopropylacrylamide Copolymers in Water. *J. Polym. Sci., Part B: Polym. Phys.* **1970**, *8* (9), 1617–1626. https://doi.org/10.1002/pol.1970.160080914.

(162) Zhu, X.; Yang, W.; Hatzell, M. C.; Logan, B. E. Energy Recovery from Solutions with Different Salinities Based on Swelling and Shrinking of Hydrogels. *Environ. Sci. Technol.* **2014**, *48* (12), 7157–7163. https://doi.org/10.1021/es500909q.

(163) Choi, J.; Moquin, A.; Bomal, E.; Na, L.; Maysinger, D.; Kakkar, A. Telodendrimers for Physical Encapsulation and Covalent Linking of Individual or Combined Therapeutics. *Mol. Pharmaceutics* **2017**, *14* (8), 2607–2615. https://doi.org/10.1021/acs.molpharmaceut.7b00019.

(164) Arens, L.; Weißenfeld, F.; Klein, C. O.; Schlag, K.; Wilhelm, M. Osmotic Engine: Translating Osmotic Pressure into Macroscopic Mechanical Force via Poly(Acrylic Acid) Based Hydrogels. *Advanced Science* **2017**, *4* (9), 1700112. https://doi.org/10.1002/advs.201700112.

(165) Howse, J. R.; Topham, P.; Crook, C. J.; Gleeson, A. J.; Bras, W.; Jones, R. A. L.; Ryan, A. J. Reciprocating Power Generation in a Chemically Driven Synthetic Muscle. *Nano Lett.* **2006**, *6* (1), 73–77. https://doi.org/10.1021/nl0520617.

(166) Benyus, J. M. *Biomimicry: Innovation Inspired by Nature*; Harper Perennial: New York, N.Y, 2002.

(167) Saltiel, A. R.; Kahn, C. R. Insulin Signalling and the Regulation of Glucose and Lipid Metabolism. *Nature* **2001**, *414* (6865), 799–806. https://doi.org/10.1038/414799a.

(168) Staddon, J. E. R. *Adaptive Behavior and Learning*; Cambridge University Press, 2016.

(169) Hergenhahn, B. R.; Olson, M. H. *An Introduction to Theories of Learning*; Pearson Prentice Hall, 2005.

(170) Gandhi, N.; Ashkenasy, G.; Tannenbaum, E. Associative Learning in Biochemical Networks. *Journal of Theoretical Biology* **2007**, *249* (1), 58–66. https://doi.org/10.1016/j.jtbi.2007.07.004.

(171) Lerch, M. M.; Grinthal, A.; Aizenberg, J. Viewpoint: Homeostasis as Inspiration—Toward Interactive Materials. *Advanced Materials* *n/a* (n/a), 1905554. https://doi.org/10.1002/adma.201905554.

(172) Jones, S. J.; Taylor, A. F.; Beales, P. A. Towards Feedback-Controlled Nanomedicines for Smart, Adaptive Delivery: *Experimental Biology and Medicine* **2018**. https://doi.org/10.1177/1535370218800456.

(173) Siegel, R. A. Stimuli Sensitive Polymers and Self Regulated Drug Delivery Systems: A Very Partial Review. *Journal of Controlled Release* **2014**, *190*, 337–351. https://doi.org/10.1016/j.jconrel.2014.06.035.

(174) Hauser, A. W.; Sundaram, S.; Hayward, R. C. Photothermocapillary Oscillators. *Phys. Rev. Lett.* **2018**, *121* (15), 158001. https://doi.org/10.1103/PhysRevLett.121.158001.

(175) Making waves in a photoactive polymer film | Nature https://www.nature.com/articles/nature22987 (accessed Mar 27, 2020).

(176) Semenov, S. N.; Wong, A. S. Y.; Made, R. M. van der; Postma, S. G. J.; Groen, J.; Roekel, H. W. H. van; Greef, T. F. A. de; Huck, W. T. S. Rational Design of Functional and Tunable Oscillating Enzymatic Networks. *Nature Chem.* **2015**, *7* (2), 160–165. https://doi.org/10.1038/nchem.2142.

(177) Becer, C. R.; Hahn, S.; Fijten, M. W. M.; Thijs, H. M. L.; Hoogenboom, R.; Schubert, U. S. Libraries of Methacrylic Acid and Oligo(Ethylene Glycol) Methacrylate Copolymers with LCST Behavior. *Journal of Polymer Science Part A: Polymer Chemistry* **2008**, *46* (21), 7138–7147. https://doi.org/10.1002/pola.23018.

(178) Zhu, Z.; Chen, H.; Li, S.; Yang, X.; Bittner, E.; Cai, C. Tripodal Amine Ligands for Accelerating Cu-Catalyzed Azide–Alkyne Cycloaddition: Efficiency and Stability against

Oxidation and Dissociation. *Catalysis Science & Technology* **2017**, *7* (12), 2474–2485. https://doi.org/10.1039/C7CY00587C.

(179) van den Berg, C. M. G.; Kramer, J. R. Determination of Complexing Capacities of Ligands in Natural Waters and Conditional Stability Constants of the Copper Complexes by Means of Manganese Dioxide. *Analytica Chimica Acta* **1979**, *106* (1), 113–120. https://doi.org/10.1016/S0003-2670(01)83711-9.

(180) Talpur, M. M. A.; Oracz, P.; Kaim, A. Study of Methyl Methacrylate—Acrylamide Copolymerization System in Cyclohexanone in the Absence of Conventional Radical Initiator. *Polymer* **1996**, *37* (18), 4149–4154. https://doi.org/10.1016/0032-3861(96)00141-3.

(181) Wang, X.; Pu, J.; An, B.; Li, Y.; Shang, Y.; Ning, Z.; Liu, Y.; Ba, F.; Zhang, J.; Zhong, C. Programming Cells for Dynamic Assembly of Inorganic Nano-Objects with Spatiotemporal Control. *Advanced Materials* **2018**, *30* (16), 1705968. https://doi.org/10.1002/adma.201705968.

(182) Foster, J. C.; Radzinski, S. C.; Zou, X.; Finkielstein, C. V.; Matson, J. B. H2S-Releasing Polymer Micelles for Studying Selective Cell Toxicity. *Mol. Pharmaceutics* **2017**, *14* (4), 1300–1306. https://doi.org/10.1021/acs.molpharmaceut.6b01117.

(183) Tang, A.; Wang, C.; Stewart, R.; Kopeček, J. Self-Assembled Peptides Exposing Epitopes Recognizable by Human Lymphoma Cells. *Bioconjugate Chem.* **2000**, *11* (3), 363–371. https://doi.org/10.1021/bc990133d.

(184) Moitra, N.; Trens, P.; Raehm, L.; Durand, J.-O.; Cattoën, X.; Man, M. W. C. Facile Route to Functionalized Mesoporous Silica Nanoparticles by Click Chemistry. *J. Mater. Chem.* **2011**, *21* (35), 13476–13482. https://doi.org/10.1039/C1JM12066B.

(185) Gibson, M. I.; Paripovic, D.; Klok, H.-A. Size-Dependent LCST Transitions of Polymer-Coated Gold Nanoparticles: Cooperative Aggregation and Surface Assembly. *Advanced Materials* **2010**, *22* (42), 4721–4725. https://doi.org/10.1002/adma.201001382.

(186) Shan, J.; Zhao, Y.; Granqvist, N.; Tenhu, H. Thermoresponsive Properties of N-Isopropylacrylamide Oligomer Brushes Grafted to Gold Nanoparticles: Effects of Molar Mass and Gold Core Size. *Macromolecules* **2009**, *42* (7), 2696–2701. https://doi.org/10.1021/ma802482e.

(187) I. Gibson, M.; K. O'Reilly, R. To Aggregate, or Not to Aggregate? Considerations in the Design and Application of Polymeric Thermally-Responsive Nanoparticles. *Chemical Society Reviews* **2013**, *42* (17), 7204–7213. https://doi.org/10.1039/C3CS60035A.

(188) Bidirectional Nanoparticle Crossing of Oil–Water Interfaces Induced by Different Stimuli: Insight into Phase Transfer - Stocco - 2012 - Angewandte Chemie International Edition - Wiley Online Library https://onlinelibrary.wiley.com/doi/full/10.1002/anie.201203493 (accessed May 19, 2020).

(189) Chen, Z.; Ji, H.; Liu, C.; Bing, W.; Wang, Z.; Qu, X. A Multinuclear Metal Complex Based DNase-Mimetic Artificial Enzyme: Matrix Cleavage for Combating Bacterial Biofilms. *Angewandte Chemie International Edition* **2016**, *55* (36), 10732–10736. https://doi.org/10.1002/anie.201605296.

(190) Jones, C. D.; Lyon, L. A. Synthesis and Characterization of Multiresponsive Core−Shell Microgels. *Macromolecules* **2000**, *33* (22), 8301–8306. https://doi.org/10.1021/ma001398m.

(191) White, S. R.; Sottos, N. R.; Geubelle, P. H.; Moore, J. S.; Kessler, M. R.; Sriram, S. R.; Brown, E. N.; Viswanathan, S. Autonomic Healing of Polymer Composites. *Nature* **2001**, *409* (6822), 794. https://doi.org/10.1038/35057232.

(192) Keller, M. W.; White, S. R.; Sottos, N. R. A Self-Healing Poly(Dimethyl Siloxane) Elastomer. *Advanced Functional Materials* **2007**, *17* (14), 2399–2404. https://doi.org/10.1002/adfm.200700086.

(193) Blaiszik, B. J.; Kramer, S. L. B.; Olugebefola, S. C.; Moore, J. S.; Sottos, N. R.; White, S. R. Self-Healing Polymers and Composites. *Annual Review of Materials Research* **2010**, *40* (1), 179–211. https://doi.org/10.1146/annurev-matsci-070909-104532.

(194) Diesendruck, C. E.; Sottos, N. R.; Moore, J. S.; White, S. R. Biomimetic Self-Healing. *Angewandte Chemie International Edition* **2015**, *54* (36), 10428–10447. https://doi.org/10.1002/anie.201500484.

(195) Chen, X.; Dam, M. A.; Ono, K.; Mal, A.; Shen, H.; Nutt, S. R.; Sheran, K.; Wudl, F. A Thermally Re-Mendable Cross-Linked Polymeric Material. *Science* **2002**, *295* (5560), 1698–1702. https://doi.org/10.1126/science.1065879.

(196) Lu, Y.-X.; Guan, Z. Olefin Metathesis for Effective Polymer Healing via Dynamic Exchange of Strong Carbon–Carbon Double Bonds. *J. Am. Chem. Soc.* **2012**, *134* (34), 14226–14231. https://doi.org/10.1021/ja306287s.

(197) Chen, Y.; Kushner, A. M.; Williams, G. A.; Guan, Z. Multiphase Design of Autonomic Self-Healing Thermoplastic Elastomers. *Nature Chemistry* **2012**, *4* (6), 467–472. https://doi.org/10.1038/nchem.1314.

(198) Cordier, P.; Tournilhac, F.; Soulié-Ziakovic, C.; Leibler, L. Self-Healing and Thermoreversible Rubber from Supramolecular Assembly. *Nature* **2008**, *451* (7181), 977–980. https://doi.org/10.1038/nature06669.

(199) Zrínyi, M.; Szabó, D. Muscular Contraction Mimiced by Magnetic Gels. *Electro-Rheological Fluids and Magneto-Rheological Suspensions, Proceedings of the International Conference* **2000**, *15* (6), 11–17. https://doi.org/10.1142/9789812793607_0002.

(200) Fuhrer, R.; Athanassiou, E. K.; Luechinger, N. A.; Stark, W. J. Crosslinking Metal Nanoparticles into the Polymer Backbone of Hydrogels Enables Preparation of Soft, Magnetic Field-Driven Actuators with Muscle-Like Flexibility. *Small* **2009**, *5* (3), 383–388. https://doi.org/10.1002/smll.200801091.

(201) Schaefer, D. W.; Justice, R. S. How Nano Are Nanocomposites? *Macromolecules* **2007**, *40* (24), 8501–8517. https://doi.org/10.1021/ma070356w.

(202) Kumar, S. K.; Jouault, N.; Benicewicz, B.; Neely, T. Nanocomposites with Polymer Grafted Nanoparticles. *Macromolecules* **2013**, *46* (9), 3199–3214. https://doi.org/10.1021/ma4001385.

(203) Ionov, L. Polymeric Actuators. *Langmuir* **2015**, *31* (18), 5015–5024. https://doi.org/10.1021/la503407z.

(204) Huynh, T.-P.; Sonar, P.; Haick, H. Advanced Materials for Use in Soft Self-Healing Devices. *Advanced Materials* **2017**, *29* (19), 1604973. https://doi.org/10.1002/adma.201604973.

(205) Jordan, J.; Jacob, K. I.; Tannenbaum, R.; Sharaf, M. A.; Jasiuk, I. Experimental Trends in Polymer Nanocomposites—a Review. *Materials Science and Engineering: A* **2005**, *393* (1), 1–11. https://doi.org/10.1016/j.msea.2004.09.044.

(206) Ahmed, A. S.; Ramanujan, R. V. Hysteretic Buckling for Actuation of Magnet–Polymer Composites. *Macromolecular Chemistry and Physics* **2015**, *216* (15), 1594–1602. https://doi.org/10.1002/macp.201500152.

(207) Yang, Y.; W. Urban, M. Self-Healing Polymeric Materials. *Chemical Society Reviews* **2013**, *42* (17), 7446–7467. https://doi.org/10.1039/C3CS60109A.

(208) Bergman, S. D.; Wudl, F. Mendable Polymers. *J. Mater. Chem.* **2007**, *18* (1), 41–62. https://doi.org/10.1039/B713953P.

(209) Zhong, N.; Post, W. Self-Repair of Structural and Functional Composites with Intrinsically Self-Healing Polymer Matrices: A Review. *Composites Part A: Applied Science and Manufacturing* **2015**, *69*, 226–239. https://doi.org/10.1016/j.compositesa.2014.11.028.

(210) Roy, N.; Bruchmann, B.; Lehn, J.-M. DYNAMERS: Dynamic Polymers as Self-Healing Materials. *Chemical Society Reviews* **2015**, *44* (11), 3786–3807. https://doi.org/10.1039/C5CS00194C.

(211) Mozhdehi, D.; Ayala, S.; Cromwell, O. R.; Guan, Z. Self-Healing Multiphase Polymers via Dynamic Metal–Ligand Interactions. *J. Am. Chem. Soc.* **2014**, *136* (46), 16128–16131. https://doi.org/10.1021/ja5097094.

(212) Burattini, S.; M. Colquhoun, H.; D. Fox, J.; Friedmann, D.; W. Greenland, B.; F. Harris, P. J.; Hayes, W.; E. Mackay, M.; J. Rowan, S. A Self-Repairing, Supramolecular Polymer System: Healability as a Consequence of Donor–Acceptor π–π Stacking Interactions. *Chemical Communications* **2009**, *0* (44), 6717–6719. https://doi.org/10.1039/B910648K.

(213) Burnworth, M.; Tang, L.; Kumpfer, J. R.; Duncan, A. J.; Beyer, F. L.; Fiore, G. L.; Rowan, S. J.; Weder, C. Optically Healable Supramolecular Polymers. *Nature* **2011**, *472* (7343), 334–337. https://doi.org/10.1038/nature09963.

(214) Tee, B. C.-K.; Wang, C.; Allen, R.; Bao, Z. An Electrically and Mechanically Self-Healing Composite with Pressure- and Flexion-Sensitive Properties for Electronic Skin Applications. *Nature Nanotechnology* **2012**, *7* (12), 825–832. https://doi.org/10.1038/nnano.2012.192.

(215) Chung, C.-M.; Roh, Y.-S.; Cho, S.-Y.; Kim, J.-G. Crack Healing in Polymeric Materials via Photochemical [2+2] Cycloaddition. *Chem. Mater.* **2004**, *16* (21), 3982–3984. https://doi.org/10.1021/cm049394+.

(216) Capelot, M.; Montarnal, D.; Tournilhac, F.; Leibler, L. Metal-Catalyzed Transesterification for Healing and Assembling of Thermosets. *J. Am. Chem. Soc.* **2012**, *134* (18), 7664–7667. https://doi.org/10.1021/ja302894k.

(217) Amamoto, Y.; Kamada, J.; Otsuka, H.; Takahara, A.; Matyjaszewski, K. Repeatable Photoinduced Self-Healing of Covalently Cross-Linked Polymers through Reshuffling of Trithiocarbonate Units. *Angewandte Chemie International Edition* **2011**, *50* (7), 1660–1663. https://doi.org/10.1002/anie.201003888.

(218) Imato, K.; Nishihara, M.; Kanehara, T.; Amamoto, Y.; Takahara, A.; Otsuka, H. Self-Healing of Chemical Gels Cross-Linked by Diarylbibenzofuranone-Based Trigger-Free Dynamic Covalent Bonds at Room Temperature. *Angewandte Chemie International Edition* **2012**, *51* (5), 1138–1142. https://doi.org/10.1002/anie.201104069.

(219) Yang, Y.; He, J.; Li, Q.; Gao, L.; Hu, J.; Zeng, R.; Qin, J.; Wang, S. X.; Wang, Q. Self-Healing of Electrical Damage in Polymers Using Superparamagnetic Nanoparticles. *Nature Nanotechnology* **2019**, *14* (2), 151. https://doi.org/10.1038/s41565-018-0327-4.

(220) Ahmed, A. S.; Ramanujan, R. V. Magnetic Field Triggered Multicycle Damage Sensing and Self Healing. *Scientific Reports* **2015**, *5*, srep13773. https://doi.org/10.1038/srep13773.

(221) Adzima, B. J.; Kloxin, C. J.; Bowman, C. N. Externally Triggered Healing of a Thermoreversible Covalent Network via Self-Limited Hysteresis Heating. *Advanced Materials 22* (25), 2784–2787. https://doi.org/10.1002/adma.200904138.

(222) Nguyen, V. Q.; Ahmed, A. S.; Ramanujan, R. V. Morphing Soft Magnetic Composites. *Advanced Materials* **2012**, *24* (30), 4041–4054. https://doi.org/10.1002/adma.201104994.

(223) Yoonessi, M.; Lerch, B. A.; Peck, J. A.; Rogers, R. B.; Solá-Lopez, F. J.; Meador, M. A. Self-Healing of Core–Shell Magnetic Polystyrene Nanocomposites. *ACS Appl. Mater. Interfaces* **2015**, *7* (31), 16932–16937. https://doi.org/10.1021/acsami.5b04314.

(224) Ahmed, A. S.; Ramanujan, R. V. Curie Temperature Controlled Self-Healing Magnet–Polymer Composites. *Journal of Materials Research* **2015**, *30* (7), 946–958. https://doi.org/10.1557/jmr.2015.59.

(225) Post, W.; Bose, R. K.; García, S. J.; Van der Zwaag, S. Healing of Early Stage Fatigue Damage in Ionomer/Fe3O4 Nanoparticle Composites. *Polymers* **2016**, *8* (12), 436. https://doi.org/10.3390/polym8120436.

(226) Duenas, T.; Enke, A.; Chai, K.; Castellucci, M.; Sundaresan, V. B.; Wudl, F.; Murphy, E. B.; Mal, A.; Alexandar, J. R.; Corder, A.; Ooi, T. K. Smart Self-Healing Material Systems Using Inductive and Resistive Heating. In *Smart Coatings III*; ACS Symposium Series;

American Chemical Society, 2010; Vol. 1050, pp 45–60. https://doi.org/10.1021/bk-2010-1050.ch004.

(227) Corten, C. C.; Urban, M. W. Repairing Polymers Using Oscillating Magnetic Field. *Advanced Materials* **2009**, *21* (48), 5011–5015. https://doi.org/10.1002/adma.200901940.

(228) Huang, J.; Cao, L.; Yuan, D.; Chen, Y. Design of Novel Self-Healing Thermoplastic Vulcanizates Utilizing Thermal/Magnetic/Light-Triggered Shape Memory Effects. *ACS Appl. Mater. Interfaces* **2018**, *10* (48), 40996–41002. https://doi.org/10.1021/acsami.8b18212.

(229) Hohlbein, N.; Shaaban, A.; Schmidt, A. M. Remote-Controlled Activation of Self-Healing Behavior in Magneto-Responsive Ionomeric Composites. *Polymer* **2015**, *69* (Supplement C), 301–309. https://doi.org/10.1016/j.polymer.2015.04.024.

(230) Ogliani, E.; Yu, L.; Javakhishvili, I.; L. Skov, A. A Thermo-Reversible Silicone Elastomer with Remotely Controlled Self-Healing. *RSC Advances* **2018**, *8* (15), 8285–8291. https://doi.org/10.1039/C7RA13686B.

(231) Du, L.; Xu, Z.-Y.; Fan, C.-J.; Xiang, G.; Yang, K.-K.; Wang, Y.-Z. A Fascinating Metallo-Supramolecular Polymer Network with Thermal/Magnetic/Light-Responsive Shape-Memory Effects Anchored by Fe3O4 Nanoparticles. *Macromolecules* **2018**, *51* (3), 705–715. https://doi.org/10.1021/acs.macromol.7b02641.

(232) Liu, K.; Pan, X.; Chen, L.; Huang, L.; Ni, Y.; Liu, J.; Cao, S.; Wang, H. Ultrasoft Self-Healing Nanoparticle-Hydrogel Composites with Conductive and Magnetic Properties. *ACS Sustainable Chem. Eng.* **2018**, *6* (5), 6395–6403. https://doi.org/10.1021/acssuschemeng.8b00193.

(233) Feng, X. Q.; Zhang, G. Z.; Bai, Q. M.; Jiang, H. Y.; Xu, B.; Li, H. J. High Strength Self-Healing Magnetic Elastomers With Shape Memory Effect. *Macromol. Mater. Eng.* **2016**, *301* (2), 125–132. https://doi.org/10.1002/mame.201500226.

(234) Wang, Y.-M.; Pan, M.; Liang, X.-Y.; Li, B.-J.; Zhang, S. Electromagnetic Wave Absorption Coating Material with Self-Healing Properties. *Macromolecular Rapid Communications* **2017**, *38* (23), 1700447. https://doi.org/10.1002/marc.201700447.

(235) Zhang, Y.; Yang, B.; Zhang, X.; Xu, L.; Tao, L.; Li, S.; Wei, Y. A Magnetic Self-Healing Hydrogel. *Chem. Commun.* **2012**, *48* (74), 9305–9307. https://doi.org/10.1039/C2CC34745H.

(236) Yu, C.; Wang, C.-F.; Chen, S. Robust Self-Healing Host–Guest Gels from Magnetocaloric Radical Polymerization. *Advanced Functional Materials* **2014**, *24* (9), 1235–1242. https://doi.org/10.1002/adfm.201302058.

(237) Li, Q.; Barrett, D. G.; Messersmith, P. B.; Holten-Andersen, N. Controlling Hydrogel Mechanics via Bio-Inspired Polymer–Nanoparticle Bond Dynamics. *ACS Nano* **2016**, *10* (1), 1317–1324. https://doi.org/10.1021/acsnano.5b06692.

(238) Schäfer, S.; Kickelbick, G. Diels–Alder Reactions on Surface-Modified Magnetite/Maghemite Nanoparticles: Application in Self-Healing Nanocomposites. *ACS Appl. Nano Mater.* **2018**, *1* (6), 2640–2652. https://doi.org/10.1021/acsanm.8b00308.

(239) Li, W.; Wu, G.; Tan, J.; Zhu, Y.; Yu, X.; Lei, Y.; Sun, G.; You, B. Facile Fabrication of Self-Healing Superhydrophobic Nanocomposite Films Enabled by near-Infrared Light. *J Mater Sci* **2019**, *54* (10), 7702–7718. https://doi.org/10.1007/s10853-019-03426-7.

(240) Xu, S.; Zhao, B.; Adeel, M.; Mei, H.; Li, L.; Zheng, S. Shape Memory and Self-Healing Properties of Polymer-Grafted Fe3O4 Nanocomposites Implemented with Supramolecular

Quadruple Hydrogen Bonds. *Polymer* **2019**, *172*, 404–414. https://doi.org/10.1016/j.polymer.2019.04.020.

(241) Park, J.; An, K.; Hwang, Y.; Park, J.-G.; Noh, H.-J.; Kim, J.-Y.; Park, J.-H.; Hwang, N.-M.; Hyeon, T. Ultra-Large-Scale Syntheses of Monodisperse Nanocrystals. *Nat Mater* **2004**, *3* (12), 891–895. https://doi.org/10.1038/nmat1251.

(242) Bronstein, L. M.; Huang, X.; Retrum, J.; Schmucker, A.; Pink, M.; Stein, B. D.; Dragnea, B. Influence of Iron Oleate Complex Structure on Iron Oxide Nanoparticle Formation. *Chem. Mater.* **2007**, *19* (15), 3624–3632. https://doi.org/10.1021/cm062948j.

(243) Deacon, G. B.; Phillips, R. J. Relationships between the Carbon-Oxygen Stretching Frequencies of Carboxylato Complexes and the Type of Carboxylate Coordination. *Coordination Chemistry Reviews* **1980**, *33* (3), 227–250. https://doi.org/10.1016/S0010-8545(00)80455-5.

(244) Gravano, S. M.; Dumas, R.; Liu, K.; Patten, T. E. Methods for the Surface Functionalization of γ-Fe2O3 Nanoparticles with Initiators for Atom Transfer Radical Polymerization and the Formation of Core–Shell Inorganic–Polymer Structures. *Journal of Polymer Science Part A: Polymer Chemistry* **2005**, *43* (16), 3675–3688. https://doi.org/10.1002/pola.20823.

(245) Zhao, Y.; Perrier, S. Reversible Addition−Fragmentation Chain Transfer Graft Polymerization Mediated by Fumed Silica Supported Chain Transfer Agents. *Macromolecules* **2007**, *40* (25), 9116–9124. https://doi.org/10.1021/ma0716783.

(246) Marutani, E.; Yamamoto, S.; Ninjbadgar, T.; Tsujii, Y.; Fukuda, T.; Takano, M. Surface-Initiated Atom Transfer Radical Polymerization of Methyl Methacrylate on Magnetite

Nanoparticles. *Polymer* **2004**, *45* (7), 2231–2235. https://doi.org/10.1016/j.polymer.2004.02.005.

(247) Sun, Y.; Ding, X.; Zheng, Z.; Cheng, X.; Hu, X.; Peng, Y. Surface Initiated ATRP in the Synthesis of Iron Oxide/Polystyrene Core/Shell Nanoparticles. *European Polymer Journal* **2007**, *43* (3), 762–772. https://doi.org/10.1016/j.eurpolymj.2006.10.021.

(248) White, L. D.; Tripp, C. P. Reaction of (3-Aminopropyl)Dimethylethoxysilane with Amine Catalysts on Silica Surfaces. *Journal of Colloid and Interface Science* **2000**, *232* (2), 400–407. https://doi.org/10.1006/jcis.2000.7224.

(249) Skrabania, K.; Miasnikova, A.; Bivigou-Koumba, A. M.; Zehm, D.; Laschewsky, A. Examining the UV-Vis Absorption of RAFT Chain Transfer Agents and Their Use for Polymer Analysis. *Polym. Chem.* **2011**, *2* (9), 2074–2083. https://doi.org/10.1039/C1PY00173F.

(250) Chemist's Companion - A Handbook of Practical Data, Techniques, and References - Knovel https://app.knovel.com/web/toc.v/cid:kpCCAHPDT4/viewerType:toc//root_slug:viewerType%3Atoc/url_slug:root_slug%3Achemists-companion-handbook?kpromoter=federation (accessed Aug 1, 2019).

(251) Miller, J. D.; Ishida, Hatsuo. Quantitative Intermolecular Reaction of Hydrolyzed Trialkoxysilanes at Submonolayer, Monolayer, and Multilayer Surface Coverages. *Langmuir* **1986**, *2* (2), 127–131. https://doi.org/10.1021/la00068a002.

(252) Rotzoll, R.; Nguyen, D. H.; Vana, P. Trithiocarbonates Containing Trimethoxysilyl Functionalities as Mediating Agents in Reversible Addition-Fragmentation Chain Transfer

(RAFT) Polymerization of Methyl Acrylate. *Macromol. Symp.* **2009**, *275–276* (1), 1–12. https://doi.org/10.1002/masy.200950101.

(253) Bini, R. A.; Marques, R. F. C.; Santos, F. J.; Chaker, J. A.; Jafelicci, M. Synthesis and Functionalization of Magnetite Nanoparticles with Different Amino-Functional Alkoxysilanes. *Journal of Magnetism and Magnetic Materials* **2012**, *324* (4), 534–539. https://doi.org/10.1016/j.jmmm.2011.08.035.

(254) Chiefari, J.; Chong, Y. K. (Bill); Ercole, F.; Krstina, J.; Jeffery, J.; Le, T. P. T.; Mayadunne, R. T. A.; Meijs, G. F.; Moad, C. L.; Moad, G.; Rizzardo, E.; Thang, S. H. Living Free-Radical Polymerization by Reversible Addition−Fragmentation Chain Transfer: The RAFT Process. *Macromolecules* **1998**, *31* (16), 5559–5562. https://doi.org/10.1021/ma9804951.

(255) Edmondson, S.; Osborne, V. L.; Huck, W. T. S. Polymer Brushes via Surface-Initiated Polymerizations. *Chem. Soc. Rev.* **2004**, *33* (1), 14–22. https://doi.org/10.1039/B210143M.

(256) Tsujii, Y.; Ejaz, M.; Sato, K.; Goto, A.; Fukuda, T. Mechanism and Kinetics of RAFT-Mediated Graft Polymerization of Styrene on a Solid Surface. 1. Experimental Evidence of Surface Radical Migration. *Macromolecules* **2001**, *34* (26), 8872–8878. https://doi.org/10.1021/ma010733j.

(257) Moad, G.; Rizzardo, E.; Thang, S. H. Living Radical Polymerization by the RAFT Process. *Aust. J. Chem.* **2005**, *58* (6), 379–410. https://doi.org/10.1071/CH05072.

(258) Finch, C. A. Polymer Handbook: Third Edition Edited by J. Brandrup and E. H. Immergut, Wiley-Interscience, Chichester, 1989. Pp. Ix + Parts I to VIII, Price £115·00/$;175·00.

ISBN 0–471–81244–7. *British Polymer Journal* **1990**, *23* (3), 277–277. https://doi.org/10.1002/pi.4980230318.